

UNIVERSITY OF NEW SOUTH WALES

DOCTORAL THESIS

---

**Advancing Si:P donor qubits towards  
large scale quantum computing:  
Long-distance coupling**

---

*Author:*  
Stefanie TENBERG

*Supervisor:*  
Prof. Andrea MORELLO  
*Co-Supervisor:*

*A thesis submitted in fulfillment of the requirements  
for the degree of Doctor of Philosophy  
in the*

Fundamental Quantum T  
School of Electrical Engineering

September 7, 2018



## Declaration of Authorship

I, Stefanie TENBERG, declare that this thesis titled, "Advancing Si:P donor qubits towards large scale quantum computing: Long-distance coupling" and the work presented in it are my own. I confirm that:

- This work was done wholly or mainly while in candidature for a research degree at this University.
- Where any part of this thesis has previously been submitted for a degree or any other qualification at this University or any other institution, this has been clearly stated.
- Where I have consulted the published work of others, this is always clearly attributed.
- Where I have quoted from the work of others, the source is always given. With the exception of such quotations, this thesis is entirely my own work.
- I have acknowledged all main sources of help.
- Where the thesis is based on work done by myself jointly with others, I have made clear exactly what was done by others and what I have contributed myself.

Signed:

Date:



*“Nature isn’t classical, [...] , and if you want to make a simulation of nature, you’d better make it quantum mechanical, and [...] it’s a wonderful problem, because it doesn’t look so easy.”*

Richard Feynman, 1982

*“Those who dance are considered insane by those who can’t hear the music.”*

Friedrich Nietzsche



UNIVERTY OF NEW SOUTH WALES

*Abstract*

Center for Quantum Computation and Communication Technology  
School of Electrical Engineering

Doctor of Philosophy

**Advancing Si:P donor qubits towards large scale quantum computing:  
Long-distance coupling**

by Stefanie TENBERG

The Thesis Abstract is written here (and usually kept to just this page). The page is kept centered vertically so can expand into the blank space above the title too...



## *Acknowledgements*

The acknowledgments and the people to thank go here, don't forget to include your project advisor...



# Contents

<b>Declaration of Authorship</b>	<b>iii</b>
<b>Abstract</b>	<b>vii</b>
<b>Acknowledgements</b>	<b>ix</b>
<b>1 Quantum computing in silicon: A different way of computation</b>	<b>1</b>
1.1 Introduction: The quantum revolution of computation . . . . .	2
1.2 Foundation: the qubit . . . . .	2
1.2.1 An introduction to the qubit . . . . .	2
1.2.2 Phosphorus dopants in silicon . . . . .	3
1.2.3 The Phosphorus donor spin qubit . . . . .	5
1.3 Approach to large scale quantum computing . . . . .	7
1.3.1 Surface Code . . . . .	7
1.4 Circuit Quantum Electrodynamics . . . . .	7
1.5 Scope of this thesis . . . . .	7
<b>2 The flip flop qubit</b>	<b>9</b>
2.1 A new electrically accessible qubit . . . . .	10
2.1.1 Manipulating the orbital degree of freedom: the charge qubit .	10
2.1.2 Modulating the hyperfine interaction . . . . .	13
2.1.3 The flip-flop qubit . . . . .	15
2.2 Electrical noise and relaxation . . . . .	17
2.2.1 Dephasing due to electrical noise . . . . .	17
2.2.2 Relaxation . . . . .	19
2.2.3 Tunnel coupling tuning . . . . .	20
2.2.4 Adiabatic phase control . . . . .	20
2.3 Electric drive . . . . .	22
2.4 Two-qubit coupling . . . . .	28
2.5 Scaling up using circuit quantum electrodynamics . . . . .	34
<b>3 The nuclear spin qubit with an electric dipole transition</b>	<b>37</b>
3.1 Introduction . . . . .	38
3.2 Second-order Raman drive of a $^{31}\text{P}$ nuclear spin . . . . .	38
3.3 Robust electric dipole transition of a Si:P nuclear spin . . . . .	40
3.3.1 Electron, nuclear and charge hybridization . . . . .	40
3.3.2 Resilience against charge noise . . . . .	44
3.3.3 Coupling to microwave cavity photons . . . . .	45
3.3.4 Nuclear spin relaxation . . . . .	45
3.3.5 Dependence of electric dipole strength and spin relaxation rate on frequency and field detuning . . . . .	45
3.4 Long-distance coupling of nuclear spin qubits . . . . .	46
3.5 Conclusion . . . . .	48

<b>4 Building a quantum processor</b>	<b>49</b>
<b>5 Device fabrication and experimental methods</b>	<b>51</b>
5.1 Device fabrication and packaging . . . . .	52
5.2 Experimental setup . . . . .	52
<b>6 Low magnetic field effects in Si:P qubits</b>	<b>53</b>
6.1 Co-tunneling . . . . .	54
6.2 Evanescence-wave Johnson noise . . . . .	54
<b>7 Flip flop measurements</b>	<b>55</b>
<b>8 Conclusion</b>	<b>57</b>
<b>Bibliography</b>	<b>59</b>

# List of Figures

1.1	bandstructure	4
1.2	Valleys in silicon. (a) Conduction band band minima in bulk silicon, showing six ellipsoids (valleys) in the Brillouin zone. Inset : The components of the effective masses (for the valley $k_z$ ), along three directions in $k$ -space, highlighting the longitudinal ( $m_l$ ) and transverse ( $m_t$ ) masses. (b) The degeneracy of the 6 valleys broken by confinement, strain and sharp interfaces, highlighting the orbital ground states separated by valley splitting.	4
1.3	Donor confinement potential.	5
2.1	Flip-flop qubit Bloch sphere	10
2.2	Orbital and valley states	11
2.3	Charge qubit dispersion relation	12
2.4	Hyperfine interaction change with electric field	13
2.5	Flip-flop qubit dispersion relation	16
2.6	Hybridized charge-flip-flop states	17
2.7	Flip-flop dispersion for different tunnel couplings	17
2.8	Flip-flop dephasing	18
2.9	Flip-flop relaxation rate	19
2.10	Tunnel coupling tuning	20
2.11	Z-gate adiabaticity time step for each electric field $E_z$	22
2.12	High-fidelity adiabatic z-gates	23
2.13	Electric drive of the flip-flop qubit	24
2.14	Adiabatic flip-flop electric drive	24
2.15	Adiabatic gate errors	25
2.16	Electric dipole-dipole interactions between two distant flip-flop qubits	28
2.17	Screening and image charges	30
2.18	Coupling rate between 2 flip-flop qubits	32
2.19	High-fidelity adiabatic $\sqrt{iSWAP}$ gates between two distant flip-flop qubits	33
2.20	Coupling to a resonator	34
2.21	Gate performance summary	35

3.1 (a) Components of a Raman-enabled Si:P nuclear electric dipole transition. The electron spatial wavefunction (transparent gray) is shared between an interface-dot, $ i\rangle$ , and a donor-bound state, $ d\rangle$ , which are coupled by a tunnel rate $V_t$ . Metallic gates (blue) on top of $\text{SiO}_2$ dielectric (not shown) control the electron charge state via a static vertical field $E_{dc}$ , and can introduce an oscillating electric field $E_{ac}$ . In a circuit-Quantum Electrodynamics setup, the electrostatic gate can be replaced by the inner conductor of a microwave resonator, and $E_{ac}$ by the vacuum field of such resonator. A nearby broadband antenna Dehollain2013 (brown) provides the magnetic drive $B_{ac}$ . (b) Simplified energy level diagram for Raman-drive of the Si:P nuclear-spin qubit, with energy splitting $\epsilon_{ns}$ . $ \uparrow\rangle ( \downarrow\rangle)$ represents electron spin up (down), while $ \uparrow\uparrow\rangle ( \downarrow\downarrow\rangle)$ represents nuclear spin up (down). The second-order Raman drive is obtained by combining the microwave electric and magnetic drives, having frequencies $\nu_B$ and $\nu_E$ , respectively, and coupling rates $g_B$ and $g_E^{\text{ff}}$ , respectively. The drive is detuned by a frequency $\delta$ from the $ \uparrow\downarrow\rangle$ state. (c) Expanded energy diagram including the charge states $ g\rangle$ and $ e\rangle$ . . . . .	39
3.2 Nuclear spin levels in the rotating frame of the magnetic drive $B_{ac}$ at frequency $\nu_B$ . From left to right, the system eigenstates are shown while adding the electron spin state, then the charge state, then increasing the strength of the magnetic drive. See main text for a detailed description. . . . .	41
3.3 (a), Nuclear spin transition frequency $\epsilon'_{ns}$ in the rotating frame of the magnetic drive $B_{ac}$ , as a function of the static vertical electric field $E_{dc}$ across the donor-dot system, for vanishing magnetic drive ( $\epsilon'_{ns}(A) - \text{Eq. 3.13}$ , grey dashed line) and strong magnetic drive ( $\epsilon'_{ns}(A, D_{\text{drive}}) - \text{Eq. 3.18}$ , black solid line). We have assumed $B_0 = 0.2$ T, $B_{ac} = 0.6$ mT, $d = 15$ nm and $V_t \approx \epsilon_{\text{ff}}$ and $\nu_B \approx \gamma_e B_0 - A/4$ (since $\langle A \rangle = A/2$ at the ionization point). Green/yellow lines show transition frequencies calculated numerically from the Hamiltonian in Eq. 3.12. The color indicates the degree of admixture of the bare $ g\downarrow\downarrow\rangle$ state into the higher $\mathcal{H}'_{ns}$ eigenstate corresponding to each transition. The nuclear spin transition (predominantly $ g\downarrow\uparrow\rangle \leftrightarrow  g\downarrow\downarrow\rangle$ ) anticrosses a flip-flop transition (predominantly $ g\downarrow\uparrow\rangle \leftrightarrow  g\uparrow\downarrow\rangle$ ) at $E_{dc} = 350$ V/m, with a splitting $\sim 2g_B$ set by the strength of the magnetic drive. The flip-flop transition is strongly shifted by $D_{\text{so}}$ , due to its coupling to the charge qubit states around $E_{dc} = 0$ . At $E_{dc} = 250$ V/m, the nuclear-spin excited eigenstate has $\sim 75\%$ of $ g\downarrow\downarrow\rangle$ and is robust against electrical noise ( $\partial\epsilon'_{ns}/\partial E_{dc} = 0$ ). (b), Nuclear electric dipole strength $p_E^{\text{ns}} = \partial g_E^{\text{ns}}/\partial E_{ac}$ obtained from Eqs. 3.20 (theory, black line), or for numerical diagonalization of the full Hamiltonian $\mathcal{H}'$ under $E_{ac}$ drive (numerics, light blue line). For the choice of parameters used in this figure, $p_E^{\text{ns}}$ peaks where $E_{dc} = 250$ V/m. (c). Nuclear spin relaxation rate $1/T_{1,ns}$ in the presence of the magnetic drive $B_{ac}$ and the effect of coupling to phonons via charge states, Eq. 3.21. . . . .	43

- 3.4 (a) Nuclear electric dipole strength  $p_E^{\text{ns}}$  and (b) nuclear spin relaxation rate  $1/T_{1,\text{ns}}$ , as a function of the donor-dot electric field detuning,  $E_{\text{dc}}$ , and the magnetic drive frequency,  $\nu_B$ .  $E_{\text{dc}} = 0$  is the ionization point, where the electron charge is equally shared between donor and interface dot. In (a), the dashed line shows the ESR frequency  $\nu_{e,\downarrow\downarrow}$  when the nuclear spin is in the  $|\downarrow\downarrow\rangle$  state, the dot-dashed line shows the charge qubit frequency minus the nuclear spin frequency,  $\epsilon_0 - \epsilon_{\text{ns}}$ , and the dot-dot-dashed line the electron spin resonance frequency  $\nu_{e,\uparrow\uparrow}$  when the nuclear spin is in the  $|\uparrow\uparrow\rangle$  state. The charge and flip-flop states are detuned by  $\delta_{\text{so}}$ , which is close to zero at  $E_{\text{dc}} = 0$ . Charge and flip-flop states then hybridize, shifting the system eigenenergies by an AC-Stark shift  $D_{\text{so}}$ . The plots in Figs. 3.3b,c correspond to specific line cuts of the graphs shown here, for  $\nu_B = \nu_{e,\downarrow\downarrow}$  at  $E_{\text{dc}} = 0$ , *i.e.*  $\nu_B = 5.565$  GHz. . . . . 46
- 3.5 (a), Components and (b) level diagram for long-distance coupling of two  $^{31}\text{P}$  nuclear spins via electric dipole-dipole interactions. Each displaced electron produces an electric dipole field  $E_{\text{dip}}$  (shown only for one electron). The charge dipoles induced by displacing the electron wavefunction partly towards the interface dot interact with a strength  $g_{\text{dd}}$  (Eq. 2.53), and the charge qubits interact with the flip-flop states with strength  $g_{\text{so}}$  (Eq. 2.9). Adding the (global) magnetic drive of strength  $g_B$  and tuning the system to the fully-hybridized regime described in Sec. 3.3 results in a nuclear-nuclear coupling strength  $g_{2q}^{\text{ns}} \approx 0.55$  MHz at a 400 nm distance (Eq. 3.22). . . . . 47
- 4.1 **Silicon hybrid quantum processor.** **a** Schematic view of a large-scale quantum processor based upon  $^{31}\text{P}$  donors in Si, operated and coupled through the use of an induced electric dipole. Idle qubits have electrons at the interface, leaving the  $^{31}\text{P}$  nucleus in the ultra-coherent ionized state. Electrons are partially shifted towards the donor for quantum operations. The sketch shows a possible architecture where a cluster of qubits is locally coupled via the electric dipole, and a sub-group thereof is further coupled to another cluster through interaction with a shared microwave cavity (aqua). The drawing is not to scale; control lines and readout devices are not shown. . . . . 50



# List of Tables

2.1 Gate errors for different noise sources . . . . .	27
---	----



# List of Abbreviations

**LAH** List Abbreviations Here  
**WSF** What (it) Stands For



# Physical Constants

Speed of Light  $c_0 = 2.997\,924\,58 \times 10^8 \text{ m s}^{-1}$  (exact)



# List of Symbols

$a$	distance	m
$P$	power	W (J s <sup>-1</sup> )
$\omega$	angular frequency	rad



*For/Dedicated to/To my...*



## Chapter 1

# Quantum computing in silicon: A different way of computation

---

*“Second quantum revolution. The definition of insanity is doing the same thing over and over and expecting different results.”*

–Unknown

---

## 1.1 Introduction: The quantum revolution of computation

Ever since the invention of the abacus around 2700-2300BC in Babylon **abacus** computation has been a fundamental pillar of human society. Over centuries calculus and mathematics has evolved and become more and more relevant in all kinds of aspects of our lives. When in the second half of the 20th century the digital computer was invented, data processing and stored capabilities grew exponentially, following Moores Law which predicts an increase of processing power by a factor of two per year. **MooresLaw** This in turn revolutionized many aspects of modern life, like logistics, medicine, weather forecasting, banking and many more. But also is computing constantly reinventing itself, e.g. with the invention of the internet in 1990. **The conversation** <https://theconversation.com/the-history-of-computing-is-both-evolution-and-revolution-11500>

Nowadays computing is deeply embedded in every day life where humans created big data. This is fed to computers and then in turn impacts people. Thus we rely on this ever improving technology, but this is the point where we run into trouble. Not only is Moores Law is approaching a critical point after which is might break down, the quantum limit, but also are some key problems of modern society, like data-searching, simulating large chemical (or quantum) systems or predicting material properties, computationally hard - meaning that they will never be solved by a classical computer, regardless of its power. This is the frontier of complexity as John Preskill calls it. **JohnPreskillNasa** So if quantum mechanics becomes relevant for computer chips of incredibly small size and quantum systems are hard to simulate, why shouldn't we fight fire with fire and use quantum properties for computing to tackles these problems and reach the next stage of computing? Already in 1982 physicist Richard Feynman suggested this approach "Nature isn't classical, [...], and if you want to make a simulation of nature, you'd better make it quantum mechanical, and [...] it's a wonderful problem, because it doesn't look so easy." This idea has far reaching implications for the hardware necessary to realise this quantum computation - it also needs to exhibit quantum mechanical properties. Thus the classical bits are replaced by quantum bits (qubits). Unlike classical bits, qubits have two inherent quantum mechanical properties that give quantum information its power: superposition and entanglement. The former means that the qubit can be in exclusive states, like the binary 0 and 1, at the same time. The latter describes the correlation between different states - fully entangled states cannot be described independently, they are not separable. Combining this two aspects of quantum mechanics makes quantum information powerful as now highly parallel processing is possible as  $N$  qubits have  $2^N$  eigenstates which can be used simultaneously. The foundation of this is the qubit. This needs to be a well-defined two-level system, that can interact strongly with another qubit but does not interact strongly with the environment, except for measurements. This already gives us an indication that this is indeed a challenging task like Feynman already suggested, but the implications are so large that in the last decades not only researchers but also companies like IBM, Intel, Microsoft and Google have started to participate in the race for a quantum computer. Billions of dollars are invested every year for the potential to simulate quantum systems and thus develop new drugs, more efficient fertilizers and much more. Everyone wants to achieve the quantum revolution of computation and in the following chapters I will describe how this work brings us one step closer towards this aim.

## 1.2 Foundation: the qubit

### 1.2.1 An introduction to the qubit

**Smith2017** A qubit consists out of a well-defined quantum two levels system. This is defined by its Hamiltonian  $\mathcal{H}$ , an operator which corresponds to the total energy of the system. The two levels are described by the eigenstates of this system  $|0\rangle$  and  $|1\rangle$ . The qubit can then be in any superposition state  $|\psi\rangle = \alpha|0\rangle + \beta|1\rangle$  with  $\alpha \in \mathbb{C}$  and  $|\alpha|^2 + |\beta|^2 = 1$ . While this superposition state can be used during operations, it can never be observed. Whenever a quantum particle's state is measured, the part of the wave function associated with that state then collapses into a single eigenstate with a single eigenvalue, in this case either  $|0\rangle$  or  $|1\rangle$ . The probability to collapse into this states is respectively  $|\alpha|^2$  and  $|\beta|^2$ . Thus, to readout

a quantum state, a temporal ensemble measurement is performed by repeating the whole process many times.<sup>1</sup>

A qubit can be represented geometrically as a vector in three-dimensional space, where the mutually orthogonal eigenstates  $|0\rangle, |1\rangle$  are typically positioned on the north and south pole respectively. All points on the surface of the sphere symbolize pure superpositions of the eigenstates while interior points signify mixed states. This construct is called Bloch sphere and shown in figure ??.

There exist plenty two-level system in different physical systems. However, to viably implement a qubit a number of criteria need to be fulfilled at a minimum. DiVincenzo first devised these guidelines. **DiVincenzocriteria** The qubit itself must be well-defined, aka describable by an Hamiltonian, as well as have a well-defined known initial state in which it can be prepared with high precision before starting an operation. Furthermore, one needs to be able to measure the qubit, thus being able to read-out the value of the qubit precisely at any time. Moreover, a universal set of quantum gates has to exist for one and two qubits to execute quantum algorithms. On contrast the qubit needs to be isolated from its environment to prevent fluctuations on the outside to change the quantum state, leading to a loss of state coherence. This coherence needs to be much smaller than the gate operation time. Lastly the qubits have to form a scalable architecture where many qubits can interact with each other, long distance transport of qubit states is possible and errors can be corrected. Notice that while qubits are the most common way to attempt building a quantum computer, quantum d-state systems or continuous quantum variables also seem to be a viable option **Ladd2010**.

There exist a myriad of physical systems that promise to fulfil these criteria reaching from microscopic systems such as trapped atoms, photons and spins in semiconductors to macroscopic systems such as superconducting qubits. **Ladd2010** As it stands, trapped ions and superconducting qubits are leading the race in form of number of connected qubits, reaching 50 and 49 respectively **50qubits, 49qubits**. However, if these platforms will establish themselves in the long run is still in question as trapped ions are challenging to scale up to large qubit networks and superconducting qubits struggle with ???**idk**. One very promising and growing sector are semiconductor spin qubits, specifically silicon based ones. Due to the facts, that firstly, they are compatible with the current billion dollar semiconductor industry and secondly, they have potential for large scale quantum computing as they are small but still flexible. DiVincenzo and Daniel Loss first proposed a single spin qubit in 1999 **Loss1998**. Shortly after, the first GaAs spin qubit was build in 2004 **Elzerman2004** and has seen huge development since **Koppens2006, Petta2005, ...**. However, silicon has always been the dream qubit material as its industry nano-processing capacities are far superior and it lacks the intrinsic nuclear magnetic field which makes GaAs difficult to work with. In 1998 Kane already proposed a silicon based quantum computer [1], but it took until 2007 for the first single electron occupation quantum dot **Simmons2007** to be realised. Since then phosphorus donor based qubits [2], CMOS qubits **Feldhorst** and SiGe qubits **Tarucha** have been devised reaching high levels of accuracy and control ???. The focus of this thesis is the single spin donor based qubit in silicon.

### 1.2.2 Phosphorus dopants in silicon

Crystalline silicon is bonded covalently with a diamond structure. Its band structure is drawn in figure 1.1 and shows that the conduction band minimum is at a momentum of  $k_0 = 0.85k_0$  with  $k_0 = 1/a_0$  as the Brillouin zone boundary and such has an indirect band gap. This minimum has a six-fold degeneracy due to the cubic symmetry of bulk silicon. We call this 6 conduction band minima valleys. In nanodevices the degeneracy can be lifted due to breaking of symmetry. Specifically, for an electron bound to a donor positioned in the silicon lattice, the strong confinement potential created by the dopant atom, lifts breaks the cubic symmetry and lifts the degeneracy so that the six levels split into a singlet ground state A1 and a triply (T2)- and doubly-degenerate (E) set of excited states as portrayed in figure 1.2 (b).

---

<sup>1</sup>For completeness, a spatial ensemble measurement is also possible.

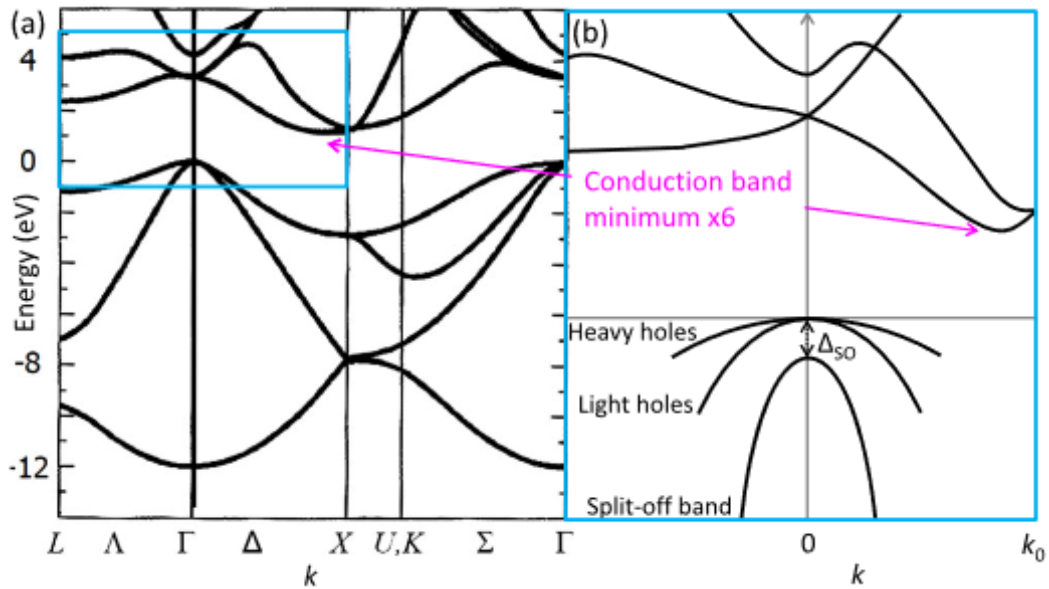


FIGURE 1.1: bandstructure

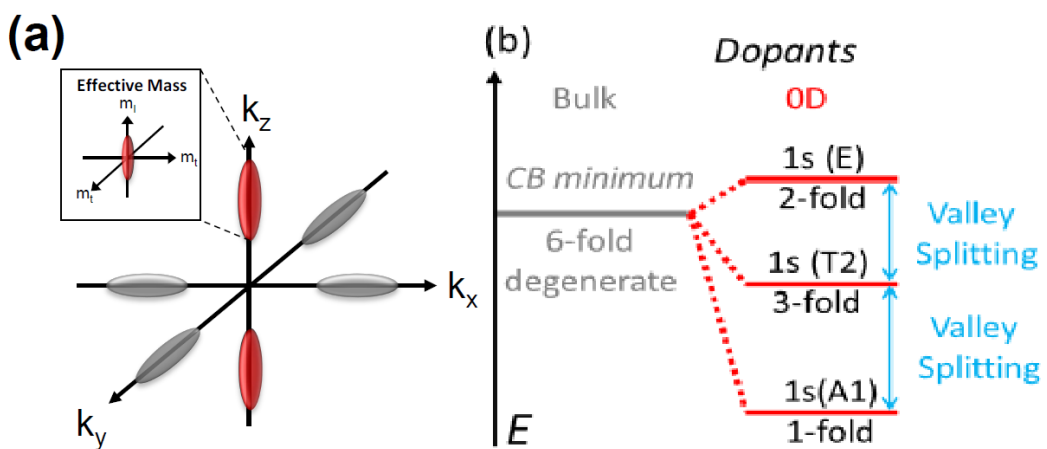


FIGURE 1.2: Valleys in silicon. (a) Conduction band band minima in bulk silicon, showing six ellipsoids (valleys) in the Brillouin zone. Inset : The components of the effective masses (for the valley  $k_z$ ), along three directions in  $k$ -space, highlighting the longitudinal ( $m_l$ ) and transverse ( $m_t$ ) masses. (b) The degeneracy of the 6 valleys broken by confinement, strain and sharp interfaces, highlighting the orbital ground states separated by valley splitting.

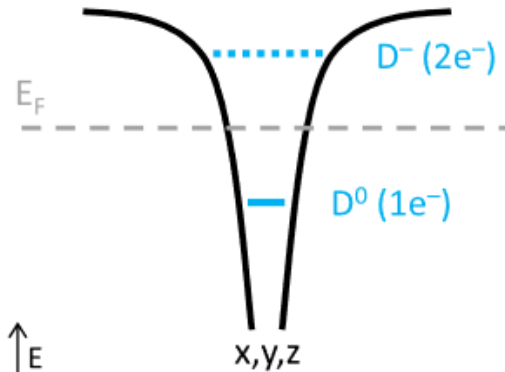


FIGURE 1.3: Donor confinement potential.

d

### 1.2.3 The Phosphorus donor spin qubit

Spin is an intrinsic quantum mechanical property of elementary particles and atomic nuclei that describes how the particle is deflected when moving in magnetic fields. It gives the particle angular momentum and a small magnetic moment. Spin is quantized, thus can only take discrete values  $-s, -s+1, \dots, s-1, s$  where  $s = \frac{n}{2}$  is the spin quantum number with  $n \in \mathbb{N}_0$ . This makes spin  $s = 1/2$  ideal for quantum computation, being a natural two level system. A particle with spin  $1/2$  is the electron. The excess electron of a donor in silicon can be used for this purpose. In this environment the donor atom in the semiconductor can be treated analogous to a hydrogen atom in vacuum with a few modifications **Zwanenburg**. E.g. due to the broken symmetry the dispersion relation for electrons near the bottom of each valley is anisotropic and is described by two light transverse effective masses ( $m_t = 0.19m_0$ ) and a heavy longitudinal effective mass ( $m_l = 0.98m_0$ ), where  $m_0$  is the mass of the free electron **d**. This is illustrated in figure 1.2 (a).

Phosphorus is a convenient donor for silicon as its nucleus also carries spin  $1/2$  which gives us a second qubit "for free". The spin states  $\pm \frac{1}{2}$  of the electron and the nucleus will be called  $\{|\uparrow\rangle, |\downarrow\rangle\}$  and  $\{|\uparrow\uparrow\rangle, |\downarrow\downarrow\rangle\}$  respectively. Unperturbed these spin states have the same energy - they are degenerate. However, if an external magnetic field  $B_0$  is applied they split by the Zeeman energy  $E_z = \gamma B_0$ , with  $\gamma$  being the corresponding gyromagnetic ratio, making them accessible as qubits. The Hamiltonian describing this system is

$$H_Z = \gamma_e B_0^z S_z - \gamma_N B_0^z I_z \quad (1.1)$$

with  $B_0^z$  as the component of the magnetic field along the z-axis,  $\{S_z, I_z\}$  the spin operator in z direction of the electron and nucleus respectively and  $\gamma_e = 28 \text{ GHz/T}$ ,  $\gamma_N = 17 \text{ MHz/T}$  as the respective gyromagnetic ratios.

However, the electron and the nucleus are not separated from each other but interact intrinsic due to the hyperfine interaction  $A$ . This interaction arises from the wave function overlap of the singlet electron ground state A1 and the nucleus and adds an interaction term  $AS \cdot I$  to the Hamiltonian

$$H = H_z + H_A = \gamma_e B_0^z S_z - \gamma_N B_0^z I_z + AS \cdot I \quad (1.2)$$

The excited electron valley states have zero probability at the nucleus and thus do not exhibit hyperfine interaction. For the conditions  $\gamma_e B_0^z \ll A > \gamma_N B_0^z$  which imply that the detuning between the coupled states  $|\uparrow\downarrow\rangle, |\downarrow\uparrow\rangle$  is much larger than the hyperfine coupling, the electron and nuclear states can be separated and the eigenstates of the Hamiltonian  $|\uparrow\uparrow\rangle, |\uparrow\downarrow\rangle, |\downarrow\uparrow\rangle, |\downarrow\downarrow\rangle$  are the tensor products of the individual spin states  $|\uparrow\uparrow\rangle = |\uparrow\rangle \otimes |\uparrow\rangle$  etc. In figure ?? the energy levels of the eigenstates are displayed.

**Electron qubit initialization and measurement** <sup>2</sup> To successfully operate the spin system as qubits, one needs to be able to determine in which spin state it is at any given time. To achieve this, we convert the electron spin signal into a charge signal, known as spin to charge conversion and then electrically read out the charge signal with off the shelf electronics.

To convert from spin to charge the spin states of the electron are tuned with bias voltages such that the Fermi level of a neighbouring reservoir lies in between both states like shown in figure ?? . In this case  $|\uparrow\rangle$  will tunnel into the reservoir and be replenished by  $|\downarrow\rangle$  while  $|\downarrow\rangle$  will stay at the donor. As this tunnel process is a moving charge, we have now converted the spin signal into a charge signal.

The key feature to now readout this charge signal is the single electron transistor (SET). This is a nanometric structure which can form an island of hundreds of electrons. The island is capacitively coupled to a top gate and tunnel coupled to source and drain reservoirs as shown in figure ?? . The energy of this island is

$$\begin{aligned} E &= \frac{Q^2}{2C} \\ &= \frac{e^2 N^2}{2C} \\ &= E_C N^2 \end{aligned}$$

where  $Q$  is the charge of island which consists out of  $N$  electrons,  $C$  is the total capacitance of the dot and  $E_C$  the charging energy. To add one electron one needs the energy

$$\begin{aligned} \Delta E(N) &= E(N+1) - E(N) \\ &= E_C \left( N + \frac{1}{2} \right) \end{aligned}$$

also called the electrochemical potential  $\mu(N)$ . Transport, thus current flow, occurs when the electrochemical potential to add the  $N$ th electron lies between the Fermi levels of the source and drain reservoirs as shown in figure ?? . If transport is blocked, the SET is in Coulomb blockade. By varying the top gate voltage oscillations between high and low current occurs when single electrons tunnel, which are called Coulomb oscillations and are shown in figure ?? . Due to the sharp slope of these curves, the sensitivity of the SET current to changes in the electrostatic environment is very high. Thus a change in charge on the donor due to a spin tunnelling event will result in a change in current on the SET. Consequently we can readout the electron qubits spin state. This is shown in figure ?? .

This measurement process can also be used to initialize the qubit into a well known state, a vital feature for qubit operation, as at the end of the process always  $|\downarrow\rangle$  is occupying the donor.

This has been first demonstrated on a single electron spin on a phosphorus donor in 2010 by A. Morello who showed single shot readout.[2]

**Qubit control** To control the qubits we use magnetic resonance. As mentioned above, spins have a magnetic momentum and react to external magnetic fields. More precisely they precess around the axis of magnetization with a frequency  $f_L$ , the so called Larmor frequency. Now we apply a magnetic pulse oscillating with a frequency  $f_{ac}$ . In the reference frame of this oscillating field, also known as the rotating frame, the spin appears to precess at a frequency  $\Delta f = f_L - f_{ac}$ . If a magnetic drive with the same frequency as the Larmor frequency is applied perpendicular to  $B_0^z$ , it appears in the rotating frame as a static field of amplitude  $B_1$  in the x-y plane. If the spin has been prepared in either  $|\uparrow\rangle$  or  $|\downarrow\rangle$ , the spin will rotate around the axis of  $B_1$  with frequency  $f_{Rabi} = \gamma B_1$ , the Rabi frequency, as these rotations are called Rabi oscillations. This is shown in figure ?? . When this magnetic resonance technique is applied to the electron, we speak of electron spin resonance (ESR) and when

<sup>2</sup>The nuclear qubit can be mapped onto the electron with pulses discussed in the paragraph "Qubit control" and thus relies on the same principles.

it is applied to the nucleus of nuclear magnetic resonance (NMR). In figure ?? these magnetic transitions and their resonance frequencies are illustrated. For the phosphorus donor electron qubit this was first demonstrated in 2012[3] and for the nuclear qubit in 2013.??

**Qubit decoherence** Quantum decoherence is the loss of quantum information from a system, in our case the qubit, to the environment. This happens as the qubit is never fully isolated from its environment and interactions lead to the transfer of information from the qubit to the outside.

There are two main parameters which describe the lifetime of the qubits quantum information.

Firstly, there is the relaxation time  $T_1$  which is the time scale on which the qubit decays from its excited state  $|\uparrow\rangle$  to its ground state  $|\downarrow\rangle$  due a perturbation orthogonal to the quantization axis, in the case of the donor qubit this means a perturbation of type  $\sigma_{x,y}$ . This perturbations can e.g. arise due to charge fluctuations and tunnelling effects. More about the specific effect of this process on our qubit, its origins and how to mitigate it will be discussed in chapter ??.

Secondly, there is the randomization of the phase of a quantum superposition on the time scale  $T_2$ , which is called dephasing. Slow perturbations along the quantization axis  $\sigma_z$  cause the Larmor frequency to fluctuate and the state starts precessing in the rotation frame such that we loose track of the phase of the state. In ensemble measurements a third time scale is relevant, the dephasing time  $T_2^*$ , where different parts of the ensemble have different Larmor frequencies due to slow fluctuations. As we are working with single spins, we only encounter time ensemble measurements. In these cases the Larmor frequency varies between each measurement due to slow changes in the environment in between. This dephasing can be suppressed by clever pulsing methods like hahn echo and CPMG **CPMG**.

Both the electron and the nuclear spin have exceptionally long coherence times when placed in an environment with few surrounding spins, as was first measured by J. Muhonen in 2014 [4]. In combination with the high fidelity control, this makes for an excellent qubit.

## 1.3 Approach to large scale quantum computing

### 1.3.1 Surface Code

## 1.4 Circuit Quantum Electrodynamics

## 1.5 Scope of this thesis



## Chapter 2

# The flip flop qubit

---

*"Scalability is the future"*

-?

---

 As discussed in chapter 1.3, new ideas for long range, scalable coupling are necessary to advance silicon quantum computing. This chapter presents a new type of qubit that relies on electric dipole interactions and aims to answer this demand.



## 2.1 A new electrically accessible qubit

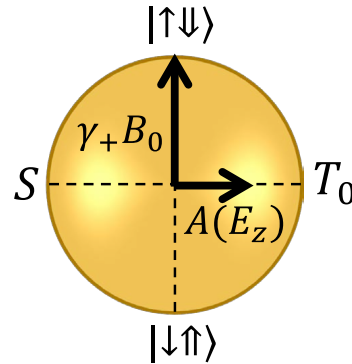


FIGURE 2.1: **Flip-flop qubit Bloch sphere.** Bloch sphere of a flip-flop spin qubit in an external magnetic field  $B_0$  coupled to a vertical electric field  $E_z$  via the hyperfine interaction  $A$ . Electron-nuclear singlet and triplet states are denoted by  $S = (|↓↑⟩ - |↑↓⟩) / \sqrt{2}$  and  $T_0 = (|↓↑⟩ + |↑↓⟩) / \sqrt{2}$ .

The new qubit is based on the phosphorus donor qubit as described in section 1.2.3. However, instead of encoding the quantum information in just the electron or the nuclear spin, we define a new qubit with the anti-aligned spin states  $|↓↑⟩, |↑↓⟩$  as the basis. We call this the flip-flop qubit. This transition is not magnetically accessible as the total z-angular momentum is constant. However, the hyperfine interaction  $H = AS \cdot I$  is a transverse term for this states with its eigenstates  $S = (|↓↑⟩ - |↑↓⟩) / \sqrt{2}$  and  $T = (|↓↑⟩ + |↑↓⟩) / \sqrt{2}$  (see figure 2.1) and thus can be used to drive the transition. The flip-flop qubit energy splitting is

$$\epsilon_{\text{ff}}(A) = \sqrt{(\gamma_+ B_0)^2 + A^2}, \quad (2.1)$$

where  $\gamma_+ = \gamma_e + \gamma_n$ . If  $A$  is now modulated at frequency  $\epsilon_{\text{ff}}$ , we are driving the flip-flop transition with electric dipole spin resonance (EDSR).

The hyperfine interaction strength between the electron and the nucleus depends on the overlap of the electron wave function with the nucleus position  $A \sim |\psi(0, 0, z_d)|^2$ . Hence, by reducing said overlap, the interaction can be decreased. This can be achieved by applying an electric field on top of donor that pulls the electron from the donor to the SiO<sub>2</sub> interface, where it behaves like a quantum dot after ionization. The electron charge position is described by the orbital degree of freedom.

### 2.1.1 Manipulating the orbital degree of freedom: the charge qubit

When the electron is at the donor, the ground orbital wavefunction  $|d\rangle$  is a symmetric combination of the 6 valleys  $k_{\pm x}, k_{\pm y}, k_{\pm z}$  (see chapter 1.2.2). The next valley-orbit states are 11.7 meV higher in energy and thus can be neglected. When the electron is confined at the interface, in a quantum dot like state, in-plane strain splits off the in-plane  $k_{\pm x}, k_{\pm y}$  valleys so that the wave function lives in the z valleys  $k_{\pm z}$  where the remaining twofold degeneracy is lifted by the electronic z confinement into a lower valley  $|i\rangle$  and a higher valley  $|v\rangle$ . The remainder of the excited donor and dot states are well above the ground states by several meV [5], [6]. Thus, close to the ionization point  $E_z^0$ , the lowest-energy states of the system are  $|d\rangle, |i\rangle, |v\rangle$  as shown in figure 2.2 inset. These levels can be computed with atomistic tight



binding calculations using the package NEMO-3D [7], [8] which donor depth  $z_d = 15.2$  nm below the Si/SiO<sub>2</sub> interface and the donor biased close to ionization. Figure 2.2 shows the dependence of the energy levels on the electric field  $E_z$  with the dots indicating the tight binding simulations.

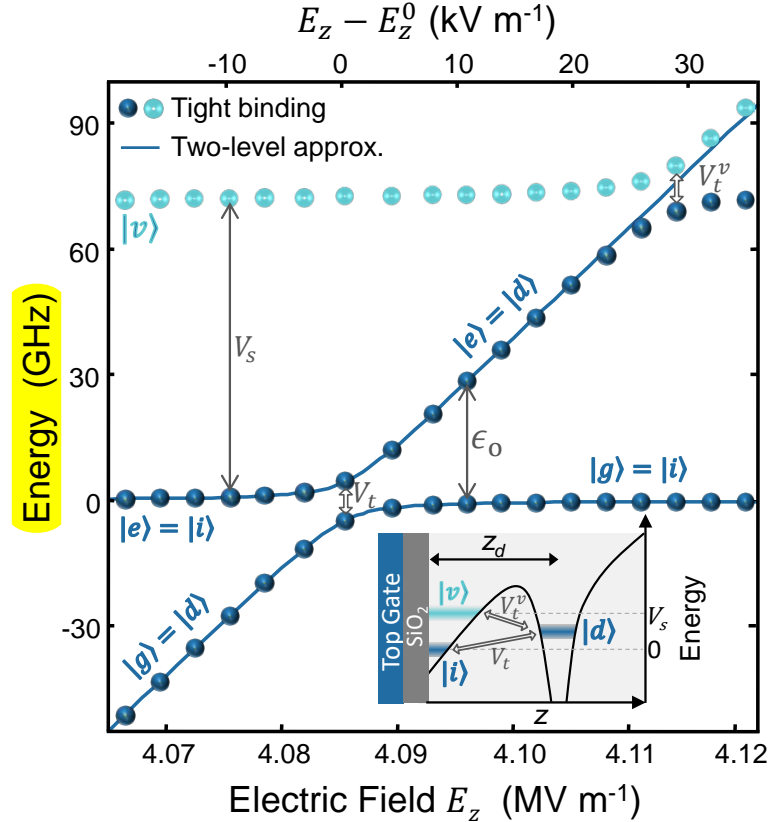


FIGURE 2.2: **Orbital and valley states.** The lowest orbital energy levels of the donor-interface system, with respect to the lower valley interface state  $|i\rangle$  (set as the zero-energy reference). The donor is assumed 15.2 nm below a Si/SiO<sub>2</sub> interface. The dots correspond to the energy levels obtained from a full-scale tight-binding calculation with NEMO-3D. Solid lines represent the energy levels obtained from the two level approximation described by Eq. 2.3. Inset: Potential profile as a function of depth, illustrating the donor  $|d\rangle$ , lower  $|i\rangle$  and upper  $|v\rangle$  valley interface states. The donor ground state is tunnel-coupled to the lower and upper valley interface states by  $V_t$  and  $V_t^v$  respectively.

We find that the electron orbital charge qubit degree of freedom can be approximated by a two-level system with ground state  $|g\rangle$  and excited state  $|e\rangle$  for  $E_z < E_z^0 \sim 4.11$  MV/m when the third valley state  $|v\rangle$  becomes relevant.

When  $E_z \ll E_z^0$ , the charge qubit ground state  $|g\rangle$  consists of the electron being localized at the donor,  $|d\rangle$ , whereas the first excited state  $|e\rangle$  corresponds to the lower valley interface state  $|i\rangle$ . With increasing  $E_z$ , the two states approach, and anticross at the ionization point  $E_z = E_z^0$ . For  $E_z \gg E_z^0$   $|d\rangle$  is the excited state, until it eventually anticrosses with the upper valley interface state  $|v\rangle$  at  $E_z^v$ .

We can describe this charge qubit with the Pauli matrices

$$\sigma_x = \begin{pmatrix} 0 & 1 \\ 1 & 0 \end{pmatrix}, \sigma_y = \begin{pmatrix} 0 & -i \\ i & 0 \end{pmatrix}, \sigma_z = \begin{pmatrix} 1 & 0 \\ 0 & -1 \end{pmatrix}. \quad (2.2)$$

Choosing  $|d\rangle = \begin{pmatrix} 0 \\ 1 \end{pmatrix}$ ,  $|i\rangle = \begin{pmatrix} 1 \\ 0 \end{pmatrix}$  as the basis states the corresponding Hamiltonian is

$$\mathcal{H}_{\text{orb}} = \frac{V_t \sigma_x - [e(E_z - E_z^0)d/h] \sigma_z}{2}, \quad (2.3)$$

 id lines in figure 2.2) with an energy separation between the two levels of

$$\epsilon_0 = \sqrt{(V_t)^2 + [e(E_z - E_z^0)d/h]^2}. \quad (2.4)$$

 wells (at  $z_d = 15.2$  nm),  $E_z^0$  is the vertical electric field at the ionization point and  $h$  is the Planck constant. The charge qubit transition energy is plotted in figure 2.3. We find that  $d = 11$  nm, which represents the separation between the center-of-mass positions of the donor  $|d\rangle$  and interface  $|i\rangle$  orbitals, and is expectedly lower than the donor depth  $z_d$ .

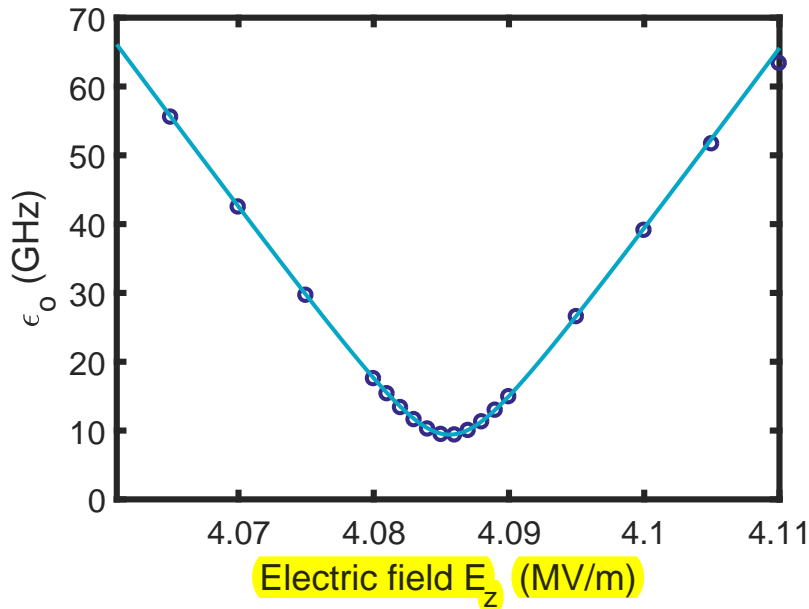


FIGURE 2.3: **Charge qubit dispersion relation.** Charge qubit dispersion relation  $\epsilon_0$  as a function of vertical electric field  $E_z$ , for  $V_t = 9.3$  GHz,  $d = 11$  nm and  $E_z^0 = 0$  V. The dots are obtained by NEMO-3D full-scale tight binding simulation while the line corresponds to the two-level approximation, giving eq. (2.4).

At the ionization point  $E_z^0$  the basis states of the charge qubit are  $|g\rangle = \frac{|i\rangle - |d\rangle}{\sqrt{2}} = \frac{1}{\sqrt{2}} \begin{pmatrix} -1 \\ 1 \end{pmatrix}$  and  $|e\rangle = \frac{|i\rangle + |d\rangle}{\sqrt{2}} = \frac{1}{\sqrt{2}} \begin{pmatrix} 1 \\ 1 \end{pmatrix}$  and  $\epsilon_0 = V_t$ . If we were to express the charge qubit in this basis, we transform  $\sigma_z \leftrightarrow -\sigma_x$  in  $H_{\text{orb}}$ .

More generalized we can express the charge qubit eigenstates as

$$|e\rangle = \alpha_1 |i\rangle + \beta_1 |d\rangle = \begin{pmatrix} \alpha_1 \\ \beta_1 \end{pmatrix} \quad (2.5)$$

$$|g\rangle = \alpha_2 |i\rangle + \beta_2 |d\rangle = \begin{pmatrix} \alpha_2 \\ \beta_2 \end{pmatrix} \quad (2.6)$$

with  $\alpha_{1,2}, \beta_{1,2}$  depending on  $V_t$  and  $E_z$ .

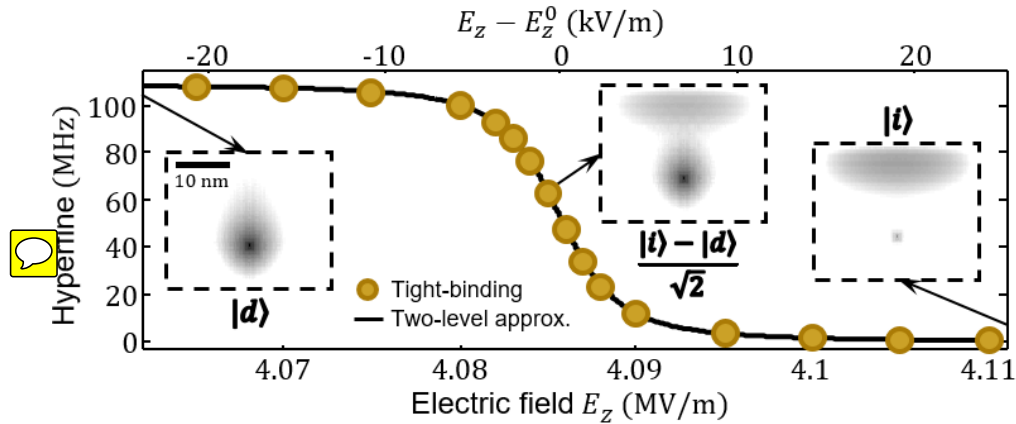


FIGURE 2.4: **Hyperfine interaction change with electric field** Atomistic tight-binding simulations [7], [8] (dots) of the electron-nucleus hyperfine interaction, for a  $z_d = 15.2$  nm deep donor, as a function of vertical electric field. The solid line is a fit using the simplified two-level Hamiltonian  $\mathcal{H}_{\text{orb}} + \mathcal{H}_A^{\text{orb}}$ , which yields  $V_t = 9.3$  GHz (see 2.2). The insets show the electron ground-state wavefunction  $|g\rangle$  for three different vertical electric fields.

### 2.1.2 Modulating the hyperfine interaction

As the hyperfine coupling the electron and nucleus experience depends on the wave function overlap between electron and nucleus, it depends on the state of the charge qubit. Is the charge qubit in the donor state  $|d\rangle$ , the hyperfine interaction is full strength  $A$  while it is 0 if the charge qubit is in the interface state  $|i\rangle$ . Thus we can describe the orbital dependent hyperfine Hamiltonian as

$$\mathcal{H}_A^{\text{orb}} = A \left( \frac{1 - \sigma_z}{2} \right) \mathbf{S} \cdot \mathbf{I} \quad (2.7)$$

Figure 2.4 shows the hyperfine strength with applied electric field. The dots present the tight-binding simulations with NEMO-3D[7], [8]. The line is derived from the Hamiltonian by calculating the ground state eigenvector  $|g\rangle$  and measuring its expectation value

$$A(E_{dc}) = \langle g | A \left( \frac{1 - \sigma_z}{2} \right) | g \rangle = A |\beta_2|^2. \quad (2.8)$$

We find that both methods agree well which confirms our two-level approximation. The insets show the wavefunction at different electric fields.

To determine the coupling between the charge qubit and the spin states  $|\downarrow\uparrow\rangle, |\uparrow\downarrow\rangle$  we calculate the matrix transition element

$$g_{so} = \langle g \uparrow\downarrow | H_A^{\text{orb}} | e \downarrow\uparrow \rangle = \frac{A}{4} \langle g | \sigma_z | e \rangle = \frac{A}{2} (\alpha_1 \alpha_2^\dagger - \beta_1 \beta_2^\dagger) \quad (2.9)$$

At the ionization point  $\langle g | \sigma_z | e \rangle = 1$  and the coupling is the strongest, allowing for fast driving. To calculate  $\langle g | \sigma_z | e \rangle$  outside the ionization point we need to determine  $\alpha, \beta$  from equations (2.5), (2.6) by calculating the eigenvectors  $|g\rangle, |e\rangle$ .

We generalize the problem to

$$H = \begin{pmatrix} -A & B \\ B & A \end{pmatrix} \quad (2.10)$$

where  $A = e^{\frac{(E_z - E_z^0)d}{2h_i}}$  and  $B = \frac{V_t}{2}$ .

The eigenvectors are calculated by

$$\begin{pmatrix} -A - \lambda_{1,2} & B \\ B & A - \lambda_{1,2} \end{pmatrix} \cdot \begin{pmatrix} \alpha_{1,2} \\ \beta_{1,2} \end{pmatrix} = \begin{pmatrix} 0 \\ 0 \end{pmatrix} \quad (2.11)$$

which gives the equations

$$(-A - \lambda_{1,2}) \alpha_{1,2} + B \beta_{1,2} = 0 \quad (2.12)$$

$$\alpha_{1,2} A + (A - \lambda_{1,2}) \beta_{1,2} = 0. \quad (2.13)$$

Furthermore, we have the normalization condition

$$\beta_{1,2} = \sqrt{1 - \alpha_{1,2}^2}. \quad (2.14)$$

We insert equation (2.14) into (2.12), (2.13) and get

$$\alpha_{1,2} = \frac{1}{\sqrt{1 + \frac{(A + \lambda_{1,2})^2}{B^2}}} \quad (2.15)$$

$$\beta_{1,2} = \sqrt{1 - \frac{1}{1 + \frac{(A + \lambda_{1,2})^2}{B^2}}}. \quad (2.16)$$

With

$$\lambda_{1,2} = \pm \sqrt{A^2 + B^2} \quad (2.17)$$

follows

$$\begin{aligned} \alpha_1 &= \frac{1}{\sqrt{\Phi^2 + 1}} = \beta_2 \equiv \beta \\ \beta_1 &= \frac{\Phi}{\sqrt{1 + \Phi^2}} \equiv \alpha \\ \alpha_2 &= \frac{1}{\sqrt{1 + \Theta^2}} = -\beta_1 = -\alpha \\ \beta_2 &= \frac{\Theta}{\sqrt{1 + \Theta^2}} = \beta \end{aligned} \quad (2.18)$$

where

$$\begin{aligned} \Phi &= \frac{A + \sqrt{A^2 + B^2}}{B} \\ \Theta &= \frac{A - \sqrt{A^2 + B^2}}{B}. \end{aligned} \quad (2.19)$$

This gives us the hybridized states

$$\begin{aligned} |e\rangle &= \beta|i\rangle + \alpha|d\rangle \\ |g\rangle &= -\alpha|i\rangle + \beta|d\rangle. \end{aligned} \quad (2.20)$$

Now we can calculate  $A(E_{dc})$  with equation (2.8) to

$$A(E_{dc}) = A \left( \frac{\Theta}{\sqrt{1 + \Theta^2}} \right)^2 = \frac{A}{2} \left( 1 - \frac{e(E_z - E_z^0) d / h}{\epsilon_0} \right). \quad (2.21)$$

and the coupling rate (2.9) to

$$g_{so} = \frac{A}{4} \frac{V_t}{\epsilon_0}. \quad (2.22)$$

Here we have assumed that the hyperfine coupling between electron spin and  $^{31}\text{P}$  nucleus is purely isotropic [9], i.e. dominated by the Fermi contact hyperfine term. This assumption may no longer exactly hold when the donor electron wave function is distorted from its spherical symmetry in the presence of the strong vertical electric field, whereby a small dipolar component can be created (a related case, where the electron is shared between two proximal P donors, has been recently studied [10]). However, it is known that the Fermi

contact component of the hyperfine coupling for donors in silicon is always the dominant term, even for  $^{29}\text{Si}$  nuclei which are placed off-center with respect to the symmetry point of the wavefunction [11]. Therefore, we expect the isotropic approximation to capture the main physics of the problem.

### 2.1.3 The flip-flop qubit

As we apply an external magnetic field  $B_0$  to our system, we need to account for the Zeeman energy of both the electron and the nuclear spin. This energy depends on the gyromagnetic ratio. However, the electron gyromagnetic ratio  $\gamma_e$  changes when the electron is confined at the Si/SiO<sub>2</sub> interface, up to 0.7% from the donor-bound electron [5]. We include this in the Zeeman Hamiltonian

$$\mathcal{H}_{B_0}^{\text{orb}} = \gamma_e B_0 \left[ 1 + \left( \frac{1 + \sigma_z}{2} \right) \Delta \gamma \right] S_z - \gamma_n B_0 I_z. \quad (2.23)$$

Thus to describe the full physics of the flip-flop qubit we get

$$\mathcal{H}_{\text{ff}} = \mathcal{H}_{B_0}^{\text{orb}} + \mathcal{H}_A^{\text{orb}} + \mathcal{H}_{\text{orb}}. \quad (2.24)$$

This system is composed of the three degrees of freedom, orbital, electron spin and nuclear spin which gives us a eight-dimensional Hamiltonian of

$$\mathcal{H}_{\text{ff}} = \mathcal{H}_{\text{orb}} \otimes \mathcal{H}_e \otimes \mathcal{H}_n \quad (2.25)$$

with the unperturbed energy eigenstates  $\{|g\rangle, |e\rangle\} \otimes \{| \uparrow\rangle, | \downarrow\rangle\} \otimes \{| \uparrow\rangle, | \downarrow\rangle\}$  with the spin states pointing along the external magnetic field. As long as the Zeeman energy exceeds the hyperfine modulation characterized by  $A/4$ , the latter is a perturbation only and the energy eigenstates of  $\mathcal{H}_{\text{ff}}$  remain the approximate products of the eigenstates.

To calculate the flip-flop qubit transition energy we numerically determine the eigenvectors of  $\mathcal{H}_{\text{ff}}$  and find the ones with the largest overlap to the flip-flop states  $|g \downarrow\uparrow\rangle, |g \uparrow\downarrow\rangle$  with the orbital state remaining unexcited. We then compute the flip-flop qubit transition energy by calculating the difference of the corresponding eigenvalues. Thus we arrive at the curve plotted in yellow in figure 2.5.

When we compare these results to the bare flip-flop energy  $\epsilon_{\text{ff}}(A, \gamma_e)$  (2.1) (plotted in dotted grey in figure 2.5) we find a large deviation around the ionization point.  $\epsilon_{\text{ff}}(A, \gamma_e)$  shows a steep slope, mostly caused by the  $E_z$ -dependence of  $\gamma_e$  as  $\gamma_e B_0 \gg A$  while  $\mathcal{H}_{\text{ff}}$  sees a dip. This dip is a result of the transverse coupling between the charge and spin states created by the hyperfine coupling in  $H_{\text{orb}}^A$ .

The insert in figure 2.5 shows the energy levels for our qubit system. On the one hand, we have the charge qubit states  $|g\rangle$  and  $|e\rangle$  and on the other the spin flip-flop states  $| \downarrow\uparrow\rangle$  and  $| \uparrow\downarrow\rangle$  which are separated by  $\epsilon_0$  and  $\epsilon_{\text{ff}}$  respectively. Thus the charge and flip-flop qubit are detuned by  $\delta_{\text{so}} = \epsilon_0 - \epsilon_{\text{ff}}$  but coupled with strength  $g_{\text{so}}$ .

For small detunings the coupling leads to a hybridization of the charge and spin states as shown in figure 2.6 with the ground state  $|\tilde{g}\rangle$  and two hybridized charge-spin excited states

$$|\tilde{g}\rangle = |g \downarrow\uparrow\rangle \quad (2.26)$$

$$|\tilde{e}_1\rangle = \beta|g \uparrow\downarrow\rangle + \alpha|e \downarrow\uparrow\rangle \quad (2.27)$$

$$|\tilde{e}_2\rangle = -\alpha|g \uparrow\downarrow\rangle + \beta|e \downarrow\uparrow\rangle. \quad (2.28)$$

We can determine these eigenvectors analytically by using eq. (2.18) and (2.19) with  $A = \delta_{\text{so}}$  and  $B = 2g_{\text{so}}$ . Here A describes the energy scale ( $\sigma_z$ ) and B drives the transitions ( $\sigma_x$ ).

Due to the detuning the flip-flop transition is a second-order process. Furthermore, as  $g_{\text{so}} \ll \delta_{\text{so}}$ , the system is in the dispersive regime. This means that the flip-flop transition experiences an AC Stark shift which can be calculated with second order perturbation theory to

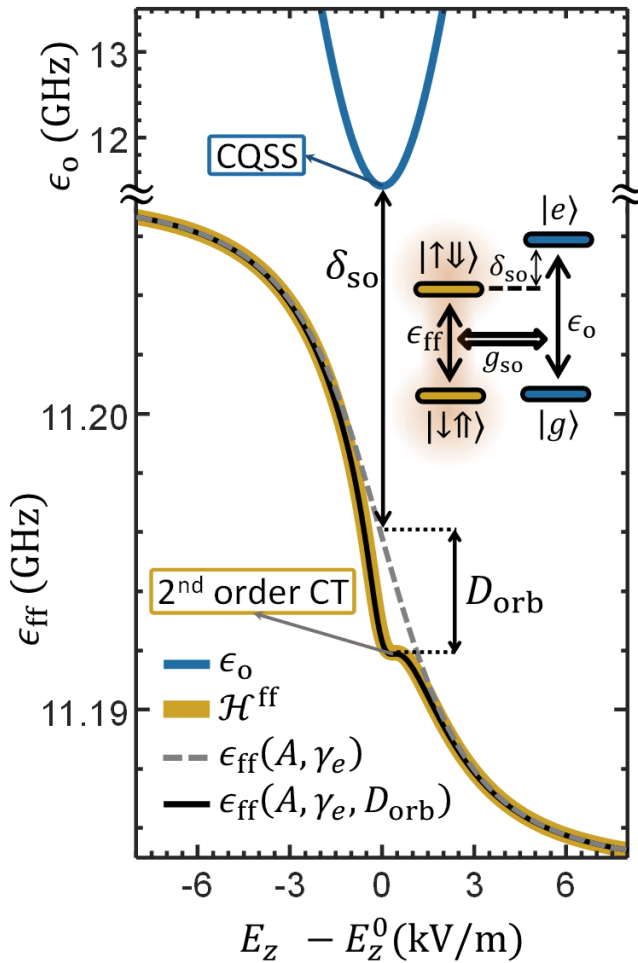


FIGURE 2.5: **Flip-flop qubit dispersion relation** Charge,  $\epsilon_0$ , and flip-flop,  $\epsilon_{\text{ff}}$ , qubits transition frequencies as a function of vertical electric field  $E_z$ , for  $B_0 = 0.4$  T,  $A = 117$  MHz,  $d = 15$  nm,  $\Delta_\gamma = -0.2\%$  and  $V_t = 11.44$  GHz. The inset shows the level diagram of flip-flop states coupled to charge states. CT stands for ‘clock transition’ and CQSS for ‘charge qubit sweet spot’.

$$D_{\text{orb}}(E_z) = \frac{|\langle \uparrow\downarrow g | H_{\text{orb}}^A | e \downarrow\uparrow \rangle \langle e \downarrow\uparrow | H_{\text{orb}}^A | g \uparrow\downarrow \rangle|}{E_{e\downarrow\uparrow} - E_{g\uparrow\downarrow}} \quad (2.29)$$

$$= \frac{[g_{\text{so}}(E_z)]^2}{\delta_{\text{so}}(E_z)},$$

[12], reducing the flip-flop qubit frequency to:

$$\epsilon_{\text{ff}}(A, \gamma_e, D_{\text{orb}}) = \epsilon_{\text{ff}}(A, \gamma_e) - D_{\text{orb}}(E_z). \quad (2.30)$$

Around  $E_z \approx E_z^0$  the charge qubit comes closest to the flip-flop qubit (see Fig. 2.5 while the coupling  $g_{\text{so}}$  is highest. Consequently  $D_{\text{orb}}(E_z)$  is largest. Plotting Eq. (2.30) (thin black line in Fig. 2.5a) agrees with the full numerical simulations of the Hamiltonian in Eq. (2.24).

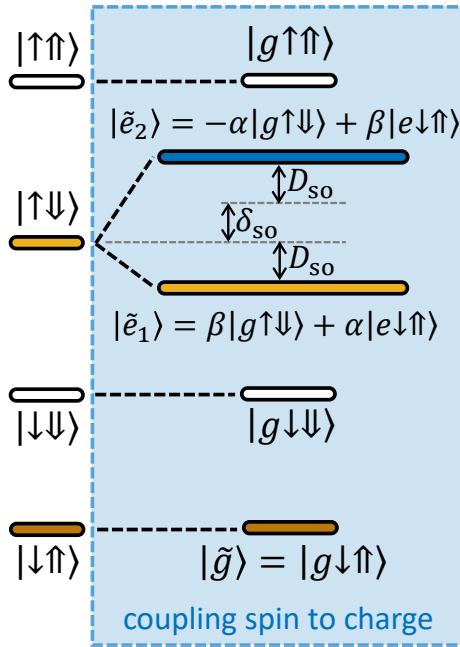


FIGURE 2.6: **Hybridized charge-flip-flop states** Level diagram showing the hybridization of the charge and flip-flop states due to the coupling  $g_{so}$  when the detuning  $\delta_{so}$  is small.

## 2.2 Electrical noise and relaxation

### 2.2.1 Dephasing due to electrical noise

Since our qubit is based on the use of electric fields, the presence of electric noise is a concern for the longevity of our qubit states. Generally, to achieve a high qubit performance one needs a high ratio of qubit coherence time to qubit gate operation time.

For the charge qubit we find that at the ionization point, the transition frequency exhibits a local minima equal to  $V_t$  and is thus first order insensitive to electrical noise  $\partial\epsilon_0/\partial E_z = 0$  (see figure 2.3), called a clock transition . However, we do not intent to operate the charge qubit as its dephasing rate still exceeds Hz.

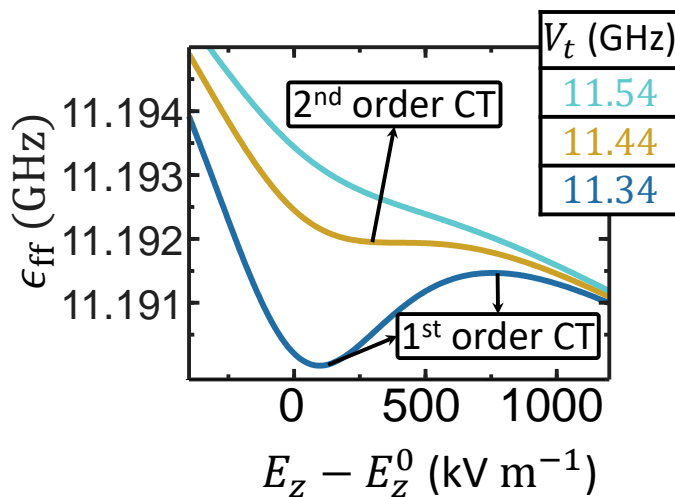


FIGURE 2.7: **Flip-flop dispersion for different tunnel couplings**  $E_z$ -dependence of flip-flop precession frequency for the three indicated tunnel coupling values.

Conveniently, the flip-flop qubit also exhibits a noise insensitive region close to the ionization point. The properties of this region depend on  $V_t$ . Figure 2.7 shows 3 different values of  $V_t$ . For low  $V_t$  the dispersive shift is strong due to the closeness of the charge qubit and thus creates two first order clock transitions. These merge into one for  $V_t = 11.44$  GHz. This creates a second-order clock transition and strongly reduces dephasing. Finally, for high  $V_t$  the dispersive shift is not strong enough and does not yield a minimum.



We estimate the dephasing from quasi-static  $E_z$  noise. This is noise with a spectral weight centred at frequencies smaller than the qubit resonance and Rabi frequency, aligned with the donor-dot direction. We assume  $E_{z,rms}^{\text{noise}} = 100$  V/m which corresponds to 1.5  $\mu$ eV charge detuning noise for  $d = 15$  nm. This is based on the following assumptions.

**Si/SiO<sub>2</sub> noise characteristics** The Si/SiO<sub>2</sub> interface is known to contain a number of defects and electron traps, which can generate charge noise and therefore degrade the operation of qubits sensitive to electric fields. Some experimental studies have extracted the trap density, in the middle of the silicon band gap, for the MOS devices we consider here [13]. It is known, experimentally and theoretically, that these charge fluctuators yield a  $1/\nu$  frequency dependence of the noise spectral density [14]. These models capture the averaged collective effect of many charge fluctuators on the qubit operation. In specific cases, one can occasionally encounter individual charge traps or fluctuators whose effect is more drastic than that of an overall  $1/\nu$  noise. However, it is usually possible experimentally to tune the electrostatic landscape of a nanoscale device in such a way that the individual trap is frozen, *i.e.* does not change its charge state while the qubit is operated. This results in a static shift in the local electric field that can be compensated with other gate voltages. In very rare occasions, a charge trap cannot be frozen while placing the qubit at its optimal operation point. In that case, the qubit will have to be considered faulty, and excluded from participating in the operations of the quantum processor.

In the general case where charge noise can be considered an average collective effect, it can be thought of as a quasi-static drift of the qubit electrostatic environment. Indeed, since individual gates take less than a microsecond, the qubit environment is usually static within a single gate, but fluctuates in between gates. The dephasing time  $T_2^*$  characterises the influences of these fluctuations on the qubit (see chapter 1.2.3). Experimentally, average quasi-static charge detuning noises around 1.9  $\mu$ eV are typically found in a range of semiconductor nanodevices, including SiGe [15]–[17], AlGaAs [18] and Si/SiO<sub>2</sub> [17], [19]. In particular, MOS structures were found recently [17] to have a charge noise spectrum similar to SiGe devices, around  $(0.5 \mu\text{eV})^2/\nu$ . Integrating over a quasi-static bandwidth relevant to experimental time-scales, say between 1 Hz and 1 MHz, yields 1.7  $\mu$ eV noise. In our simulations, given that the distance between the donor and interface sites is  $\sim 10$ –30 nm, a noise field of 100 V m<sup>−1</sup> would correspond to 1–3  $\mu$ eV charge detuning noise.

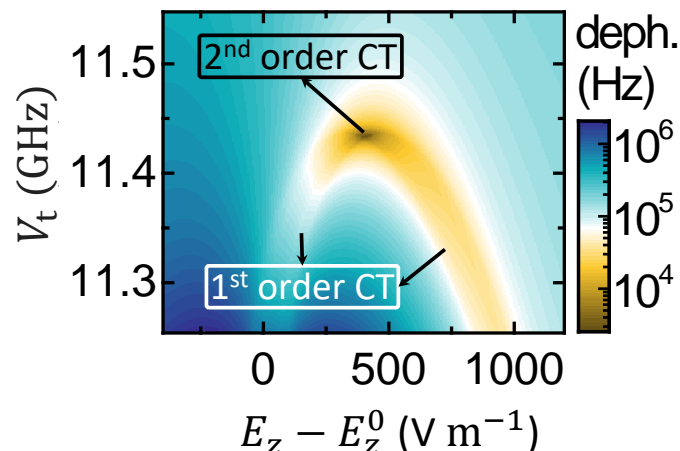


FIGURE 2.8: **Flip-flop dephasing** Estimated flip-flop qubit dephasing rate, assuming electric field noise  $E_{z,rms}^{\text{noise}} = 100$  V m<sup>−1</sup>.

**Dephasing** To estimate the dephasing resulting from this charge noise, we calculate the difference between the flip-flop transition frequency  $\epsilon_{\text{ff}}$  (transition between eigenstates closest to  $|g \downarrow\uparrow\rangle$  and  $|g \uparrow\downarrow\rangle$ ) and the transition frequencies  $\epsilon_{\text{ff}}^n$  that result when applying a uniformly distributed noise in the range  $E_z^n = \sqrt{3}[-E_{z,\text{rms}}, E_{z,\text{rms}}]$ . This gives

$$\text{Dephasing rate} = \sum_n |\epsilon_{\text{ff}} - \epsilon_{\text{ff}}^n| / N_n, \quad (2.31)$$

where  $N_n$  is the number of sampled  $E_z^n$  and  $\epsilon_{\text{ff}}^n$  is calculated for each value of  $E_z^n$ . The resulting dephasing rates are shown in figure 2.8.

The rates can be as low as  $1/T_2^* \approx 3$  kHz when at the second order clock transition. This is comparable to the dephasing of  $1/T_2^* \approx 1$  kHz due to magnetic noise in our qubits [4].

### 2.2.2 Relaxation

Relaxation can also inhibit qubit performance (see chapter 1.2.3). In silicon bulk donors the electron spin lattice relaxation time is  $T_1 \gg 1$  s due to very weak coupling between the phonons and the spins. However, according to Ref. [20], for the charge and the flip-flop qubit the difference in valley population between the interface and donor state causes a potential energy difference that leads to an effective electron-phonon coupling and to relaxation, even for a uniform phonon-induced relaxation. Basically, the relaxation is "valley-enhanced" due to the non-trivial valley structure of the electron-phonon interaction. The charge qubit relaxation rate is  $1/T_{1,c} \approx 0.49$  MHz at the ionization point and increases with higher  $\epsilon_0$ . In the dispersive regime  $\delta_{\text{so}} \gg g_{\text{so}}$  the flip-flop relaxation directly relates to the charge qubit relaxation. It is equal to the amount of charge excited state in the flip-flop eigenstates times the charge qubit relaxation rate which gives

$$1/T_{1,\text{ff}} = (g_{\text{so}}/\delta_{\text{so}})^2 / T_{1,o}, \quad (2.32)$$

with

$$1/T_{1,c} = \Theta \epsilon_0 V_t^2, \quad (2.33)$$

where  $T_{1,c}$  is the charge qubit lifetime and  $\Theta \approx 2.37 \times 10^{-24} \text{ s}^2$  is determined by the silicon crystal properties [20].

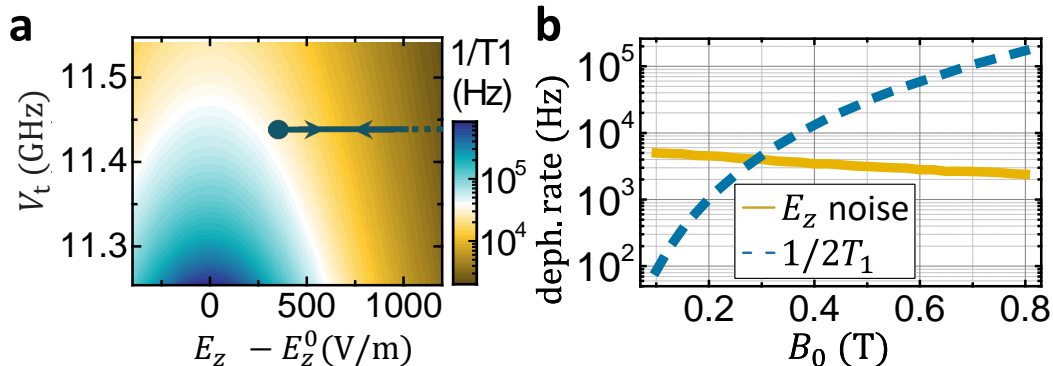


FIGURE 2.9: **Flip-flop relaxation rate.** **a** Flip-flop qubit relaxation rate, with arrows indicating the adiabatic path used for  $z$ -gates. **b** Flip-flop qubit dephasing rate due to  $E_z$  noise and relaxation at 2<sup>nd</sup>-order CTs for each  $B_0$ .

Figure 2.9a shows the flip-flop relaxation rate depending on the tunnel coupling and the applied electric field. The larger the detuning, the smaller is the component of admixed excited eigenstate  $|e \downarrow\uparrow\rangle$  and consequently the relaxation. At our proposed operating point at the second order clock transition, the relaxation rate is  $1/T_{1,\text{ff}} \sim 10$  kHz. This indicated that the qubit dephasing will be relaxation limited  $1/T_2^* = 1/2T_1$ . However, the relaxation rate depends on the external magnetic field with the power-law relation  $1/T_{1,\text{ff}} \sim B^3$  [20]. Thus reducing the magnetic field, suppresses the relaxation strongly. Figure 2.9b shows the

dephasing due to electric noise and relaxation. We find that for  $B_0 < 0.3$  T, the dephasing is no longer  $T_1$  dominated.

### 2.2.3 Tunnel coupling tuning

Tuning the flip-flop qubit, e.g. into a clock transition, requires the ability to tune the tunnel coupling  $V_t$ .  $V_t$  is difficult to control at the fabrication stage, given its exponential dependence on donor depth, together with oscillations at the atomic scale [6] arising from a similar valley interference effect as the one afflicting the exchange interaction [21].

Ion-implanting a donor at  $z_d \approx 15$  nm below the interface happens with a vertical uncertainty of order  $\pm 10$  nm (ref. [22]), resulting in more than 2 orders of magnitude uncertainty in  $V_t$  (ref. [6]). Therefore, it is crucial to implement a method to tune  $V_t$  *in situ*. A possible solution is to displace the location of the interface wavefunction laterally, which in turn modifies the overlap between the donor and interface wavefunctions and therefore reduces  $V_t$ . This can be done by adding two gates on either side of the top gate which pulls the donor electron to the interface (Fig. 2.10a), in such a way that a relative voltage between the gates can modify the interface lateral potential landscape.

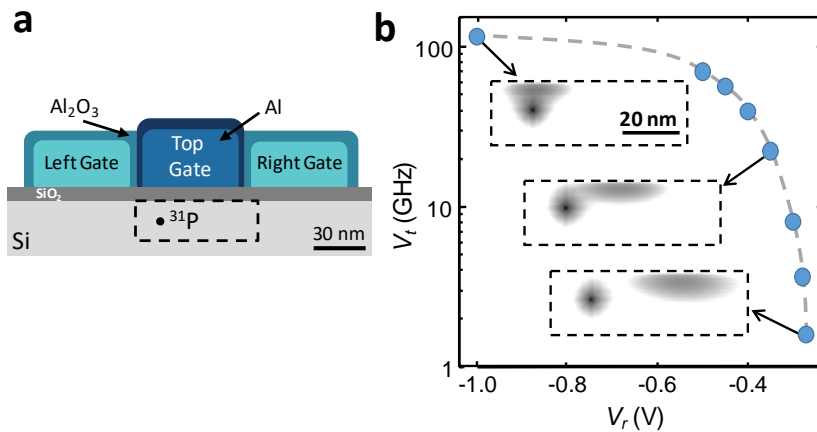


FIGURE 2.10: **Tunnel coupling tuning.** **a** Device structure to tune the tunnel coupling  $V_t$  of the charge qubit by applying lateral voltages. **b**,  $V_t$  as a function of right gate voltage, calculated using a finite element Poisson solver (Synopsis® TCAD) and atomistic tight binding (NEMO-3D, ref. [7], [8]). The insets illustrate the NEMO-3D wavefunctions for three right gate voltages  $V_r = -1, -0.35$  and  $-0.27$  V. The left gate voltage is  $V_l = -0.5$  V for all the simulations, and the top gate is biased such that the position of the electron is in between the donor and interface. The donor is assumed to be  $z_d = 9.2$  nm below the Si/SiO<sub>2</sub> interface.

This gate stack is identical to the well-established scheme for the confinement of single electrons in Si quantum dots [23]. This technique allows  $V_t$  to be reduced by at least 2 orders of magnitude (Fig. 2.10b), therefore circumventing the uncertainty in donor depth and  $V_t$  arising from ion-implantation.

Note that, when moving the interface wavefunction laterally to tune  $V_t$ , the electric dipole acquires some horizontal component. In this case, the detuning noise is caused by the noise component along the donor-interface states direction.

### 2.2.4 Adiabatic phase control

To incorporate flip-flop qubits in a quantum processor, the presence of slow dephasing regions is important to control the qubit phase with high fidelity and extend the qubit lifetime. Therefore, idle qubits are decoupled from electric fields by fully displacing the electron either to the interface or to the donor to minimize dephasing. Operations are performed close to the ionization point. Consequently, we need to displace the electron, which in turn changes its precession frequency (Fig. 2.5). As a result, the accumulated phase must be corrected after quantum operations. This is optimally done by moving the electron to the 2<sup>nd</sup>-order

clock transition, therefore minimizing dephasing errors. At this point, the flip-flop qubit phase precesses  $\sim \Delta_\gamma \gamma_e B_0 / 2 - D_{\text{orb}} \sim \text{GHz}$  faster than its idle point, and therefore any phase correction in a  $2\pi$  period can be applied within tens of ns. The dephasing rate at the clock transition, on the order of a few kHz, would cause very small errors ( $< 10^{-4}$ ). However, while moving the electron from the interface towards the donor, the flip-flop qubit goes through regions of fast dephasing (Fig. 2.8), and therefore this operation has to be performed as quickly as possible. It also has to be slow enough as to avoid errors due to non-adiabaticity, which include *e.g.* leakage to unwanted high-energy states. These errors depend on the adiabatic factor  $K$ , which quantifies the fractional rate of change of the system's eigenstates (the higher the value of  $K$ , the more adiabatic and slower is the process).  $K$  is defined, in units of rad/s, as

$$K = \left| \frac{\omega_{\text{eff}}}{\dot{\alpha}} \right| \gg 1, \quad (2.34)$$

given a time-dependent Hamiltonian in a two-dimensional Hilbert space,

$$\mathcal{H}_2 = \Delta(t)\sigma_z + \Omega(t)\sigma_x, \quad (2.35)$$

where  $\omega_{\text{eff}} = \sqrt{\Delta^2 + \Omega^2}$  is the instantaneous transition angular frequency between eigenstates, and  $\dot{\alpha}$  is the rate of change of the orientation of  $\omega_{\text{eff}}$  ( $\alpha = \arctan(\Omega/\Delta)$ ) [24].

It follows from Eq. 2.34 that

$$K = \frac{(\Delta^2 + \Omega^2)^{3/2}}{|\dot{\Delta}\Omega - \dot{\Omega}\Delta|} \gg 1, \quad (2.36)$$

We use eq. (2.36) to determine the incremental sweep time step that satisfies the adiabatic condition at any given point in  $E_z$

$$dt = K \frac{|d\Delta \cdot \Omega - d\Omega \cdot \Delta|}{(\Delta^2 + \Omega^2)^{3/2}} \quad (2.37)$$

where  $d\#$  signifies incremental steps in  $E_z$ . Although the transition process involves multiple levels, we apply Eq. 2.36 as an approximation of adiabaticity. This is confirmed to be always valid by checking that the leakage errors are kept below a target level. We use  $\Delta_c = \pi e(E_z - E_z^0)d/h$  and  $\Omega_c = \pi V_t$  to find  $dt_c$  for the charge qubit, and  $\Delta_{\text{so}} = \pi \delta_{\text{so}}$  and  $\Omega_{\text{so}} = 2\pi g_{\text{so}}$  to find  $dt_{\text{so}}$  for the spin-charge coupling. For a chosen adiabatic factor  $K$ , we then find  $E_z(t)$  by satisfying the condition  $\max(dt_{\text{so}}, dt_c) = dt$ .

In Fig. 2.12a we plot the time dynamics of an initial state  $|g\rangle \otimes (|\downarrow\uparrow\rangle + |\uparrow\downarrow\rangle)/\sqrt{2}$  while sweeping  $E_z$  adiabatically to move the electron from the interface to the 2<sup>nd</sup>-order clock transition and back, in order to realize a  $\pi$   $z$ -gate. Setting  $K = 50$  eq. (2.37) gives time steps as shown in Figure 2.11. This results in an initial adiabatic setup consisting of a fast sweep (0.8 ns), allowed by the large charge qubit splitting when  $E_z \gg E_z^0$ , followed by a slower sweep (3.5 ns), limited by the proximity of excited charge states to the flip-flop qubit when  $E_z \approx E_z^0$ . The electron then remains at the clock transition for 60 ns to perform the gate to correct for the phase shift, according to

$$t_\pi = \frac{\text{gate}/2\pi - \int_{t_0}^{t_{\text{end}}} \nu(E_z(t)) - \nu(E_z(t_0)) dt}{\nu(E_z(t_{\text{end}})) - \nu(E_z(t_0))} \quad (2.38)$$

where  $\text{gate} = \pi$  and  $t_{\text{end}} = 4.3$  ns. Afterwards we move it adiabatically back to the interface. We calculate the expectation values for the flip-flop  $z$ -state  $\langle \sigma_z^{\text{ff}} \rangle$ , the flip-flop  $x$ -state  $\langle \sigma_x^{\text{ff}} \rangle = |+_x^{\text{ff}}\rangle\langle+_x^{\text{ff}}| - |-_x^{\text{ff}}\rangle\langle-_x^{\text{ff}}|$ , where  $|+_x^{\text{ff}}\rangle = (|\uparrow\downarrow\rangle + \exp(-i2\pi\epsilon_{\text{ff}}^{t=0})|\downarrow\uparrow\rangle)/\sqrt{2}$  and  $|-_x^{\text{ff}}\rangle = (|\uparrow\downarrow\rangle + \exp(-i2\pi\epsilon_{\text{ff}}^{t=0} - i\pi)|\downarrow\uparrow\rangle)/\sqrt{2}$ , the electron position  $\langle \sigma_z \rangle$  and the charge qubit excitation  $\langle |e\rangle\langle e| \rangle$  by determining the time evolved eigenstates of our system Hamiltonian

$$|\psi(t)\rangle = e^{-i\mathcal{H}_{\text{ff}}t/\hbar}|\psi(t_0)\rangle \quad (2.39)$$

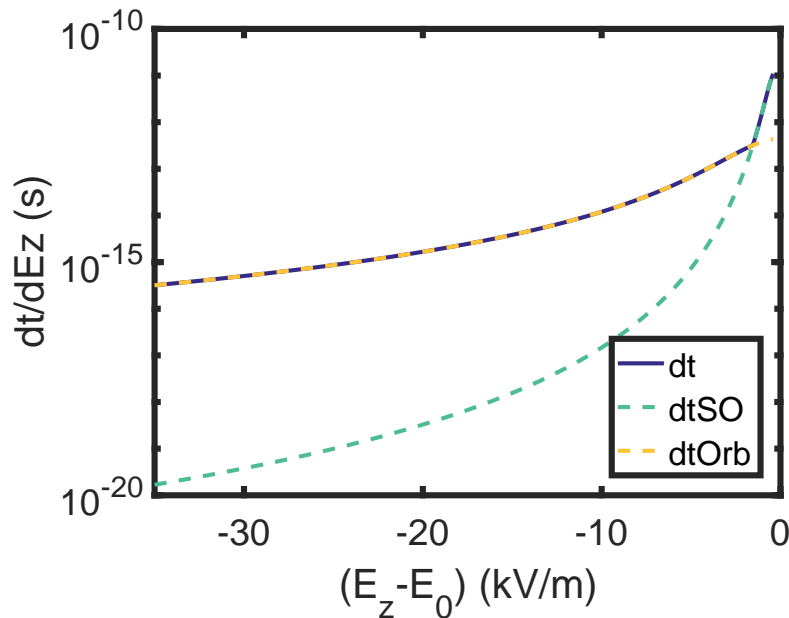


FIGURE 2.11: **Z-gate adiabaticity time step for each electric field  $E_z$ .** Time step for each electric field  $E_z$  that full fills the adiabaticity criterion from eq. (2.36).

where  $\langle \# \rangle = \langle \psi(t) | \# | \psi(t) \rangle$  as the expectation value. Indeed during the 69 ns the flip-flop phase  $\pi$ -gate is performed while keeping both the flip-flop and charge excitation minimal. Fast oscillations between the charge and flip-flop states are due to small deviations from perfect adiabaticity.

The adiabatic errors (without noise) of an adiabatic unitary process  $U_{\text{ideal}}$ , expressing leakage to other states, can be calculated by averaging the fidelity of the actual process  $U$  over a set of initial states  $|j\rangle$ ,

$$\text{Adiabatic error} = 1 - \sum_{|j\rangle} \left| \langle j | U^\dagger U_{\text{ideal}} | j \rangle \right|^2 / N_j, \quad (2.40)$$

where  $N_j$  is the number of initial states. For this 1-qubit gate, we choose  $|j\rangle = \{|g\downarrow\uparrow\rangle_e, |g\uparrow\downarrow\rangle_e, (|g\downarrow\uparrow\rangle_e + |g\uparrow\downarrow\rangle_e)/\sqrt{2}, (|g\downarrow\uparrow\rangle_e + i|g\uparrow\downarrow\rangle_e)/\sqrt{2}\}$  and  $N_j = 4$ .

These errors can be controlled with the factor  $K$ , which determines the setup time (see Fig. 2.12b).

Quasi-static  $E_z$  noise can increase errors, due to dephasing (Fig. 2.12c). At realistic noise levels ( $100 \text{ V m}^{-1}$ ), the gate error rate is found to be  $< 10^{-4}$ . Similar error levels arise due to relaxation, which remains below  $3 \cdot 10^4 \text{ Hz}$  (Fig. 2.9).

Note that the presence of clock transitions does not affect the ability to use  $E_{\text{ac}}$  to resonantly drive the qubit, since the transverse term  $A(E_z)$  still responds fully to the electric field (this is similar to the case of magnetic clock transitions, e.g. in Si:Bi [25]).

## 2.3 Electric drive

We can achieve high-fidelity one-qubit  $x(y)$ -gates with an electric drive of the flip-flop qubit as illustrated in figure 2.13(a). The fastest 1-qubit gates are obtained when the electron is around the ionization point, where  $\partial A / \partial E_z$  is maximum (Fig. 2.4). A vertical oscillating electric field of amplitude  $E_{\text{ac}}$  is applied in resonance with the flip-flop qubit, *i.e.*,  $\nu_E = \epsilon_{\text{ff}}$ . This renders  $\mathcal{H}_A(t)$  time-dependent with a component  $A_{\text{ac}} \cos(2\pi\nu_E t)$ , resulting in a coupling rate

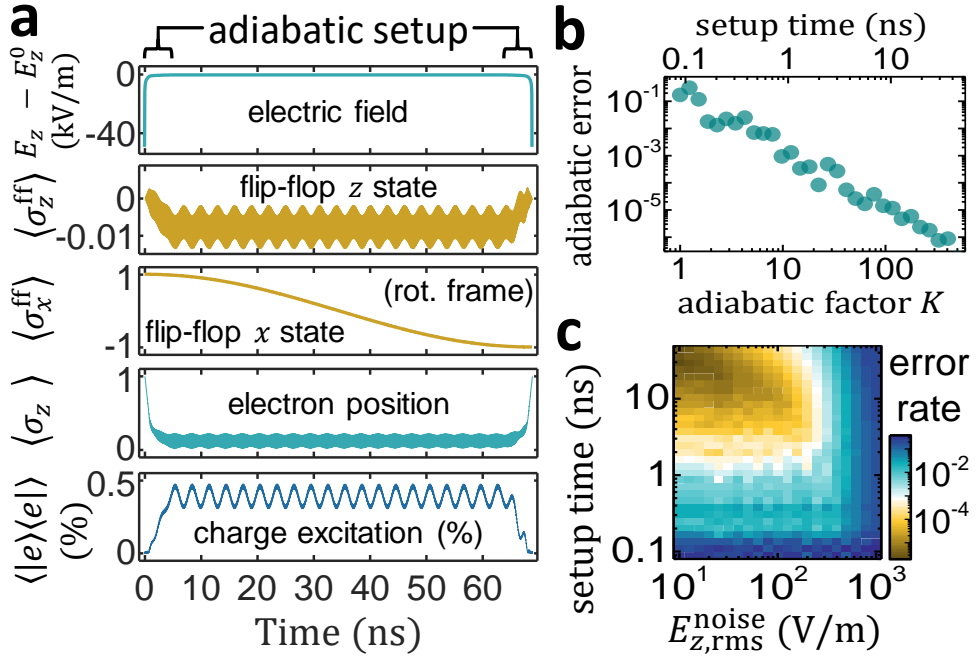


FIGURE 2.12: **High-fidelity adiabatic  $z$ -gates.** **a**, Time-evolution of an adiabatic ( $K = 50$ )  $\pi$   $z$ -gate on state  $|g\rangle \otimes (|↓↑⟩ + |↑↓⟩)/\sqrt{2}$ , showing applied electric field and flip-flop/charge states. Outer brackets denote the expectation value of an operator.  $\sigma_z^{\text{ff}} = |↑↓⟩\langle↑↓| - |↓↑⟩\langle↓↑|$  and  $\sigma_x^{\text{ff}} = |+^{\text{ff}}_x\rangle\langle+^{\text{ff}}_x| - |-^{\text{ff}}_x\rangle\langle-^{\text{ff}}_x|$ , where  $|+^{\text{ff}}_x\rangle = (|↑↓⟩ + \exp(-i2\pi\epsilon_{\text{ff}}^t)|↓↑⟩)/\sqrt{2}$  and  $|-^{\text{ff}}_x\rangle = (|↑↓⟩ + \exp(-i2\pi\epsilon_{\text{ff}}^t - i\pi)|↓↑⟩)/\sqrt{2}$ . **b**,  $\pi$   $z$ -gate leakage error for different adiabatic setup times, which are set by the factor  $K$ . **c**,  $\pi$   $z$ -gate error due to quasi-static  $E_z$  noise, at the 2<sup>nd</sup>-order CT at  $B_0 = 0.4$  T, for different noise amplitudes and adiabatic setup times.

$$g_E^{\text{ff}} = A_{\text{ac}}/4. \quad (2.41)$$

The oscillation strength  $A_{\text{ac}}$  depends on the driving electric field, described by the Hamiltonian

$$H_E = E_{\text{ac}} \cos(2\pi\nu_E t) \sigma_z \quad (2.42)$$

where  $E_{\text{ac}}$  is the electric drive amplitude. The coupling of this electric field to the charge qubit is then determined by

$$g_E = \langle g | H_E | e \rangle \quad (2.43)$$

$$= \frac{eE_{\text{ac}}d}{4h} \langle g | \sigma_z | e \rangle \quad (2.44)$$

$$= \frac{eE_{\text{ac}}d}{4h} \frac{V_t}{\epsilon_0}. \quad (2.45)$$

This coupling rate corresponds to half the Rabi frequency in the one-photon limit. Furthermore, in every case of resonant driving we assume a linearly polarized field, resulting in a Rabi frequency that equals half the dipole matrix element times the driving field amplitude (rotating-wave approximation). This explains the factors of 4 appearing in all the formulas for coupling rates.

Figure ?? (b) portrays the energy level diagram for the electric drive. A large detuning  $\delta_{\text{so}} \gg g_{\text{so}}$  (Fig. ??b) between the charge and flip-flop qubit ensures the least amount of the charge excited state  $|e\rangle$  in the flip-flop qubit eigenstates, minimizing qubit relaxation via

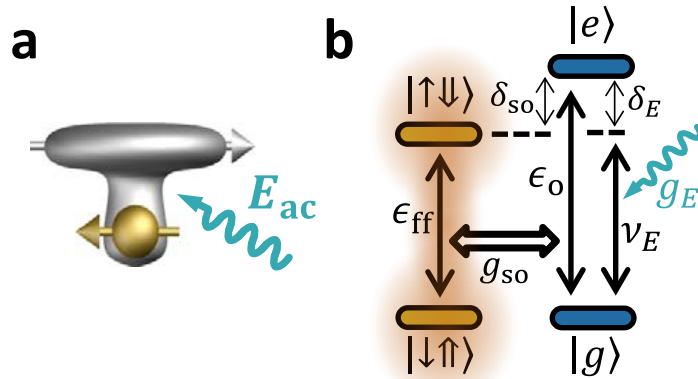


FIGURE 2.13: **Electric drive of the flip-flop qubit.** **a**, Spatial representation and **b**, level diagram, for electrical drive of a flip-flop qubit, showing partially ionized electron wavefunction and spin arrows.

charge-phonon coupling. The flip-flop qubit is still driven, via a second-order process, at a rate (half-Rabi frequency) given by second order perturbation theory to:

$$g_E^{\text{ff}} = \frac{|\langle \uparrow\downarrow g | H | e \downarrow\uparrow \rangle \langle e \downarrow\uparrow | H | g \uparrow\downarrow \rangle|}{E_{e\downarrow\uparrow} - E_{g\uparrow\downarrow}} \quad (2.46)$$

$$= \frac{g_{\text{so}} g_E}{2} \left( \frac{1}{\delta_{\text{so}}} + \frac{1}{\delta_E} \right), \quad (2.47)$$

where  $\delta_E = \nu_E - \epsilon_o$ . Equation 2.46 provides another explanation of why the fastest 1-qubit gates are obtained when the electron is at the ionization point:  $\delta_{\text{so}}$  and  $\delta_E$  are minimum ( $\epsilon_o$  is minimum), and  $g_{\text{so}}$  and  $g_E$  are maximum (Eqs. 2.9 and 2.43).

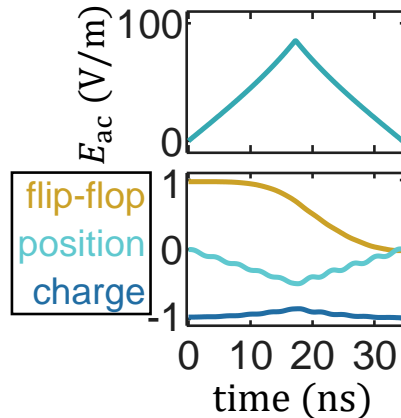


FIGURE 2.14: **Adiabatic flip-flop electric drive** Time-dependent adiabatic drive amplitude and qubit dynamics of a  $\pi/2$   $x$ -gate, for  $K = 30$ ,  $B_0 = 0.4$  T,  $E_z = E_z^0$  and  $V_t = 11.5$  GHz. Right plot shows flip-flop z state,  $\langle \sigma_z^{\text{ff}} \rangle$ , electron position,  $\langle \sigma_z \rangle$ , and charge qubit state,  $\langle |e\rangle \langle e| - |g\rangle \langle g| \rangle$ .

The electrical drive can cause some excitation of the charge qubit. It is therefore convenient to turn  $E_{\text{ac}}$  on/off adiabatically to make sure the charge is de-excited at the end of the gate. Figure 2.14 shows the  $E_{\text{ac}}$  time evolution needed for a  $\pi/2$   $x$ -gate. The adiabatic increase of  $E_{\text{ac}}(t)$  is calculated with eq. (2.36) with  $\Delta_E = \pi\delta_E$  and  $\Omega_E = 2\pi g_E$  where we have

assumed an adiabatic factor  $K = 30$ , sufficient for leakage errors  $< 10^{-3}$ . Once  $E_{ac}(t)$  has been determined, we employ Floquet theory to calculate time evolution of the Hamiltonian which now changes with every time step.

Floquet theory says that semi-classical theory provides results that are equivalent to full quantum theory in cases of driving fields interacting with a (qubit) system when fluctuations in the phonon number can be neglected **floquet**. For a periodic Hamiltonian  $H(t) = H(t + T)$  with  $T$  we define the time propagator as

$$|\psi(t)\rangle = K(t, t_0)|\psi(t_0)\rangle, \quad (2.48)$$

with  $K(t_0, t_0) = 1$ . We can use the propagator over a full period  $K(T, 0)$  to construct a time evolution over many multiples  $n$  of the fundamental period

$$K(nT, 0) = [K(T, 0)]^n \quad (2.49)$$

This can be used when de-constructing the adiabatic evolution into many small time steps which result in the final time-evolved operator  $H$ . This can then be used to calculate the expectation values of flip-flop z-state  $\langle \sigma_z^{ff} \rangle$ , the electron position  $\langle \sigma_z \rangle$  and the charge qubit state  $\langle |e\rangle\langle e| - |g\rangle\langle g| \rangle$ . In our  $\pi/2$  x-gate,  $E_{ac}$  increases steadily until a  $\pi/4$  rotation is completed, after which  $E_{ac}$  is gradually switched off to achieve the gate. Meanwhile, an average 4% excitation of the charge qubit causes a  $\sim 4 \cdot 10^4$  Hz relaxation rate of the encoded quantum state (Eq. 2.33), or error levels close to  $10^{-3}$ .

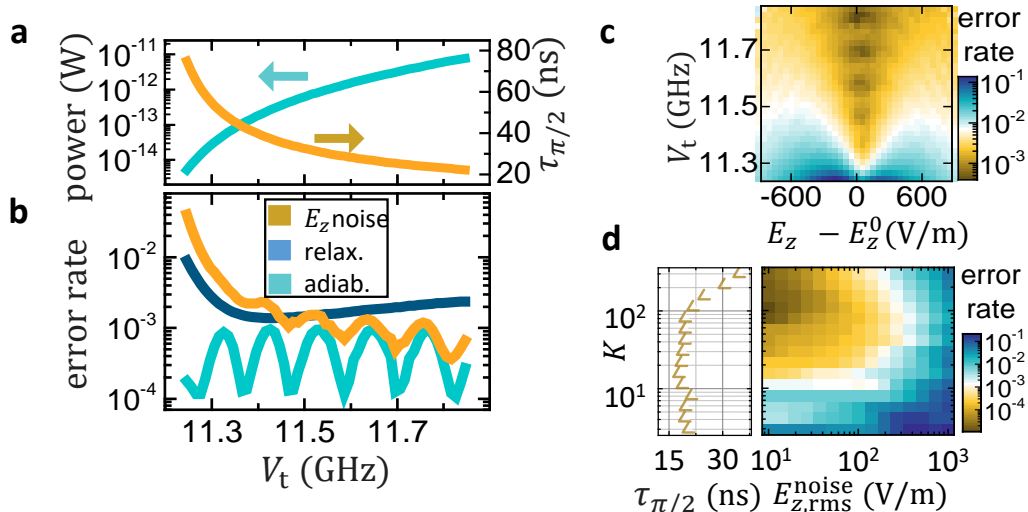


FIGURE 2.15: **Adiabatic gate errors.** **a** Averaged drive power and gate time for the parameters  $K = 30$ ,  $B_0 = 0.4$  T,  $E_z = E_z^0$  and  $V_t = 11.5$  GHz. For the same parameters, **b** the error rates for different  $V_t$ . To estimate the drive power, we assumed a  $50\ \Omega$  line in which a  $1\text{-V}$  AC voltage produces a  $10\text{ V m}^{-1}$  AC vertical electric field. **c**, Estimated flip-flop qubit  $\pi/2$  x-gate error due to quasi-static noise with amplitude  $E_{z,rms}^{noise} = 100\text{ V m}^{-1}$ . **d**, Dependence of the gate error rate on the electric noise r.m.s. amplitude and adiabatic factor  $K$  (which sets the gate time).

We then investigate in figure 2.15(a) how the total  $\pi/2$  x-gate errors depend on the biasing of the electron wavefunction by calculating the adiabatic error from eq. (2.40) and the error from quasi-static  $E_z$  noise from

$$\text{Noise error} = 1 - \sum_{n, |j\rangle_n} \left| \langle j|_n U_n^\dagger U_{n,\text{ideal}} |j\rangle_n \right|^2 / (N_j N_n) \quad (2.50)$$

where  $|j\rangle = \{|g\downarrow\uparrow\rangle_e, |g\uparrow\downarrow\rangle_e, (|g\downarrow\uparrow\rangle_e + |g\uparrow\downarrow\rangle_e)/\sqrt{2}, (|g\downarrow\uparrow\rangle_e + i|g\uparrow\downarrow\rangle_e)/\sqrt{2}\}$  and  $N_j = 4$ .

At the ionization point,  $E_z = E_z^0$ , error levels close to  $10^{-3}$  are found over a wide range of  $V_t$ . The  $K = 30$  choice ensures adiabatic errors  $< 10^{-3}$  with an oscillatory character typical

of adiabatic processes [26]. At small  $V_t$  (and therefore small detuning  $\delta_{\text{so}}$ ), the qubit eigenstates contain a substantial amount of charge, causing more errors due to charge-phonon relaxation. Increasing the detuning  $\delta_E$  with larger  $V_t$  allows for a faster adiabatic sweep and higher powers (Fig. 2.15(b)), yielding shorter gate times and therefore less errors due to quasi-static noise. Still, the incident power is at least three orders of magnitude lower than the one needed to drive donor electron spin qubits, at the same Rabi frequency, with oscillating magnetic fields [3], [4].

As Fig. 2.15(a) shows, low error rates are still available away from the ionization point, even though best values are found at  $E_z = E_z^0$ . This is because our gate times are so fast that dephasing, and therefore CT's, do not play a crucial role. Instead, quasi-static  $E_z$  noise cause errors mainly by modulating the driving strength  $g_E^{\text{ff}}$ , causing “gate time jitter”. Indeed, the gate time is sensitive to the orbital transition frequency  $\epsilon_o$  (Eq. 2.46), and therefore gate errors are minimized close to the charge qubit sweet spot (CQSS), where  $\partial\epsilon_o/\partial E_z = 0$  (Fig. 2.8).

Finally, as Fig. 2.15(c) shows, lower quasi-static  $E_z$  noise can cause less errors, provided that the adiabatic factor  $K$  is increased, to reduce leakage errors, up to an optimum value where gate times are still fast as to keep noise errors low. Relaxation errors could also be reduced by reducing  $B_0$  (recall Fig. 2.9).

A number of other noise sources can also affect the qubits. Another source of electric field noise can be the thermal and electrical noise produced by the metallic gates on top of the qubits, and the room-temperature instruments they connect to. An  $R = 50 \Omega$  resistor at room temperature produces Johnson-Nyquist noise with an r.m.s voltage  $\sqrt{4k_B T R \Delta\nu}$ . Therefore a quasi-static bandwidth  $\Delta\nu \sim 10^6$  Hz produces  $\sim 1 \mu\text{V}$  voltage noise, which is equivalent to  $E_{z,\text{rms}}^{\text{noise}} \sim 10 \text{ V m}^{-1}$ , or errors  $< 10^{-5}$  (Fig. 2.15c). Furthermore, because of the very low powers required by the electrically-driven 1-qubit gates and adiabatic shuttling, it is possible to insert abundant low-temperature attenuation along the high-frequency lines, and therefore the relevant temperature for the Johnson-Nyquist noise is well below room temperature. On the other hand, being close to a metallic interface, our qubit will be subject to evanescent wave Johnson noise (EWJN) due to vacuum and thermal fluctuations. Assuming the qubit is  $z = 15 \text{ nm}$  under aluminum gates at  $T = 100 \text{ mK}$  ( $\sigma = 1.4 \times 10^8 \text{ S m}^{-1}$  conductivity **Dehollain2013S**), a quasi-static bandwidth  $\Delta\nu \approx 10^6$  Hz produces **Henkel1999S**  $\sqrt{k_B T \Delta\nu / (2z^3 \sigma)} \sim 0.04 \text{ V m}^{-1}$  r.m.s. electric field noise, therefore negligible. We conclude that the main source of quasi-static noise will be charge noise with a typical  $1/\nu$  spectrum. Consistently with recently measured for Si/SiO<sub>2</sub> interfaces **Freeman2016S**, we assume the power spectral density to be  $S_c(\omega) \approx 10^4 / (6\omega)$ , in units of  $\text{V}^2 \text{ m}^{-2} \text{ rad}^{-1} \text{ s}$ .

So far we have only considered quasi-static noise. The presence of some residual amount of high-frequency noise could possibly lead to errors while performing quantum operations. Below we discuss these high-frequency sources, finding that they will cause much smaller errors compared to quasi-static noise.

In general, a driven qubit Rabi-oscillates with a decay envelope function given by **Bylander2011S**  $\zeta(t) \exp(-\Gamma_R t)$ , where  $\zeta(t)$  represents decay due to quasi-static detuning noise and  $\Gamma_R$  the exponential Rabi decay rate, which combines the qubit relaxation rate,  $\Gamma_1$ , the inverse of the gate time jitter due to quasi-static noise,  $\Gamma_1^{\Delta}$ , the inverse of the gate time jitter due to noise at the drive frequency,  $\Gamma_1^{\nu}$ , (the last three yield  $T_{2\rho}$  in the dressed qubit picture **Laucht2016S**) and the decay rate due to detuning noise at the Rabi frequency,  $\Gamma_{\Omega}$  (which equals the inverse of  $T_{1\rho}$  in the dressed qubit picture **Yan2013S**, **Laucht2016S**).

The effects of  $\zeta(t)$ ,  $\Gamma_1$  and  $\Gamma_1^{\Delta}$  have already been discussed extensively in this manuscript, with corresponding error levels below  $10^{-3}$ . We now focus on errors due to high-frequency noise sources, corresponding to decay rates  $\Gamma_1^{\nu}$  and  $\Gamma_{\Omega}$ .

Vertical (thus parallel to the driving field  $E_{\text{ac}}$ ) noise at the qubit resonance frequency ( $\sim 10^{10}$  Hz) would cause transitions between the qubit eigenstates – essentially a spurious excitation/relaxation process driven by noise – at a rate  $\Gamma_1^{\nu}$ . This noise can be caused *e.g.* by charges fluctuating in resonance with the qubit or by voltage noise at the metallic gates. This includes vacuum fluctuations, especially since the qubit frequency is generally higher than the corresponding device temperature. Also, during gate operations, the portion of the noise spectrum around the qubit frequency can add incoherently to the external resonant drive, causing the gate time to fluctuate. For the flip-flop qubit, the Rabi decay rate is given by  $\Gamma_1^{\nu} =$

Error levels at different spectral bandwidths			
Noise source	Quasi-static ( $<10^6$ Hz)	Rabi ( $\sim 10^7$ Hz)	Qubit ( $\sim 10^{10}$ Hz)
1/f vertical ( $E_z$ )	$10^{-3}$	$< 10^{-4}$	$10^{-4}$
1/f horizontal ( $E_{x,y}$ )	$10^{-4}$	$< 10^{-5}$	-
Charge-phonon relaxation	-	-	$10^{-3}$
Johnson-Nyquist	$<< 10^{-5}$	$< 10^{-5}$	$< 10^{-4}$
EWJN	-	$< 10^{-6}$	$< 10^{-4}$

TABLE 2.1: **Gate errors for different noise sources** Hyphens indicate non-existent or negligible errors.

$(\pi/2)(\mu_e^{\text{ff}}/\hbar)^2 S(2\pi\epsilon_{\text{eff}})$ , where  $\mu_e^{\text{ff}} = ed\langle g_{\text{so}}/\delta_{\text{so}} \rangle$  is the average flip-flop qubit electric dipole moment and  $S(2\pi\epsilon_{\text{eff}})$  is the noise power spectral density at the qubit angular frequency (in units of  $\text{V}^2 \text{ m}^{-2} \text{ rad}^{-1} \text{ s}$ ). Note that this flip-flop electric dipole is much smaller than the charge dipole, which in turn makes it less susceptible to electrical noise. This happens because, in our gate scheme, the charge dipole is only used as a second-order enabler, and therefore charge excitation is greatly minimized (Figs. 2.12a, ??c and 2.19a). In case of charge noise,  $S_c(\omega) = 10^4/(6\omega)$ , which gives  $\Gamma_1^v \sim 10^4$  Hz. This implies  $\pi/2$   $x$ -gate errors  $\sim 10^{-4}$ . There could also be vacuum fluctuations of charge traps, which could also generate errors due to relaxation. We do not know of any experimental measurement of such a noise for semiconductor nanostructures. For superconducting charge qubits, it has been found that charge noise increases linearly at frequencies beyond the thermal bath **Astafiev2004S**, which has been explained in terms of two-level coherent charge fluctuators **Shnirman2005S**. If a similar phenomenon afflicts our qubits, those quantum fluctuations will play an important role beyond  $\sim 2$  GHz (100 mK), implying that, at 10 GHz, relaxation can be up to 25 times faster. This can increase relaxation error rates to  $\sim 10^{-3}$ . In case of Johnson-Nyquist noise,  $S_{\text{JN}}(\omega) = 2 \times 10^{14} R \hbar \omega \pi^{-1} (e^{\hbar \omega / k_B T} - 1)^{-1}$  (where we have used  $\partial E_z / \partial V = 10^7 \text{ m}^{-1}$ , typical in MOS nanostructures). Because of the very low powers required by the electrically-driven 1-qubit gates ( $< 1$  pW), it is possible to insert abundant low-temperature attenuation along the high-frequency lines, insuring that the gates are well thermalized, and the noise of the room-temperature electronics greatly attenuated. A noise temperature  $T = 100$  mK would give  $\Gamma_1^v < 10^4$  Hz, and therefore error rates  $< 10^{-4}$ . Finally, in case of EWJN at  $T = 100$  mK, the  $10^{10}$  Hz part of the spectrum is **Henkel1999S, Poudev2013S**  $S_{\text{EW}}(\omega) \approx \hbar \omega / (4\pi z^3 \sigma)$ . This would give  $\Gamma_1^v < 10^4$  Hz, therefore again error rates  $< 10^{-4}$ .

Noise at the Rabi frequency ( $\Omega_R > 10^7$  Hz) causes decay in the Rabi oscillations at a rate  $\Gamma_\Omega$ . This type of noise feeds into the driven qubit via fluctuations in the detuning between drive frequency and the qubit precession frequency. The decay rate of the flip-flop qubit is given by  $\Gamma_\Omega = (\pi/2)(2\pi \sum_{i=x,y,z} \partial \epsilon_{\text{eff}} / \partial E_i)^2 S(\Omega_R)$ . At the low-error operation region of Fig. ??f,  $\partial \epsilon_{\text{eff}} / \partial E_z \sim 10^3$  Hz  $\text{V}^{-1} \text{ m}$  and  $\partial \epsilon_{\text{eff}} / \partial E_{x,y} \sim 10^2$  Hz  $\text{V}^{-1} \text{ m}$  (from Fig. 3.3g).  $1/\nu$  charge noise gives  $\Gamma_\Omega < 10^4$  Hz, implying  $< 10^{-4}$  errors. Johnson-Nyquist noise from room temperature gives  $\Gamma_\Omega = 3 \times 10^2$  Hz, whereas EWJN at 100 mK gives  $\Gamma_\Omega = 2 \times 10^1$  Hz, therefore producing  $< 10^{-5}$  and  $< 10^{-6}$  errors, respectively.

At the same time, horizontal noise will also have an effect, albeit minimal, in gate performance. For the parameters at which  $V_t \approx 10$  GHz in Fig. 2.10b,  $10 \mu\text{V}$  r.m.s. lateral noise would cause less than 0.01% uncertainty in the dipole size, therefore causing negligible gate errors. The same noise causes less than 1% uncertainty in  $\delta_{\text{so}}$  (and therefore in gate time), which translates into maximum  $10^{-4}$  errors due to gate time jitter, and maximum  $\sim 10^4$  Hz extra dephasing due to dispersive shifts (Eq. 2.29).

We conclude that quasi-static  $E_z$  noise and charge-phonon relaxation are the main sources of error and the most deleterious ones for flip-flop qubits. Therefore our analysis is sufficient to provide a reliable estimate of dephasing and gate errors. Indeed, low-frequency noise was

found to be the most deleterious one in a hybrid donor-dot qubit in a silicon MOS device **Harvey-Collard2015S**. Finally, note that we do not assume any type of dynamical noise correction or cancellation to be applied, and therefore our calculations are a worst-case scenario. Table 2.1 summarizes these results.

## 2.4 Two-qubit coupling

To couple two flip-flop qubits, we use the electric dipole that naturally arises when a donor-electron wavefunction is biased to the ionization point, due to the fact that a negative charge has been partly displaced away from the positive  $^{31}\text{P}$  nucleus. The electric field produced by this induced dipole in turn, modifies the energy of a nearby donor which is also biased at the ionization point, resulting in a long-range coupling between the two. This is illustrated in figure 2.16(a).

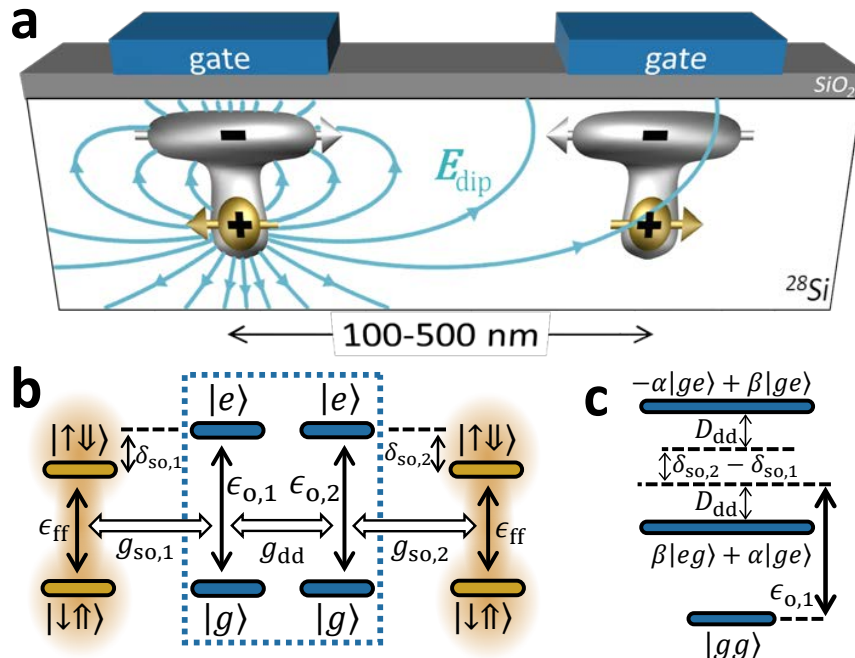


FIGURE 2.16: Electric dipole-dipole interactions between two distant flip-flop qubits. **a**, Device scheme for coupling qubits, showing dipole field lines,  $E_{\text{dip}}$ , produced by the dipole on the left. **b**, Level diagram for two-qubit coupling via electric dipole-dipole interaction. **c**, Lowest molecular eigenstates for the two charge qubits inside dashed rectangle in **b**.

The interaction energy between two distant dipoles,  $\mu_1$  and  $\mu_2$ , oriented perpendicularly to their separation  $r$  is  $V_{\text{dip}} = \mu_1\mu_2/(4\pi\epsilon_r\epsilon_0 r^3)$ , where  $\epsilon_0$  is the vacuum permittivity and  $\epsilon_r$  the material's dielectric constant ( $\epsilon_r = 11.7$  in silicon)[27]. The electric dipole of each donor-interface state is  $\mu_i = ed_i(1 + \sigma_{z,i})/2$ , implying that the dipole-dipole interaction Hamiltonian is:

$$\mathcal{H}_{\text{dip}} = V_{\text{dd}} (\sigma_{z,1}\sigma_{z,2} + \sigma_{z,1} + \sigma_{z,2}) \quad (2.51)$$

$$V_{\text{dd}} = \frac{1}{16\pi\epsilon_0\epsilon_r h} \frac{e^2 d_1 d_2}{r^3} \quad (2.52)$$

This electric dipole-dipole interaction is therefore equivalent to a small shift in the equilibrium orbital position of both electrons plus a coupling term between the charge qubits (blue dashed rectangle in Fig. 2.16b) equal to:

$$g_{dd} = \langle e_1 g_2 | H_{\text{dip,coupling}} | g_1 e_2 \rangle \quad (2.53)$$

$$= V_{dd} \langle e_1 | \sigma_{z,1} | g_1 \rangle \langle g_2 | \sigma_{z,2} | e_2 \rangle \quad (2.54)$$

$$= V_{dd} \frac{V_{t,1} V_{t,2}}{\epsilon_{o,1} \epsilon_{o,2}} \quad (2.55)$$

The strength of the dipole also depends on screening effects.

**Dipole Screening** Our device topology consists of a  $\text{SiO}_2$  layer sandwiched between a metal gate and silicon substrate, with the donor embedded in the substrate. In such a topology, the image charges of the donor electron and nucleus will be located above the donor, thereby creating an additional vertical dipole.

The magnitude and polarity of the image charges depend on the details of the nanos-structure, such as the donor depth and thickness of the oxide. We first analyze two extreme scenarios considering image charges at (i) silicon-metal and (ii) silicon-oxide interfaces. For a source donor electron (or nuclear) charge  $\mathcal{D}_{e(n)}$ , in silicon, the image charge  $\mathcal{I}_{e(n)}$  in the interface material is given by **Rahman2009S**

$$\mathcal{I}_{e(n)} = Q \mathcal{D}_{e(n)}, \quad (2.56)$$

$$Q = \frac{\epsilon_{\text{Si}} - \epsilon_{\text{I}}}{\epsilon_{\text{Si}} + \epsilon_{\text{I}}}, \quad (2.57)$$

where  $\epsilon_{\text{Si}} = 11.7$  is the dielectric constant of silicon,  $\epsilon_{\text{I}} = 3.9$  and  $\infty$  for oxide and metal interfaces respectively. Figures 2.17a,b show the magnitude and polarity of the image charges for both types of interfaces. For simplicity, we assume in Fig. 2.17 and Eq. 2.56 that the donor electron as well as its image are point charges. Given that the separation between the two donors is at least 180 nm (more than hundred times the Bohr radius of the donor electron), the above assumption is valid when calculating their dipolar interaction.

We first consider the electric dipole to be vertical. For the silicon-metal interface in Fig. 2.17a,  $Q = -1$  and therefore the image charges have the opposite sign and same magnitude as the source charges. As a result, the total electric field  $E_{\text{dip}}$  from each donor will be enhanced by a factor of 2. This improves the electric dipole coupling  $g_{dd}$  between the two donors by a factor of 4. On the contrary, for the silicon-oxide interface in Fig. 2.17b, the image charges have the same sign and reduced magnitude ( $Q = 0.5$ ) as the source charges, which decreases  $E_{\text{dip}}$  by half and therefore  $g_{dd}$  to a quarter of its bare value.

For a real device, which typically contains a few metal gates on top of a  $\sim 8$  nm thick  $\text{SiO}_2$ , it is difficult to make a precise estimate of the extra electric field from image charges. **Rahman et. al. Rahman2009S** assumed that a combination of metallic and oxide screening effects yields  $Q = -0.5$ , corresponding to an improvement in the magnitude of the electric dipole by  $\approx 50\%$ , which yields an improvement in  $g_{dd}$  by 125%. This means that, while building a real device, one would have to aim for slightly larger inter-donor separations than the ones presented here.

Since the donor-interface tunnel coupling  $V_t$  has to be tuned to a precise value, the dipole will also have lateral components as shown on the insets of Fig. 2.10. These components will also be affected by image charges. In the case of a metallic interface, Fig. 2.17a, the lateral image dipole has opposite direction as the original one, and therefore the total lateral component will be completely screened. On the other hand, for the  $\text{SiO}_2$  interface, Fig. 2.17b, the lateral component will be enhanced by 50%. Finally, for our assumed real structure ( $Q = -0.5$ ), the lateral dipole will decrease to half its original value.

In total, the dipole size and orientation, including screening, will be:

$$\mathbf{D}_i = \mathbf{d}_i + Q \times (d_{i,x}, d_{i,y}, -d_{i,z}), \quad (2.58)$$

where  $\mathbf{d}_i$  refers to the bare dipole, with  $x$ ,  $y$  and  $z$  components  $d_{i,x}$ ,  $d_{i,y}$  and  $d_{i,z}$ , respectively.

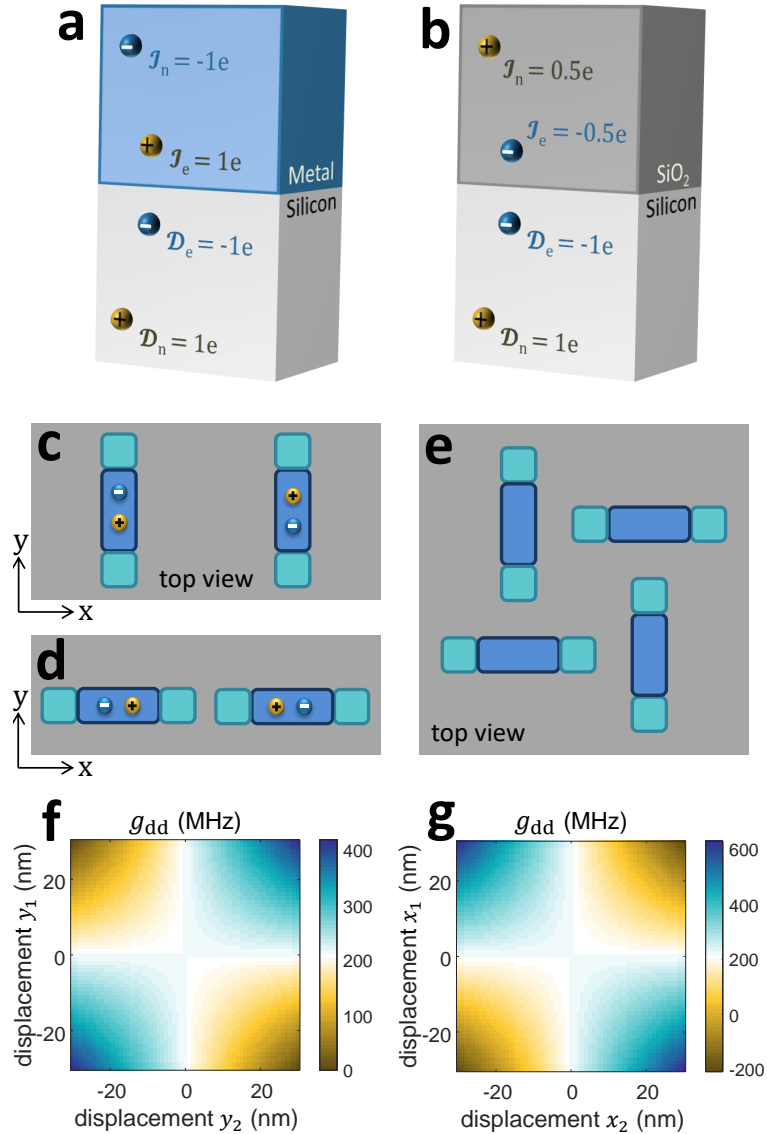


FIGURE 2.17: **Screening and image charges.** Image ( $\mathcal{I}_e$  and  $\mathcal{I}_n$ ) charges of the donor electron ( $\mathcal{D}_e$ ) and nucleus ( $\mathcal{D}_n$ ) for silicon-metal (a) and silicon-oxide (b) interfaces. The magnitude and polarity of the image charges are given by Supplementary Eq. 2.56. Schematic top view of two interacting dipoles when the negative charges (blue spheres) are displaced in perpendicular (c) and parallel (d) direction to the inter-dipole separation. e, Top view of gate stack that tunes each qubit's  $V_t$  by displacing their interface states perpendicularly to their nearest neighbor displacement, leaving  $g_{dd}$  unchanged. Inter-dipole coupling  $g_{dd}$ , as predicted by Eq. 2.59, for the orientation shown in c (f) and d (g), for  $r = 200$  nm,  $d_1 = d_2 = 10$  nm and  $Q = -0.5$ .

As the image charges decrease a lateral dipole, the uncertainty in the total electric dipole of a donor-interface state is minimal, even when displacing the interface wavefunction laterally to tune up  $V_t$ . At  $V_t \approx 10$  GHz, the total dipole size of Fig. 2.2 ( $d_z = 11$  nm) is  $(1 + 0.5)d_z = 16.5$  nm, while the one of Fig. 2.10 ( $d_z = 5$  nm,  $d_x = 25$  nm) is  $\sqrt{[(1 + 0.5)d_z]^2 + [(1 - 0.5)d_x]^2} = 14.6$  nm. This is important for qubit reproducibility over a large scale processor.

To include images charges and angular dependencies, the dipole-dipole interaction term, Eq. 2.52, has to be modified to **Ravets2014S**:

$$V_{dd} = \frac{e^2}{16\pi\epsilon_0\epsilon_r h} \frac{\mathbf{D}_1 \cdot \mathbf{D}_2 - 3(\mathbf{D}_1 \cdot \mathbf{r})(\mathbf{D}_2 \cdot \mathbf{r})/r^2}{r^3}, \quad (2.59)$$

We neglect the interaction of a dipole with its own charge since it does not produce inter-donor coupling.

Laterally displacing the interface charge is, in general, necessary for the purpose of tuning the donor-interface tunnel coupling  $V_t$ . This displacement, however, also alters the total electric dipole direction and can therefore affect the dipole-dipole coupling  $g_{dd}$  between neighbouring qubits. We first consider the case in which the displacements are perpendicular to the separation between dipoles, Fig. 2.17c. The  $g_{dd}$  dependence on  $y_1$  and  $y_2$  is plotted in Fig. 2.17f, for maximum displacements of 30 nm (enough to tune  $V_t$  by two orders of magnitude – see Fig 2.10g). It shows that, provided that the interface states are displaced along the same direction,  $g_{dd}$  only varies by a factor of two. For completeness, we also analyze the case in which the interface states are displaced in the same direction as the inter-donor separation (Fig. 2.17d). As can be seen in the plot in Fig. 2.17g,  $g_{dd}$  varies by a factor of three if the interface states are displaced in opposite directions. Finally, the variation in  $g_{dd}$  can be reduced even further by fabricating the gate stack in such a way that the charges in neighbouring qubits are displaced in perpendicular directions, as in Fig. 2.17e. In this way, from Eq. ??, the only dipole terms contributing to the coupling are the vertical ones, and therefore  $g_{dd}$  is unchanged (to first order) while tuning  $V_t$ .

**Two-qubit coupling** The electric dipole-dipole interaction provides a natural way to couple two distant flip-flop qubits since each flip-flop qubit is coupled to their electron position (Eq. 2.7). We compute the 2-qubit coupling strength between the singlet ground state and excited triplet state

$$|S\rangle = \frac{1}{\sqrt{2}} (|g_1 \uparrow_1 \downarrow_1, g_2 \downarrow_2 \uparrow_2\rangle - |g_1 \downarrow_1 \uparrow_1, g_2 \uparrow_2 \downarrow_1\rangle) \quad (2.60)$$

$$|T\rangle = \frac{1}{\sqrt{2}} (|g_1 \uparrow_1 \downarrow_1, g_2 \downarrow_2 \uparrow_2\rangle + |g_1 \downarrow_1 \uparrow_1, g_2 \uparrow_2 \downarrow_1\rangle) \quad (2.61)$$

as the corresponding eigenenergy difference with the Hamiltonian

$$H = H_{ff}^1 + H_{ff}^2 + H_{dip}. \quad (2.62)$$

Figure 2.18a shows the results at the ionization point  $E_z^{0,2q} = E_z^0 - 2g_{dd}h/(2eL_i)$  which is shifted by the presence of the second qubit.

The coupling rate exceeds 10 MHz around two narrow regions when the flip flop qubit is in resonance with a molecular state as the two charge qubits in Fig. 2.16b form hybridized molecular states, which are coupled to each flip-flop qubit as illustrated in figure 2.16c. The states of the hybridized molecular states are

$$\tilde{g} = \beta|eg\rangle + \alpha|ge\rangle \quad (2.63)$$

$$\tilde{e} = -\alpha|eg\rangle + \beta|ge\rangle \quad (2.64)$$

,similar to eq. (2.20), with the coefficients as in eq. (2.18) and (2.19). We have  $A = \delta_{so,2} - \delta_{so,1}$  and  $B = 2g_{dd}$ . Basically A describes the energy scale ( $\sigma_z$ ) and B drives the transitions ( $\sigma_x$ ). The coupling between the two charge qubits shifts the charge qubit eigenenergies.

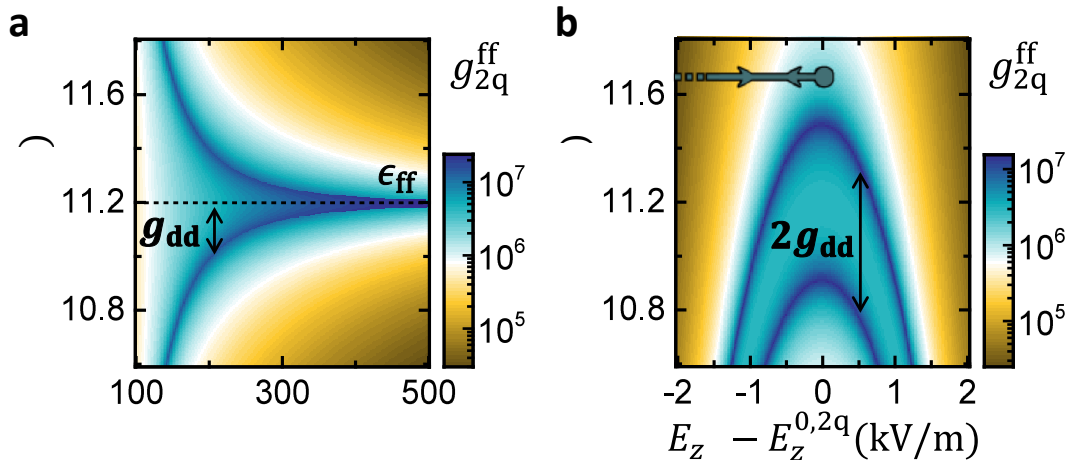


FIGURE 2.18: **Coupling rate between 2 flip-flop qubits.** **a**, Effective coupling between 2 flip-flop qubits as a function of  $V_{t,1} = V_{t,2} = V_t$ , interdistance  $r$  (**a**) and electric field  $E_{z,1} = E_{z,2} = E_z$  (**b**). The arrows in **b** represent the adiabatic path followed for 2-qubit gates.  $E_z^{0,2q}$  is the ionization point in the presence of a second qubit,  $E_z^{0,2q} = E_z^0 - 2g_{dd}h/(2eL_i)$ .

The resonant regime, however, induces too many relaxation errors due to resonant charge excitation. Therefore it is best to detune the flip-flop qubits from the molecular states, while still keeping a substantial inter-qubit coupling rate, via a second-order process. We calculate this coupling rate between the flip-flop qubits to

$$g_{2q}^{ff} = \langle \uparrow_1 \downarrow_1 \downarrow_2 \uparrow_2 | H_{tot} | \downarrow_1 \uparrow_1 \uparrow_2 \downarrow_2 \rangle \quad (2.65)$$

$$= g_{so,1} g_{so,2} \alpha \beta \left( \frac{1}{D_{dd} - \delta_{so,1}} + \frac{1}{D_{dd} + \delta_{so,2}} \right) \quad (2.66)$$

where

$$D_{dd} = \frac{|\langle g_1 e_2 | H_{orb}^A + H_{dip} | e_1 g_2 \rangle \langle e_1 g_2 | H_{orb}^A + H_{dip} | g_1 e_2 \rangle|}{E_{e_1 g_2} - E_{g_1 e_2}} \quad (2.67)$$

$$= (\delta_{so,2} - \delta_{so,1}) \left( 1 + [2g_{dd}/(\delta_{so,2} - \delta_{so,1})]^2 \right) / 2 \quad (2.68)$$

is the charge eigenenergy shift.

Figure 2.18b shows the coupling rate as a function of electric field at a fixed inter-qubit distance of  $r = 180$  nm.

**Two-qubit gates** 2-qubit gates start with both electrons at the interface, where qubits are decoupled since the electric dipoles and the hyperfine interactions are first-order insensitive to vertical electric fields. Indeed, from Eq. 2.65,  $g_{2q}^{ff}$  is negligible since  $g_{so}$  vanishes and  $\delta_{so}$  diverges. The electrons are then simultaneously and adiabatically displaced to the ionization point for a time necessary for an  $\sqrt{i}\text{SWAP}$  gate, before returning to the interface.

In Fig. 2.19a we show the dynamics of a 2-qubit gate performed with an adiabatic factor  $K = 30$ , following the trajectory shown in Fig. 2.18b. Similarly to 1-qubit  $z$  gates (the calculations are analogous to those in adiabatic phase control), the electron is first displaced in a fast time scale ( $\sim 0.3$  ns) set by the charge qubit parameters ( $\epsilon_0$  and  $V_t$ ), followed by a slower sweep ( $\sim 19$  ns) set by the spin-charge coupling parameters ( $\delta_{so}$  and  $g_{so}$ ), until it reaches the ionization point. The electron remains still for a short time before the whole process is then

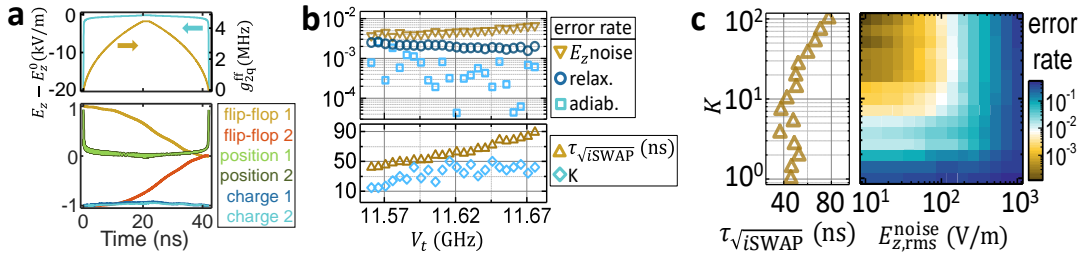


FIGURE 2.19: **High-fidelity adiabatic  $\sqrt{i\text{SWAP}}$  gates between two distant flip-flop qubits.** **a**, Time evolution of an adiabatic  $\sqrt{i\text{SWAP}}$  gate, for  $K = 30$ ,  $r = 180$  nm,  $B_0 = 0.4$  T and  $V_t = 11.58$  GHz. **b**, Optimized  $\sqrt{i\text{SWAP}}$  gate error, gate time and adiabatic factor  $K$ . **c**, Optimized error rate arising from quasi-static  $E_z$ -noise, for different noise amplitudes and adiabatic factor  $K$  (which sets the gate time).

reversed. In the end a  $\sqrt{i\text{SWAP}}$  gate is performed. While some amount of charge is excited during the process, it goes back to its ground state,  $|gg\rangle$ , with an adiabatic error around  $10^{-3}$ .

We quantify the 2-qubit gate fidelity in presence of the most deleterious noise types for our qubits, namely quasi-static  $E_z$  noise and charge-phonon relaxation. For this, we observe that the optimal gate fidelities are achieved when  $E_z(\tau_{\sqrt{i\text{SWAP}}}/2) \approx E_z^0$ . Similarly to 1-qubit  $x$ -gates, this happens because  $\sqrt{i\text{SWAP}}$  gates are sensitive to gate time jitter, and therefore errors are minimized at the CQSS where  $g_{2q}^{\text{ff}}$  is robust against  $E_z$  noise to first order – recall Fig. 2.18e and Eq. 2.65). An optimization algorithm finds the best adiabatic factor  $K$  that minimizes errors due to  $E_z$  noise for each value of  $V_{t,1} = V_{t,2} = V_t$ . The result is shown in Fig. 2.19b. Smaller detunings  $\delta_{\text{so}}$  (small  $V_t$ ) result in shorter gate times, which in turn reduces errors from quasi-static noise. However, this also implies a larger admixture of charge in the qubit eigenstates, which slightly increases relaxation errors. The lowest error rates,  $\sim 3 \times 10^{-3}$  are found at small detunings,  $V_t - \epsilon_{\text{ff}} - g_{\text{dd}} \approx 100$  MHz ( $V_t \approx 11.59$  GHz). At even smaller detunings, the 2-qubit coupling rate becomes too fast, requiring faster adiabatic sweeps to avoid over-rotation (lower  $K$ , Fig. 2.19b) and generating more leakage errors. The gate errors remain within  $10^{-3} - 10^{-2}$  for a wide range of  $V_t$ . Finally, we estimate in Fig. 2.19c how noise errors depend on the noise amplitude and adiabatic factor  $K$ , which sets the gate time.

Our proposed 2-qubit gates are not only well protected against noise, but also robust against donor misplacement. Variations in  $r$ ,  $d_1$  and  $d_2$  mainly cause variations in the charge qubits coupling  $g_{\text{dd}}$ , therefore simply changing the energy separation between molecular charge states (Fig. 2.18c). However, the coupling  $g_{2q}^{\text{ff}}$  between the flip-flop qubits can be kept essentially constant by simply readjusting  $V_t$ , using *e.g.* the method described in Fig. 3.3f,g. Figure 2.18d shows that one can keep a constant value of, for example,  $g_{2q}^{\text{ff}} = 1$  MHz for any inter-donor spacing between 180 and 500 nm, by adjusting  $V_t$  between 11.3 and 11.8 GHz. In other words, since the flip-flop qubit coupling is mediated by a tunable interaction with their respective charge qubits, the inter-qubit interaction does not need to decay with  $r^3$ , as one would otherwise get when the dipole interaction couples the qubits directly **Ogorman2014**, [28]. Therefore, two-qubit operations can be turned on between pairs of qubits separated by many sites in a 2-dimensional array. This tunable long-range connectivity can be exploited to great advantage in large-scale quantum processors **Li2017**. The large tolerance in  $g_{\text{dd}}$  also accommodates very well the donor depth uncertainties inherent to ion implantation **Donkelaar2015**, given the linear dependence of  $g_{2q}^{\text{ff}}$  on  $d_i$  (Eqs. 2.52 and 2.53).

We conclude that our scheme provides a dramatic reduction in the fabrication complexity, especially compared to schemes that require placing a gate between a pair of tightly-spaced donors, such as the Kane’s proposal [1], which requires  $r \approx 15$  nm separation between two  $^{31}\text{P}$  nuclear spins. Note that, by relocating the problem of valley oscillations from the exchange interaction [1] to the tunnel coupling, we have effectively provided a way in which the delicate parameter can now be tuned using a much simpler gate geometry.

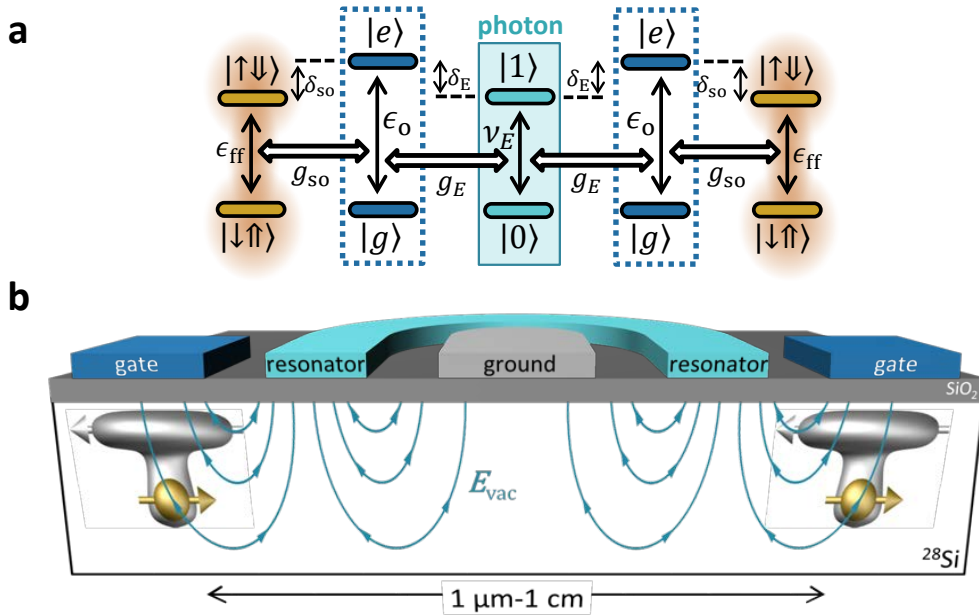


FIGURE 2.20: **Coupling to a resonator.** a, Level diagram for distant flip-flop qubit coupling via a microwave resonator showing photon number states and off-resonant charge states. b, Device scheme for coupling qubits via a photonic link. Distant donors, placed next to the resonator center line and biased to their ionization point, are subject to the vacuum electric field  $E_{vac}$  of a shared microwave resonator.

## 2.5 Scaling up using circuit quantum electrodynamics

In order to reach the long-term goal of a large-scale quantum processor, wiring up the control and read-out lines for each individual qubit is not trivial, given the high density in typical spin qubit architectures [29]. Recent solutions include cross-wiring using multilayer lithography [28] or floating gate electrodes inspired by dynamic random access memory systems **Veldhorst2016**. In both cases, using flip-flop qubits with long-distance interactions would result in widely spaced donors and loose fabrication tolerances. In addition, since flip-flop qubits are coupled via electric fields, they could be spaced further apart by using electrical mediators. These include floating metal gates **Trifunovic2012** or even microwave resonators. Indeed, the use of electric dipole transitions allows a natural integration of donor-based spin qubits into a circuit-Quantum Electrodynamics (QED) architecture **Xiang2013, Mi2016**, [12], [30] (see Fig. 4.1c for a possible device layout).

A full quantum mechanical treatment yields a charge-photon coupling rate given by Eq. 2.43, with  $\nu_E$  now representing the resonator fundamental mode frequency and  $E_{ac}$  the resonator vacuum field,  $E_{vac}$ . Again, it is best to have the charge excited state detuned from the flip-flop transition and resonator photon (see Fig. 4.1b), therefore minimizing charge excitation while retaining a second-order flip-flop-photon coupling given by Eq. 2.46. Assuming  $\delta_{so} \approx \delta_E \approx 10g_{so} \approx 10g_E$ , a  $d = 15$  nm deep <sup>31</sup>P flip-flop qubit would be coupled to photons at a  $g_E^{ff} \approx 3$  MHz rate. This is three orders of magnitude faster than the electron-spin coupling rate to a resonator via its magnetic vacuum field **Tosi2014**, [31], and comparable to the coupling strength obtained by using strong magnetic field gradients [32], [33], but without the need to integrate magnetic materials within a superconducting circuit. This assumes a vacuum field amplitude  $E_{vac} \approx 30$  V/m, which can be obtained by using tapered coplanar waveguide or high-inductance resonators [34].

The possibility of coupling the qubits to microwave photons provides a path for dispersive qubit readout, as well as for photonic interconnects. Near-quantum limited amplifiers have recently become available to obtain excellent readout speed and fidelities **Castellanos2008**. The resonator can also be used as a quantum bus to couple two spin qubits separated by as

z-gates		x(y)-gates			2-qubit $\sqrt{i\text{SWAP}}$ gates			Photonic link
$\tau_\pi$	Error	$\tau_{\pi/2}$	Power	Error	Distance	$\tau_{\sqrt{i\text{SWAP}}}$	Error	Coupling
70 ns	$10^{-4}$	30 ns	< 1 pW	$10^{-3}$	100 - 500 nm	40 ns	$10^{-2} - 10^{-3}$	$g_E^{\text{ff}} = 3 \text{ MHz}$

FIGURE 2.21: **Gate performance summary.** Figures of merit summarizing the speed and error rates of different gate schemes present in this chapter, assuming realistic noise sources.

far as 1 cm (Fig. 4.1c), a distance given by the mode wavelength. Fig. 4.1b shows the detailed energy level diagram. To avoid losses from photon decay, the qubits should be detuned from the resonator by an amount much greater than the qubit-photon coupling rates. Assuming  $\delta_E^{\text{ff}} = 10g_E^{\text{ff}}$ , where  $\delta_E^{\text{ff}} = \nu_E - \epsilon_{\text{ff}}$ , the effective 2-qubit coupling  $g_{2q}^{\text{ff}} \approx (g_E^{\text{ff}})^2 / \delta_E^{\text{ff}} \approx 0.3 \text{ MHz}$  yields a  $\sqrt{i\text{SWAP}}$  gate that takes only 0.4  $\mu\text{s}$ .



## Chapter 3

# The nuclear spin qubit with an electric dipole transition

---

*“Scalability is the future”*

---

-?

---

### 3.1 Introduction

The nuclear spin of a phosphorus donor in silicon has long been the subject of much study in the context of solid-state quantum information processing, either as a qubit cell for large-scale quantum processors **Ogorman2016**, [1], [28], or a memory for long-lived quantum information storage [35], [36]. Whether in ensemble form [37] or as individual qubit [4], the  $^{31}\text{P}$  nuclear spin has record-long coherence times, thanks to its insensitivity to electric fields and the possibility to drastically reduce magnetic environmental noise by hosting it in isotopically pure  $^{28}\text{Si}$  [38]. However, it cannot trivially be coupled to other quantum systems, and therefore all quantum computing proposals so far impose short interaction distances and slow quantum gate operations **Ogorman2016**, [1], [28].

In the hybrid approach to quantum information processing **Xiang2013**, different quantum systems interact in a large architecture that benefits from the best properties of each system, which are often coupled together via microwave resonators. In order to couple to individual spin qubits, the resonator vacuum field can be enhanced by shrinking its dimensions in the vicinity of the spin qubit, thereby enhancing the spin-photon coupling rate **Tosi2014**, **Sarabi2017**, [31], [39]. However, having a Zeeman splitting in the radio-frequency range and a null electric dipole, phosphorus nuclear-spins do not interact naturally with microwave resonators.

The artificial creation of electric dipole transitions has been proposed for different spin systems [40]–[44] as a way to facilitate scalability. The challenge here is how to make the spin drivable by electric fields without making it too susceptible to electrical noise, which can be significant in nanoscale electronic devices. In this chapter, we show how to engineer a strong electric dipole transition at microwave frequencies for the nuclear spin, based on the flip flop qubit and our finding from chapter 2, by applying an oscillating magnetic field to nucleus while the electron is shared between the donor and a quantum dot defined at the Si/SiO<sub>2</sub> interface **Calderon2006**, [19], [23], [44]. While the admixture of spin and charge states can potentially make the system very sensitive to electric noise, we show that the nuclear spin precession frequency and electric dipole strength can be rendered highly immune to electrical noise by a peculiar choice of spin-charge hybridization, same than for the flip flop qubit. By providing a robust coupling between the nuclear spin and electric fields, our scheme opens up new avenues to couple  $^{31}\text{P}$  qubits to other quantum systems, including microwave resonators, superconducting qubits, or simply other nuclear spins but at distances and with speeds that had not been anticipated so far.

### 3.2 Second-order Raman drive of a $^{31}\text{P}$ nuclear spin

The base of our proposal for the nuclear qubit is the flip flop qubit, as described in chapter 2, with the Hamiltonian  $H_{ff}$  from eq. (2.24).

The electron and nuclear spins can be coherently driven by conventional magnetic resonance transitions using oscillating magnetic fields at microwave [3] and radio frequencies [45]. In particular, the nuclear spin transition frequency when the electron spin is  $|\downarrow\rangle$  (i.e. the  $|\downarrow\uparrow\rangle \leftrightarrow |\downarrow\downarrow\rangle$  transition) is:

$$\epsilon_{\text{ns}}(A) = \gamma_n B_0 + A/2. \quad (3.1)$$

where  $\gamma_+ = \gamma_e + \gamma_n$ .

Now we show how the flip-flop transition provides a way of controlling the nuclear spin state without any radiofrequency field, by using instead two microwave-frequency excitations, one of which is electric, as illustrated in figure 3.1a. This has important advantages over magnetic-only schemes [35], [36], since it allows coupling a nucleus to the vacuum electric field of a microwave cavity, or to another nucleus similarly equipped with an electric dipole, as we will show below. The key idea is to combine the electrical drive of the flip-flop transition with an additional magnetic drive  $B_{\text{ac}} \cos(2\pi\nu_B t)$ , perpendicular to the static  $B_0$  (Fig 3.1a), where the Hamiltonian is

$$H_{\text{ESR}} = B_{\text{ac}} \cos(2\pi\nu_B t) (\gamma_e S_x - \gamma_n I_x) \quad (3.2)$$

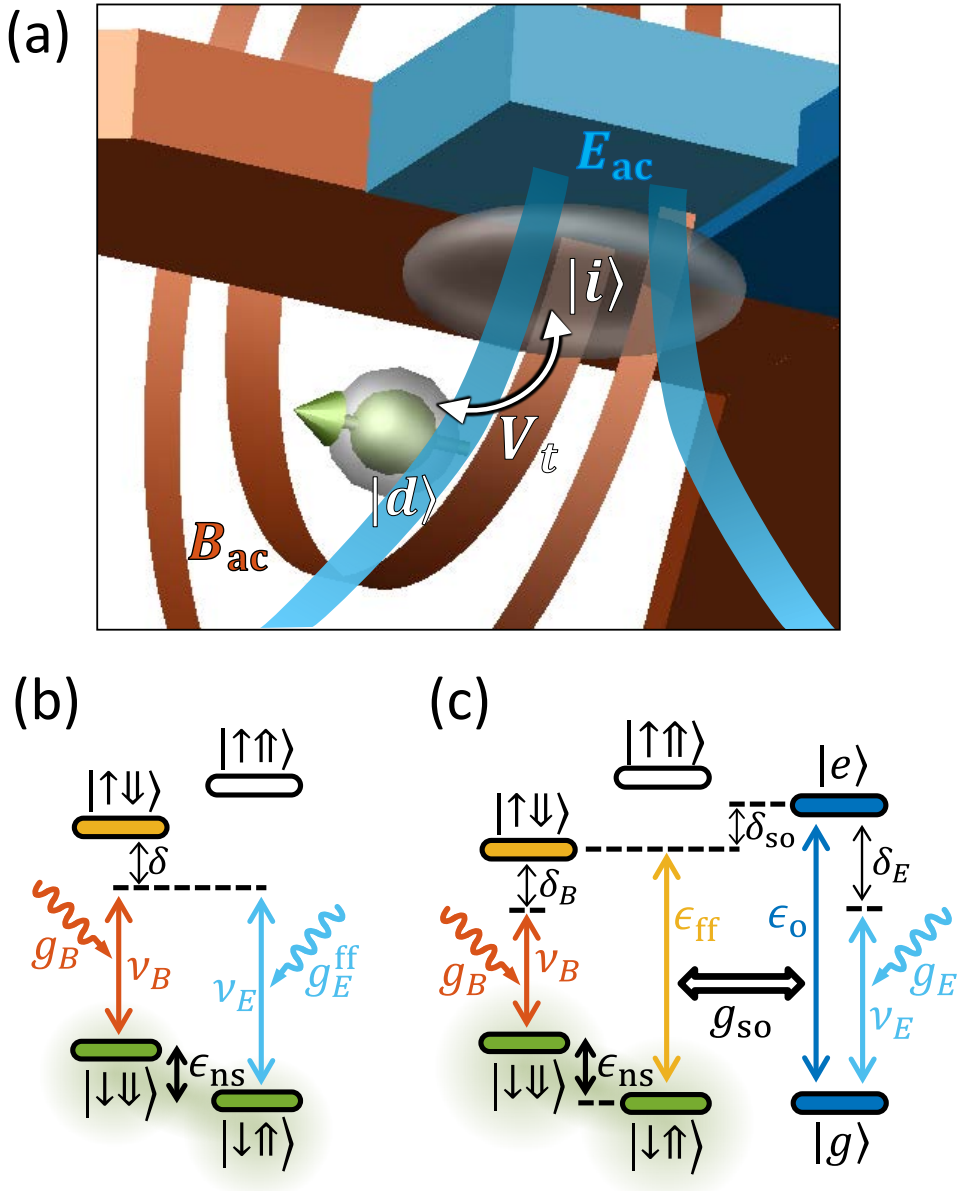


FIGURE 3.1: (a) Components of a Raman-enabled Si:P nuclear electric dipole transition. The electron spatial wavefunction (transparent gray) is shared between an interface-dot,  $|i\rangle$ , and a donor-bound state,  $|d\rangle$ , which are coupled by a tunnel rate  $V_t$ . Metallic gates (blue) on top of SiO<sub>2</sub> dielectric (not shown) control the electron charge state via a static vertical field  $E_{dc}$ , and can introduce an oscillating electric field  $E_{ac}$ . In a circuit-Quantum Electrodynamics setup, the electrostatic gate can be replaced by the inner conductor of a microwave resonator, and  $E_{ac}$  by the vacuum field of such resonator. A nearby broadband antenna Dehollain2013 (brown) provides the magnetic drive  $B_{ac}$ . (b) Simplified energy level diagram for Raman-drive of the Si:P nuclear-spin qubit, with energy splitting  $\epsilon_{ns}$ .  $| \uparrow \rangle$  ( $| \downarrow \rangle$ ) represents electron spin up (down), while  $| \uparrow \rangle$  ( $| \downarrow \rangle$ ) represents nuclear spin up (down). The second-order Raman drive is obtained by combining the microwave electric and magnetic drives, having frequencies  $\nu_B$  and  $\nu_E$ , respectively, and coupling rates  $g_B$  and  $g_E^{ff}$ , respectively. The drive is detuned by a frequency  $\delta$  from the  $| \uparrow \downarrow \rangle$  state. (c) Expanded energy diagram including the charge states  $|g\rangle$  and  $|e\rangle$ .

which gives the full nuclear qubit Hamiltonian

$$H_{ns} = H_{ff} + H_{ESR}. \quad (3.3)$$

This magnetic drive is the conventional electron spin resonance (ESR) transition, that couples the electron spin states  $|\downarrow\downarrow\rangle$  and  $|\uparrow\downarrow\rangle$  at a rate:

$$g_B = \langle \downarrow | H_{B_{ac}} | \uparrow \rangle = \gamma_e B_{ac} / 4. \quad (3.4)$$

Combining these two driving fields results in a process analogous to a Raman transition [Kok2010](#), as shown in Fig. 3.1b: with the electron in the ground spin state  $|\downarrow\rangle$ , the AC electric and magnetic fields drive the nuclear-spin “up”,  $|\downarrow\uparrow\rangle$ , and “down”,  $|\uparrow\downarrow\rangle$ , states, respectively, to a virtual level detuned from the  $|\uparrow\downarrow\rangle$  state by  $\delta \gg g_B, g_E^{\text{ff}}$ . As a result, the nuclear spin is driven via a second order process, with minimal excitation of the electron spin, at a rate:

$$g_E^{\text{ns}} = \frac{|\langle \downarrow\downarrow g | H_{ns} | \uparrow\downarrow g \rangle \langle \downarrow\downarrow g | H_{ns} | \uparrow\downarrow g \rangle|}{E_2 - E_1} \quad (3.5)$$

$$= \frac{g_B g_E^{\text{ff}}}{\delta}. \quad (3.6)$$

This can be interpreted as meaning that the microwave magnetic drive  $B_{ac}$  creates an electric dipole transition for the nuclear spin, with strength:

$$p_E^{\text{ns}} = \frac{4g_E^{\text{ns}}}{E_{ac}} = g_B \frac{A_{ac}}{E_{ac} \delta}. \quad (3.7)$$

At the ionization point, the hyperfine coupling  $A$  is strongly sensitive to electric fields, with  $\partial A = \partial E \approx 10^4 \text{ Hz}\cdot\text{m/V}$  for  $V_t$  of the order of 10 GHz [\[44\]](#). Here, directly applying Eq. 3.7 would yield a nuclear spin electric dipole  $p_E^{\text{ns}} \sim 0.2$  Debye. However, in this regime the quantum mechanical nature of the charge degree of freedom needs to be taken fully into account. Fig. 3.1c shows the level diagram for a nuclear spin Raman transition taking the electron charge levels into account. Operating in a detuned regime where  $\delta_{\text{so}} = \epsilon_0 - \epsilon_{\text{ff}} \gg g_{\text{so}}$ , in which case  $|e\rangle$  is minimally excited whereas  $A$  remain strongly sensitive to electric fields ( $E_{dc} \approx 0$ ), we know from chapter 2, that the flip-flop qubit and the AC electric field are coupled with strength  $g_E^{\text{ff}}$  (eq. (2.46)) which corresponds to a strong electric-dipole flip-flop transition ( $\sim 80$  Debye, assuming  $\delta_{\text{so}} = 10g_{\text{so}}$ ). Combining the strong flip-flop drive with the magnetic drive at rate  $g_B$  (Eq. 3.5) results in a strong electric dipole transition for the nuclear spin ( $\sim 8$  Debye, assuming  $\delta = 10g_B$ ). However, since the nuclear transition frequency depends linearly on  $A$  (see Eq. 3.1), and  $A$  is a very sensitive function of electric field near the donor ionization point, electrical noise in the device will cause fast dephasing of the nuclear precession.

### 3.3 Robust electric dipole transition of a Si:P nuclear spin

#### 3.3.1 Electron, nuclear and charge hybridization

We now show that, by adopting a different choice of device tuning, the nuclear spin can be made largely insensitive to electrical noise, while having its electric dipole transition increased even further. This is achieved by tuning the charge qubit in resonance with the flip-flop qubit ( $\epsilon_0 \approx \epsilon_{\text{ff}}$ , i.e.  $\delta_{\text{so}} \approx 0$ ), the magnetic drive in resonance with the electron spin ( $\delta_B = \gamma_e B_0 - \langle A \rangle / 2 - \nu_B \approx 0$ ), and the electric drive in resonance with the flip-flop (and charge) qubit ( $\delta_E \approx 0$ ). In this strongly hybridized regime, second-order perturbation theory can not be directly applied. We therefore analyze the nuclear spin Hamiltonian  $H_{ns}$  by first making it time-independent. Next we express  $\mathcal{H}_{ns}$  in the rotating frame of the magnetic drive by using the transformation:

$$\mathcal{H}' = U^\dagger \mathcal{H}_{ns} U - i\hbar U \dot{U}^\dagger, \quad (3.8a)$$

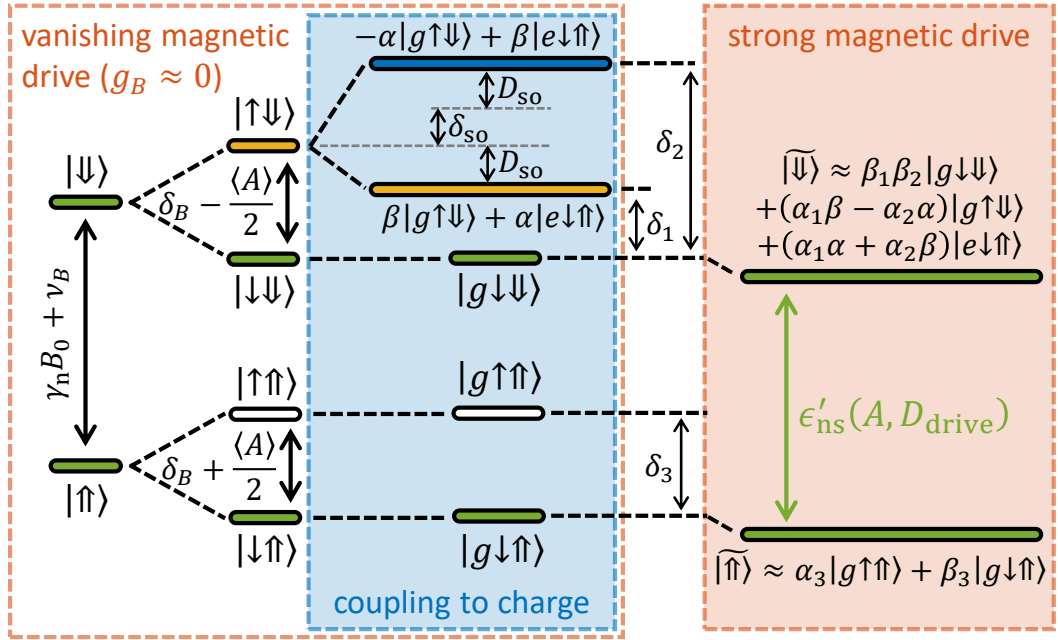


FIGURE 3.2: Nuclear spin levels in the rotating frame of the magnetic drive  $B_{ac}$  at frequency  $\nu_B$ . From left to right, the system eigenstates are shown while adding the electron spin state, then the charge state, then increasing the strength of the magnetic drive. See main text for a detailed description.

$$U = e^{i2\pi\nu_B t(S_z + I_z)}. \quad (3.8b)$$

We get

$$i\hbar U U^\dagger = \hbar\nu_B (S_z - I_z) \quad (3.9)$$

and with  $\cos(2\pi\nu_B t) = \frac{1}{2} (e^{i2\nu_B t} + e^{-i2\nu_B t})$

$$U H_{ESR} U^\dagger = \frac{B_{ac}}{2} \left[ \gamma_e \begin{pmatrix} 0 & e^{2 \cdot i2\pi\nu_B t} + 1 \\ e^{-2 \cdot i2\pi\nu_B t} + 1 & 0 \end{pmatrix} - \gamma_n \begin{pmatrix} 0 & e^{2 \cdot i2\pi\nu_B t} + 1 \\ e^{-2 \cdot i2\pi\nu_B t} + 1 & 0 \end{pmatrix} \right] \quad (3.10)$$

We neglect the counter-rotating terms, according to the rotating wave approximation and arrive at the transformed time-independent Hamiltonian of

$$\mathcal{H}' = (\gamma_e B_0 - \hbar\nu_B) S_z + (\gamma_n B_0 - \hbar\nu_B) I_z + H_{\text{orb}} + H_A^{\text{orb}} \quad (3.11)$$

After dropping counter-rotating terms, the transformed Hamiltonian becomes time-independent:

$$\begin{aligned} \mathcal{H}' = & \underbrace{(\gamma_e B_0 - \nu_B)}_{\delta_B} S_z - (\gamma_n B_0 + \nu_B) I_z \\ & + \frac{B_{ac}}{2} (\gamma_e S_x - \gamma_n I_x) + \mathcal{H}_{\text{orb}} + H_A^{\text{orb}}, \end{aligned} \quad (3.12)$$

The dominant energy scale in the above Hamiltonian is given by the term  $-(\gamma_n B_0 + \nu_B) I_z$ , which represents the energy splitting of the nuclear spin states, but shifted to microwave frequencies by the transformation to the rotating frame of  $\mathcal{H}_{\text{ESR}}$ . The corresponding energy levels are shown as  $|\uparrow\rangle$ ,  $|\downarrow\rangle$  at the left-most end of Fig. 3.2. These levels are further split by the electron spin Hamiltonian,  $(\delta_B + \langle A \rangle I_z) S_z + 2g_B S_x$ , where the expectation value of the hyperfine coupling  $\langle A \rangle$  depends on the electron charge state, yielding the electron-nuclear spin levels shown in Fig. 3.2, depicted in the limit of vanishing  $B_{ac}$  (and

therefore  $g_B$ ). In this case, the nuclear-spin transition frequency, in the rotating frame, with the electron in the ground state, is:

$$\epsilon'_{\text{ns}}(A) = \gamma_n B_0 + \nu_B + \langle A \rangle / 2. \quad (3.13)$$

In Fig. 3.3a we plot (dashed line)  $\epsilon'_{\text{ns}}(A)$  by including the dependence of  $\langle A \rangle$  on vertical electric field  $E_{\text{dc}}$  (from Eqs. 2.3,2.7). This is valid when the electron charge states are far detuned from the spin levels ( $\delta_{\text{so}} \gg g_{\text{so}}$ ). The plot highlights the strong dependence of  $\epsilon'_{\text{ns}}$  on electric fields under such conditions.

However, the nuclear spin dispersion changes dramatically when  $\delta_{\text{so}}$  approaches zero. In that case,  $\mathcal{H}_A^{\text{orb}}$  hybridizes the flip-flop and charge states, as shown in the blue panel within Fig. 3.2. The overall ground state is  $|g \downarrow\uparrow\rangle$ , but the excited flip-flop state splits into two hybridized states  $\beta|g \uparrow\downarrow\rangle + \alpha|e \downarrow\uparrow\rangle$  and  $-\alpha|g \uparrow\downarrow\rangle + \beta|e \downarrow\uparrow\rangle$ , with:

$$\alpha = \frac{\theta}{\sqrt{\theta^2 + 1}}, \quad \theta = \frac{\delta_{\text{so}} - \sqrt{\delta_{\text{so}}^2 + 4g_{\text{so}}^2}}{2g_{\text{so}}}, \quad (3.14a)$$

$$\beta = \frac{\phi}{\sqrt{\phi^2 + 1}}, \quad \phi = \frac{\delta_{\text{so}} + \sqrt{\delta_{\text{so}}^2 + 4g_{\text{so}}^2}}{2g_{\text{so}}}, \quad (3.14b)$$

so that  $\alpha = \beta = 1/\sqrt{2}$  for  $\delta_{\text{so}} = 0$  (eq. (2.26)).

As a final step, by increasing the magnetic drive amplitude  $B_{\text{ac}}$ , the Hamiltonian term  $2g_B S_x$  couples the electron spin  $|\uparrow\rangle$  and  $|\downarrow\rangle$  states, further hybridizing the system eigenstates  $|g \downarrow\downarrow\rangle$  with the hybridized flip flop states as well as  $|g \uparrow\uparrow\rangle$ . Two of those eigenstates, which we call  $|\widetilde{\downarrow\downarrow}\rangle$  and  $|\widetilde{\uparrow\uparrow}\rangle$  (Fig. 3.2, orange box), are chiefly composed of the tensor product of the nuclear  $|\downarrow\downarrow\rangle$ ,  $|\uparrow\uparrow\rangle$  states with the ground charge state  $|g\rangle$  and the ground  $|\downarrow\rangle$  electron spin state. They are obtained as:

$$|\widetilde{\downarrow\downarrow}\rangle \approx \beta_1 \beta_2 |g \downarrow\downarrow\rangle + (\alpha_1 \beta - \alpha_2 \alpha) |g \uparrow\downarrow\rangle + (\alpha_1 \alpha + \alpha_2 \beta) |e \downarrow\uparrow\rangle \quad (3.15)$$

$$|\widetilde{\uparrow\uparrow}\rangle \approx \alpha_3 |g \uparrow\uparrow\rangle + \beta_3 |g \downarrow\uparrow\rangle, \quad (3.16)$$

with coefficients  $\alpha_i, \beta_i$  ( $i = 1, 2, 3$ ) given by:

$$\alpha_1 = \frac{\theta_1}{\sqrt{\theta_1^2 + 1}}, \quad \theta_1 = \frac{\delta_1 - \sqrt{\delta_1^2 + (2\beta g_B)^2}}{2\beta g_B} \quad (3.17a)$$

$$\beta_1 = \frac{\phi_1}{\sqrt{\phi_1^2 + 1}}, \quad \phi_1 = \frac{\delta_1 + \sqrt{\delta_1^2 + (2\beta g_B)^2}}{2\beta g_B} \quad (3.17b)$$

$$\alpha_2 = \frac{\theta_2}{\sqrt{\theta_2^2 + 1}}, \quad \theta_2 = \frac{\delta_2 - \sqrt{\delta_2^2 + (2\alpha g_B)^2}}{2\alpha g_B} \quad (3.17c)$$

$$\beta_2 = \frac{\phi_2}{\sqrt{\phi_2^2 + 1}}, \quad \phi_2 = \frac{\delta_2 + \sqrt{\delta_2^2 + (2\alpha g_B)^2}}{2\alpha g_B} \quad (3.17d)$$

$$\alpha_3 = \frac{\theta_3}{\sqrt{\theta_3^2 + 1}}, \quad \theta_3 = \frac{\delta_3 - \sqrt{\delta_3^2 + 4g_B^2}}{2g_B} \quad (3.17e)$$

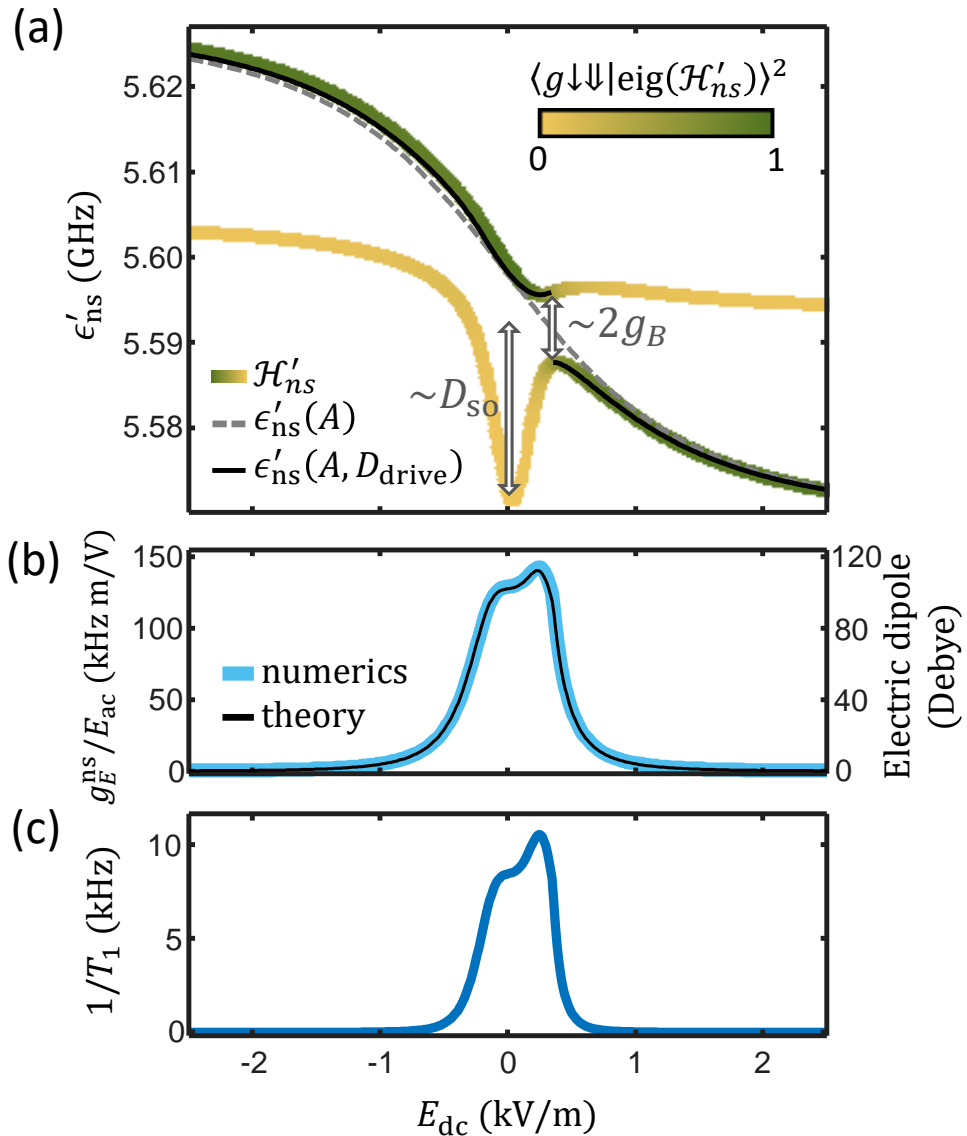


FIGURE 3.3: (a), Nuclear spin transition frequency  $\epsilon'_{ns}$  in the rotating frame of the magnetic drive  $B_{\text{ac}}$ , as a function of the static vertical electric field  $E_{dc}$  across the donor-dot system, for vanishing magnetic drive ( $\epsilon'_{ns}(A)$  – Eq. 3.13, grey dashed line) and strong magnetic drive ( $\epsilon'_{ns}(A, D_{\text{drive}})$  – Eq. 3.18, black solid line). We have assumed  $B_0 = 0.2$  T,  $B_{\text{ac}} = 0.6$  mT,  $d = 15$  nm and  $V_t \approx \epsilon_{\text{ff}}$  and  $\nu_B \approx \gamma_e B_0 - A/4$  (since  $\langle A \rangle = A/2$  at the ionization point). Green/yellow lines show transition frequencies calculated numerically from the Hamiltonian in Eq. 3.12. The color indicates the degree of admixture of the bare  $|g \downarrow \downarrow\rangle$  state into the higher  $\mathcal{H}'_{ns}$  eigenstate corresponding to each transition. The nuclear spin transition (predominantly  $|g \downarrow \uparrow\rangle \leftrightarrow |g \downarrow \downarrow\rangle$ ) anticrosses a flip-flop transition (predominantly  $|g \downarrow \uparrow\rangle \leftrightarrow |g \uparrow \downarrow\rangle$ ) at  $E_{dc} = 350$  V/m, with a splitting  $\sim 2g_B$  set by the strength of the magnetic drive. The flip-flop transition is strongly shifted by  $D_{\text{so}}$ , due to its coupling to the charge qubit states around  $E_{dc} = 0$ . At  $E_{dc} = 250$  V/m, the nuclear-spin excited eigenstate has  $\sim 75\%$  of  $|g \downarrow \downarrow\rangle$  and is robust against electrical noise ( $\partial \epsilon'_{ns} / \partial E_{dc} = 0$ ). (b), Nuclear electric dipole strength  $p_E^{\text{ns}} = \partial g_E^{\text{ns}} / \partial E_{\text{ac}}$  obtained from Eqs. 3.20 (theory, black line), or for numerical diagonalization of the full Hamiltonian  $\mathcal{H}'$  under  $E_{\text{ac}}$  drive (numerics, light blue line). For the choice of parameters used in this figure,  $p_E^{\text{ns}}$  peaks where  $E_{dc} = 250$  V/m. (c), Nuclear spin relaxation rate  $1/T_{1,\text{ns}}$  in the presence of the magnetic drive  $B_{\text{ac}}$  and the effect of coupling to phonons via charge states, Eq. 3.21.

$$\beta_3 = \frac{\phi_3}{\sqrt{\phi_3^2 + 1}}, \quad \phi_3 = \frac{\delta_3 + \sqrt{\delta_3^2 + 4g_B^2}}{2g_B} \quad (3.17f)$$

The energy splitting between  $|\widetilde{\downarrow\downarrow}\rangle$  and  $|\widetilde{\uparrow\uparrow}\rangle$ ,  $\epsilon'_{\text{ns}}$ , equals the bare nuclear-spin transition,  $\epsilon'_{\text{ns}}(A)$  (Eq. 3.13), plus an amount that depends on  $E_{\text{dc}}$ :

$$\epsilon'_{\text{ns}}(A, D_{\text{drive}}) = \epsilon'_{\text{ns}}(A) - D_{\text{drive}}(E_{\text{dc}}), \quad (3.18)$$

where  $D_{\text{drive}}$  is an AC-Stark shift given by second order perturbation theory to (analogues to eq. 2.29 and eq. 2.67):

$$D_{\text{drive}}(E_{\text{dc}}) = \sum_{i=1,2,3} \frac{\delta_i}{2} \left( \sqrt{1 + \left( \frac{2g_i}{\delta_i} \right)^2} - 1 \right), \quad (3.19a)$$

$$g_1 = \beta g_B, \quad g_2 = -\alpha g_B, \quad g_3 = g_B. \quad (3.19b)$$

This equation agrees with numerical simulations of the full Hamiltonian in the rotating frame of Eq. 3.12 (Fig. 3.3a). Around the ionization point, the flip-flop transition (itself strongly affected by the hybridization with the charge state) anticrosses the nuclear spin transition (in the rotating frame), creating a region where  $\partial\epsilon'_{\text{ns}}/\partial E_{\text{dc}} = 0$ , i.e. a first-order ‘clock transition’ [25], [46] where  $\epsilon'_{\text{ns}}$  is insensitive to electric noise to first order. Further adjustment of the parameters allows for  $\partial^2\epsilon'_{\text{ns}}/\partial E_{\text{dc}}^2 = 0$  (second-order clock transition), improving noise insensitivity even further.

In a key result of our proposal, the small admixture of the excited charge state,  $|e\rangle$ , into  $|\widetilde{\downarrow\downarrow}\rangle$  creates an electric-dipole transition for the nuclear spin. Indeed, the  $|\widetilde{\downarrow\downarrow}\rangle \leftrightarrow |\widetilde{\uparrow\uparrow}\rangle$  transition can be electrically-driven at a rate given by the charge admixture coefficients in Eq. 3.17 (see also Fig. 3.3b):

$$g_E^{\text{ns}} = g_E \beta_3 (\alpha_1 \alpha + \alpha_2 \beta), \quad (3.20)$$

This electric dipole transition, at microwave frequencies, can reach  $> 100$  Debye around  $E_{\text{dc}} = 0$  (Fig. 3.3c). This means that even an extremely weak AC electric field,  $E_{\text{ac}} \approx 3$  V/m, can drive a nuclear spin transition at a MHz Rabi frequency. This is two orders of magnitude faster than the typical Rabi frequencies obtained with standard (NMR) magnetic drive at radiofrequency [45], and an order of magnitude faster than obtained (at very high electric drive amplitudes) in a recent experiment where electrically-driven NMR was achieved by modulating the quantization axis of the electron spin [47].

### 3.3.2 Resilience against charge noise

The issue of charge noise is of paramount importance in semiconductor spin qubits. It is known, experimentally and theoretically, that charge fluctuators yield a  $1/\nu$  frequency dependence of the noise spectral density [14]. These models capture the averaged collective effect of many charge fluctuators on the qubit operation. In this case, charge noise results in a slow drift of the qubit electrostatic environment. Indeed, since individual qubit operations take less than a microsecond, the qubit environment is usually static within a single operations, but fluctuates in between operations. The estimating the noise in our system based on experimental results yields a  $1.7$  eV r.m.s. noise amplitude, which, given the distance between donor and interface  $d \approx 15$  nm, corresponds to an r.m.s. noise on the amplitude of the vertical electric field of order 100 V/m (see chapter 2.2). Inserting this into our model of the qubit energy yields a predicted nuclear spin dephasing rate of order 1 – 10 kHz. Note that, similarly to dressed states Laucht2017, [48], [49], the addition of the strong magnetic drive has the effect of extending the coherence of our qubit. However, here the suppressed noise is of electrical nature (despite the drive being magnetic), given the particular hybridization with charge states.

We thus derived the striking result that the nuclear spin has a strong electric dipole despite being robust against electrical noise. This is because, while the qubit precession frequency is insensitive to noise, its effective transverse matrix element is strongly dependent on electric fields. Importantly, the electric dipole is induced on the nuclear spin only around the flip-flop transition frequency, which is at several GHz. Since the charge and gate noise in nanoscale devices mainly has a  $1/\nu$  spectrum, the power spectral density of the noise at the frequency that would affect the nuclear qubit is expected to be very weak. Moreover, at the same bias point where the ‘clock transition’ ( $\partial\epsilon'_{\text{ns}}/\partial E_{\text{dc}} = 0$ ) for the nuclear energy takes place, the nuclear electric dipole itself is also first-order insensitive to electrical noise, since  $\partial g_E^{\text{ns}}/\partial E_{\text{dc}} = 0$  (Fig. 3.3b). A realistic  $1.5 \mu\text{eV}$  charge detuning noise **Freeman2016** would make  $g_E^{\text{ns}}$  fluctuate by only  $\sim 2\%$ . In other words, in this system both the free precession frequency and the Rabi frequency can be made first-order insensitive to charge noise.

As a final note, although we assumed  $\delta_{\text{so}} \rightarrow 0$ , the electric and magnetic driving fields are still off-resonance with the eigenstates of the full Hamiltonian  $\mathcal{H}_{\text{ns}}$  (hybridized charge-flip-flop states), ensuring minimal excitation of the  $|\uparrow\rangle$  and  $|e\rangle$  states.

### 3.3.3 Coupling to microwave cavity photons

This strong electric dipole at microwave frequencies provides a pathway for strongly coupling  $^{31}\text{P}$  nuclear spins to microwave resonators [12], where a vacuum field  $E_{\text{vac}}$  of a few V/m can result in vacuum Rabi splittings around 1 MHz. This could be achieved *e.g.* by connecting the top blue gate on Fig. 3.1a to the center pin of a superconducting coplanar waveguide resonator. Our proposal thus provides a solution to the fact that the standard (NMR) nuclear-spin transition does not naturally couple to microwave resonators. Similarly to other proposals [30], [50]–[52], here it is a classical drive ( $B_{\text{ac}}$ ) that enables coupling to a quantum field ( $E_{\text{vac}}$ ).

### 3.3.4 Nuclear spin relaxation

The engineered nuclear electric dipole also opens up a new pathway for nuclear spin relaxation:  $|\downarrow\downarrow\rangle$  can decay into  $|\uparrow\uparrow\rangle$  through a peculiar effect, where a photon from the driving field is combined with the nuclear spin energy (which is at radiofrequency) to emit a phonon at microwave frequency. The rate for this process can be roughly estimated as the admixture of the  $|e\rangle$  charge excited state into the  $|\downarrow\downarrow\rangle$  eigenstate times the charge relaxation rate  $1/T_{1,o}$ :

$$\frac{1}{T_{1,\text{ns}}} = \frac{|\langle \downarrow\downarrow | e \rangle|^2}{T_{1,o}} \approx \frac{|\alpha_1\alpha + \alpha_2\beta|^2}{T_{1,o}}, \quad (3.21)$$

where  $1/T_{1,o} = \Theta\epsilon_0 V_t^2$  (Ref. [20]), with  $\Theta \approx 2.37 \times 10^{-24} \text{ s}^2$  determined by the silicon crystal properties.

As Fig. 3.3c shows,  $1/T_{1,\text{ns}}$  peaks, around the ionization point, at a value that is still two orders of magnitude slower than *e.g.* the spin’s coupling rate to a microwave resonator, therefore allowing the strong coupling regime to be well within reach.

### 3.3.5 Dependence of electric dipole strength and spin relaxation rate on frequency and field detuning

In Fig. 3.3 we have shown an operation point ( $E_{\text{dc}} = 250 \text{ V/m}$  and  $\nu_B = 5.565 \text{ GHz}$ ) where the proposed nuclear spin electric dipole transition is robust against noise, *i.e.* both its precession frequency,  $\epsilon'_{\text{ns}}$ , and electric dipole strength,  $p_{\text{ns}}^E = g_E^{\text{ns}}/E_{\text{ac}}$ , are to first order insensitive to small perturbations of the static electric field. To understand how the system behaves when slightly detuned from the optimal working point, we calculated the dependence of the nuclear spin electric dipole strength  $p_{\text{ns}}^E$  and relaxation rate  $1/T_{1,\text{ns}}$  on the magnetic drive frequency,  $\nu_B$ , and on the static electric field,  $E_{\text{dc}}$ .

The results are plotted in Fig. 3.4. Both plots show two branches (bright yellow) where both dipole moment and relaxation rate are enhanced. To understand these branches, we refer to the level diagrams in Figs. 3.1b,c. First, note that  $\nu_B$  unequivocally sets the electric

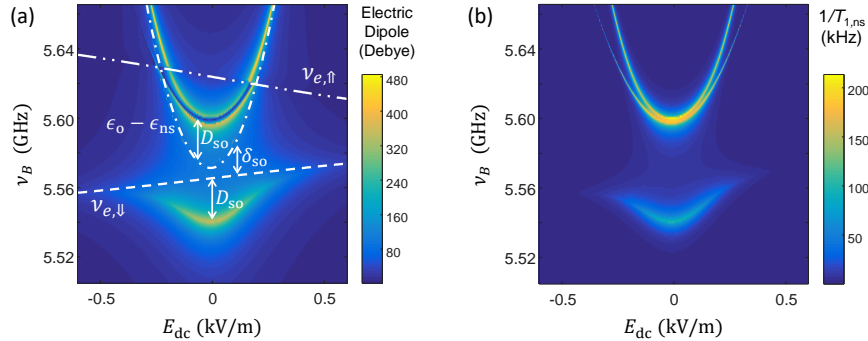


FIGURE 3.4: (a) Nuclear electric dipole strength  $p_E^{\text{ns}}$  and (b) nuclear spin relaxation rate  $1/T_{1,\text{ns}}$ , as a function of the donor-dot electric field detuning,  $E_{\text{dc}}$ , and the magnetic drive frequency,  $v_B$ .  $E_{\text{dc}} = 0$  is the ionization point, where the electron charge is equally shared between donor and interface dot. In (a), the dashed line shows the ESR frequency  $v_{e,\downarrow\downarrow}$  when the nuclear spin is in the  $|\downarrow\downarrow\rangle$  state, the dot-dashed line shows the charge qubit frequency minus the nuclear spin frequency,  $\epsilon_0 - \epsilon_{\text{ns}}$ , and the dot-dot-dashed line the electron spin resonance frequency  $v_{e,\uparrow\uparrow}$  when the nuclear spin is in the  $|\uparrow\uparrow\rangle$  state. The charge and flip-flop states are detuned by  $\delta_{\text{so}}$ , which is close to zero at  $E_{\text{dc}} = 0$ . Charge and flip-flop states then hybridize, shifting the system eigenenergies by an AC-Stark shift  $D_{\text{so}}$ . The plots in Figs. 3.3b,c correspond to specific line cuts of the graphs shown here, for  $v_B = v_{e,\downarrow\downarrow}$  at  $E_{\text{dc}} = 0$ , *i.e.*  $v_B = 5.565$  GHz.

dipole transition frequency  $\nu_E$  (in the simplest case,  $\nu_E = \nu_B + \epsilon_{\text{ns}}$ ). The two bright branches in Fig. 3.4a,b correspond to  $\nu_E$  being in resonance with either of the two charge-flip-flop hybridized states (yellow and blue states inside the light blue rectangle in Fig. 3.2). If the charge and flip-flop states were uncoupled or off-resonance, then the lower branch would simply correspond to the flip-flop dipole transition,  $\nu_E = \nu_{e,\downarrow\downarrow} + \epsilon_{\text{ns}}$  (where  $\nu_{e,\downarrow\downarrow}$  is the electron spin resonance frequency when the nuclear spin is in the ‘down’ state), which means that the magnetic drive frequency simply coincides with the electron spin resonance  $\nu_B = \nu_{e,\downarrow\downarrow}$ . This would represent a simple, on-resonance Raman transition, *i.e.* as in the sketch in Fig. 3.1b but where  $\delta = 0$ . Then, the upper branches in Fig. 3.4 would correspond to the pure charge transition,  $\nu_E = \epsilon_0$ , or equivalently  $\nu_B = \epsilon_0 - \epsilon_{\text{ns}}$ . However, since the charge and flip-flop states are coupled, they hybridize and further split the two branches by an amount equal to  $D_{\text{so}}$ .

Upon closer inspection, the upper branch shows an extra subtle feature. This branch corresponds to excitation conditions that put the magnetic drive frequency close to the electron spin resonance frequency when the nuclear spin is in the  $|\uparrow\uparrow\rangle$  state,  $\nu_{e,\uparrow\uparrow}$ . This, in turn, creates a pair of dressed electron spin states that further split the upper branch into two, separated by the ESR (magnetic) Rabi frequency of the  $\nu_{e,\uparrow\uparrow}$  resonance.

### 3.4 Long-distance coupling of nuclear spin qubits

We have shown in the previous section that a robust electric dipole at microwave frequencies is induced on the nuclear spin by the magnetic drive  $B_{\text{ac}}$ , combined with the spin-charge hybridization that is obtained by displacing the electron from the donor towards an interface quantum dot. A natural and important extension of this effect is to exploit the induced electric dipole to achieve a long-distance coupling of the nuclear spins, mediated by long-range electric dipole interaction, similar as for the flip flop qubit in chapter 2 (Fig. 3.5a) [44].

The dipole interaction between the charge qubits results in a coupling of  $g_d d$  (eq. (2.53)).

Two distant nuclear spin qubits can then be coupled when both electrons are around their ionization point, and an AC magnetic drive  $B_{\text{ac}}$  is applied (Fig. 3.5a,b) to each of them, resulting in the electric dipole  $p_E^{\text{ns}}$  at microwave frequencies. For the operation parameters used in Fig. 3.3,  $\epsilon_0 \approx \epsilon_{\text{ff}} \approx \nu_B + \epsilon_{\text{ns}}$  and  $g_B \ll g_{\text{so}}$ , the two-qubit coupling rate is obtained, via second-order perturbation theory, as:

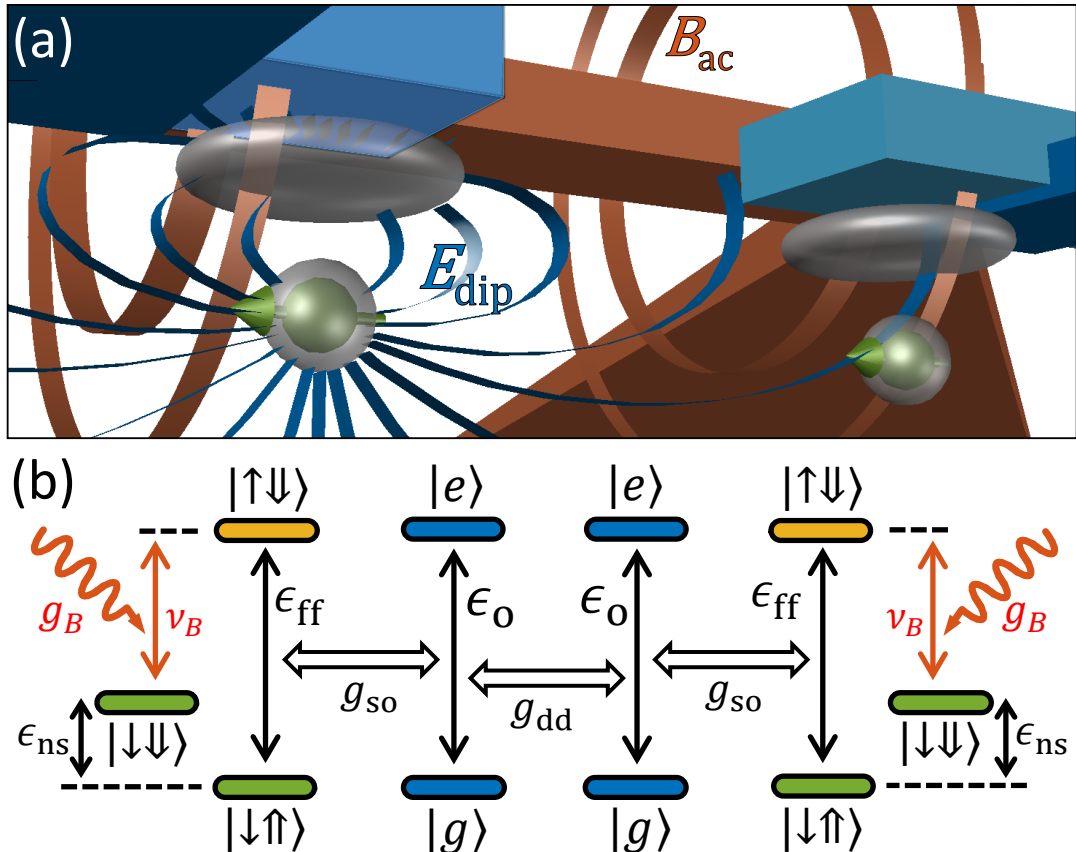


FIGURE 3.5: (a), Components and (b) level diagram for long-distance coupling of two  $^{31}\text{P}$  nuclear spins via electric dipole-dipole interactions. Each displaced electron produces an electric dipole field  $E_{\text{dip}}$  (shown only for one electron). The charge dipoles induced by displacing the electron wavefunction partly towards the interface dot interact with a strength  $g_{\text{dd}}$  (Eq. 2.53), and the charge qubits interact with the flip-flop states with strength  $g_{\text{so}}$  (Eq. 2.9). Adding the (global) magnetic drive of strength  $g_B$  and tuning the system to the fully-hybridized regime described in Sec. 3.3 results in a nuclear-nuclear coupling strength  $g_{2q}^{\text{ns}} \approx 0.55 \text{ MHz}$  at a 400 nm distance (Eq. 3.22).

$$g_{2q}^{ns} = \langle \tilde{\Psi}_1 \tilde{\Psi}_2 | H_{ns} | \tilde{\Psi}_1 \tilde{\Psi}_2 \rangle \quad (3.22)$$

$$= \left( \frac{g_B}{g_{so}} \right)^2 g_{dd}, \quad (3.23)$$

which is valid if  $g_B \ll (g_{so})^2/g_{dd}$ . For two nuclear spins  $r = 400$  nm apart,  $g_{2q}^{ns} = 0.55$  MHz, yielding a  $\sqrt{iSWAP}$  gate time of  $\sim 230$  ns. To put this in perspective, the Kane's proposal [1] described a system of two  $^{31}\text{P}$  nuclear spins placed  $r = 15$  nm apart, where a  $\sqrt{iSWAP}$  gate mediated by the electron spin exchange interaction requires  $3\ \mu\text{s}$  – an order magnitude slower, for over an order of magnitude tighter spacing. A recent proposal by Hill et al. describes a CNOT gate between nuclear spins mediated by the electron magnetic dipole interaction [28], wherein the 2-qubit gate time requires  $300\ \mu\text{s}$  for donors spaced 30 nm apart – three orders of magnitude slower than the electric-dipole mediated gate we have introduced here.

This method of coupling nuclear spin qubits at long distances via their induced electric dipole can be switched off completely –  $p_E^{ns} \approx 0$  when the electron charge is moved back to the donor – thus offering great flexibility in how multi-qubit operations are undertaken in a large array of qubits. The magnetic drive  $B_{ac}$  necessary to induce the dipole can be a global, always-on field, acting on every donor in the array. This can be optimally achieved by placing the device in a three-dimensional microwave cavity with good  $B_{ac}$  homogeneity [53]. Alternatively,  $B_{ac}$  could be delivered locally using a grid of microwave striplines [54]. The “robust” mode of operation described in Sec. 3.3 requires  $\delta_B \approx 0$ , i.e.  $B_{ac}$  in resonance with the electron spin transition. However, this resonance condition must be met while the donor is at the ionization point, where the hyperfine coupling is approximately half the value it has while the electron is fully at the donor ( $\langle A \rangle \approx A/2$ ), thus  $\nu_B \approx \gamma_e B_0 - A/4$ . Therefore, idle qubits with the electron resting at the donor will be left unaffected by the global magnetic drive, and completely decoupled from both electric and magnetic AC-fields.

### 3.5 Conclusion

The exceptional quantum coherence of  $^{31}\text{P}$  nuclear spins in isotopically enriched  $^{28}\text{Si}$  is experimentally well established [4], [37]. However, it has been widely accepted that using the  $^{31}\text{P}$  nuclear spin as the physical qubit in a quantum computer architecture requires dealing with the very small nuclear magnetic dipole, which renders operation and multi-qubit coupling slow and cumbersome **Ogorman2016**, [1], [28], even with inter-donor spacings  $\sim 10$  nm. Indeed, most of the recent focus on  $^{31}\text{P}$  nuclei for quantum information has been on using them as long-lived quantum memories [35], [36] rather than data qubits.

By engineering an electric dipole transition, we have shown here that the  $^{31}\text{P}$  qubit can also be driven at microwave frequencies, and coupled to other nuclei or to microwave cavities via electric dipole interactions, thus making it also a convenient system as data qubit. The effects of electrical noise can be strongly suppressed by operating around ‘clock transitions’, which allow the  $^{31}\text{P}$  system to retain dephasing times in the 0.1 – 1 ms range. The nuclear spin, equipped with an artificial electric dipole, can then be incorporated into large hybrid quantum architectures **Xiang2013** where – in analogy to flip-flop qubits [44] – large arrays of nuclear qubits couple either by electric dipole-dipole coupling or via cavity microwave photons. In such architectures, the spacing between qubits can be several hundreds of nanometers, leaving ample space for classical interconnects **Fischer2015**, [55] and readout devices, fabricated using conventional silicon nanoelectronics fabrication methods.

## Chapter 4

# Building a quantum processor

---

*"Scalability is the future"*

-?

---

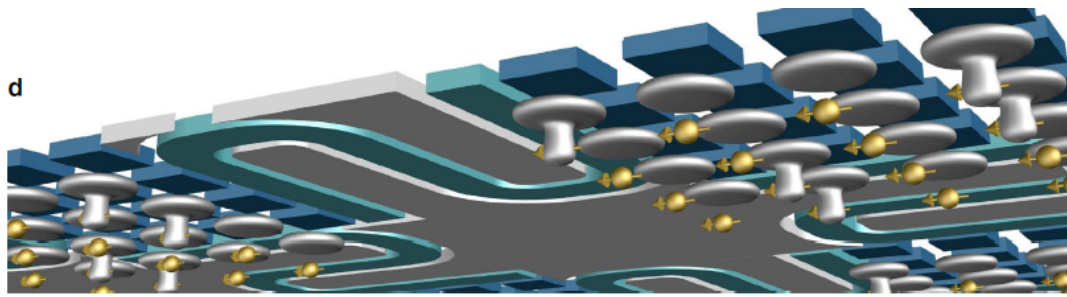


FIGURE 4.1: **Silicon hybrid quantum processor.** **a** Schematic view of a large-scale quantum processor based upon  $^{31}\text{P}$  donors in Si, operated and coupled through the use of an induced electric dipole. Idle qubits have electrons at the interface, leaving the  $^{31}\text{P}$  nucleus in the ultra-coherent ionized state. Electrons are partially shifted towards the donor for quantum operations. The sketch shows a possible architecture where a cluster of qubits is locally coupled via the electric dipole, and a subgroup thereof is further coupled to another cluster through interaction with a shared microwave cavity (aqua). The drawing is not to scale; control lines and readout devices are not shown.

Fig. 4.1a summarizes the key figures of merit of a quantum processor based on flip-flop qubits coupled by electric dipole interactions. Fast 1-qubit  $x$ -gates are attainable with low electric drive power and error rates  $\sim 10^{-3}$ . 2-qubit  $\sqrt{i\text{SWAP}}$  gates are fast and with error rates approaching  $10^{-3}$ . At the end of all operations, the phase of each qubit can be corrected, via adiabatic  $z$ -gates, in fast time scales and low error rates  $\sim 10^{-4}$ . These values are based on current experimentally known values of charge noise in silicon devices **Freeman2016**, and are possibly amenable to improvement through better control of the fabrication parameters. More advanced control pulse schemes could allow for faster gates with less leakage **Ghosh2016**, [56], [57], and active noise cancellation techniques, *e.g.* pulses for gate time jitter [58] or decoherence **Sar2012** suppression, could further improve gate fidelities.

Idle qubits are best decoupled from all other qubits by having the electron at the interface and the quantum state stored in the nuclear spin, which has a record coherence times  $T_2 \gtrsim 30$  s (ref. [4]), and can be even longer in bulk samples [37]. Quantum information can be swapped between the nuclear and the flip-flop qubit by simply applying an ESR  $\pi$ -pulse that excites the  $|\downarrow\downarrow\rangle$  state to  $|\uparrow\downarrow\rangle$  (Fig. ??c).

Qubit read-out can be obtained by spin-dependent tunneling into a cold charge reservoir, detected by a single-electron transistor [2]. Read-out times can be  $\sim 1\ \mu\text{s}$  with cryogenic amplifiers [59], which is comparable to the time necessary to perform, for example,  $\sim 20$  individual gates lasting  $\sim 50$  ns each, in a surface code error correction protocol [60].

A large-scale, fault-tolerant architecture can be built in a variety of ways. One- or two-dimensional arrays can be built to implement error correction schemes such as the Steane [61] or the surface [60] code, since all mutual qubit couplings are tunable and gateable. A larger processor can include a hybrid of both coupling methods, incorporating cells of dipolarly-coupled qubits, interconnected by microwave photonic links (Fig. 4.1d), in which case more advanced error-correction codes can be implemented **Li2017**, [62]–[64]. Microwave resonators could be also used to interface donors with superconducting qubits **Devoret2013**, [65], for the long-term goal of a hybrid quantum processor that benefits from the many advantages of each individual architecture **Xiang2013**.

## Chapter 5

# Device fabrication and experimental methods

---

*“Scalability is the future”*

-?

---

**5.1 Device fabrication and packaging****5.2 Experimental setup**

## Chapter 6

# Low magnetic field effects in Si:P qubits

---

*"Improving and understanding the performance of our qubit"*

-?

---

Spin qubits have been advancing

## **6.1 Co-tunneling**

## **6.2 Evanescence-wave Johnson noise**

## Chapter 7

# Flip flop measurements

---

*"hopefully sth here..."*

-?

---



## Chapter 8

# Conclusion

---

*"wohooo..."*

*-?*

---



# Bibliography

- [1] B. E. Kane, "A silicon-based nuclear spin quantum computer", *Nature*, vol. 393, no. 6681, pp. 133–137, 1998, ISSN: 0028-0836. DOI: [10.1038/30156](https://doi.org/10.1038/30156). [Online]. Available: <http://www.nature.com/doifinder/10.1038/30156>5Cnpapers2://publication/doi/10.1038/30156.
- [2] A. Morello, J. J. Pla, F. A. Zwanenburg, K. W. Chan, K. Y. Tan, H. Huebl, M. Möttönen, C. D. Nugroho, C. Yang, J. A. Van Donkelaar, A. D. Alves, D. N. Jamieson, C. C. Escott, L. C. Hollenberg, R. G. Clark, and A. S. Dzurak, "Single-shot readout of an electron spin in silicon", *Nature*, vol. 467, no. 7316, pp. 687–691, 2010, ISSN: 00280836. DOI: [10.1038/nature09392](https://doi.org/10.1038/nature09392). arXiv: [1003.2679](https://arxiv.org/abs/1003.2679).
- [3] J. J. Pla, K. Y. Tan, J. P. Dehollain, W. H. Lim, J. J. L. Morton, D. N. Jamieson, A. S. Dzurak, and A. Morello, "A single-atom electron spin qubit in silicon", *Nature*, vol. 489, no. 7417, pp. 541–544, 2012, ISSN: 00280836. DOI: [10.1038/nature11449](https://doi.org/10.1038/nature11449). arXiv: [1305.4481](https://arxiv.org/abs/1305.4481). [Online]. Available: <http://dx.doi.org/10.1038/nature11449>.
- [4] J. T. Muhonen, J. P. Dehollain, A. Laucht, F. E. Hudson, R. Kalra, T. Sekiguchi, K. M. Itoh, D. N. Jamieson, J. C. McCallum, A. S. Dzurak, and A. Morello, "Storing quantum information for 30 seconds in a nanoelectronic device", *Nature Nanotechnology*, vol. 9, no. 12, pp. 986–991, 2014, ISSN: 17483395. DOI: [10.1038/nnano.2014.211](https://doi.org/10.1038/nnano.2014.211). arXiv: [1402.7140](https://arxiv.org/abs/1402.7140).
- [5] R. Rahman, G. P. Lansbergen, S. H. Park, J. Verdijin, G. Klimeck, S. Rogge, and L. C. L. Hollenberg, "Orbital Stark effect and quantum confinement transition of donors in silicon", pp. 1–10, 2009. DOI: [10.1103/PhysRevB.80.165314](https://doi.org/10.1103/PhysRevB.80.165314).
- [6] M. J. Calderon, A. Saraiva, B. Koiller, and S. D. Sarma, "Quantum control and manipulation of donor electrons in Si-based quantum computing", vol. 122410, no. 2009, 2009. DOI: [10.1063/1.3124084](https://doi.org/10.1063/1.3124084).
- [7] G. Klimeck, S. Member, S. S. Ahmed, H. Bae, N. Kharche, R. Rahman, S. Clark, B. Haley, S. Lee, M. Naumov, H. Ryu, F. Saied, M. Prada, M. Korkusinski, T. B. Boykin, and S. Member, "Atomistic Simulation of Realistically Sized Nanodevices Using NEMO 3-D — Part I : Models and Benchmarks", vol. 54, no. 9, pp. 2079–2089, 2007.
- [8] G. Klimeck, S. Member, S. S. Ahmed, N. Kharche, M. Korkusinski, M. Usman, M. Prada, T. B. Boykin, and S. Member, "Atomistic Simulation of Realistically Sized Nanodevices Using NEMO 3-D — Part II : Applications", vol. 54, no. 9, pp. 2090–2099, 2007.
- [9] Feher, "2i+1", *Physical Review*, vol. 834, no. 1956, 1959.
- [10] S. J. Hile, L. Fricke, M. G. House, E. Peretz, C. Y. Chen, Y. Wang, M. Broome, S. K. Gorman, J. G. Keizer, R. Rahman, and M. Y. Simmons, "Addressable electron spin resonance using donors and donor molecules in silicon", no. July, pp. 1–8, 2018.
- [11] J. L. Ivey and R. L. Mieher, "No Title", 1975.

- [12] A. Blais, R. S. Huang, A. Wallraff, S. M. Girvin, and R. J. Schoelkopf, "Cavity quantum electrodynamics for superconducting electrical circuits: An architecture for quantum computation", *Physical Review A - Atomic, Molecular, and Optical Physics*, vol. 69, no. 6, pp. 062320-1, 2004, ISSN: 10502947. DOI: [10.1103/PhysRevA.69.062320](https://doi.org/10.1103/PhysRevA.69.062320). arXiv: [0402216](https://arxiv.org/abs/0402216) [cond-mat].
- [13] B. C. Johnson, J. C. Mccallum, L. H.W. V. Beveren, and E Gauja, "Deep level transient spectroscopy study for the development of ion-implanted silicon field-effect transistors for spin-dependent transport", *Thin Solid Films*, vol. 518, no. 9, pp. 2524–2527, 2010, ISSN: 0040-6090. DOI: [10.1016/j.tsf.2009.09.152](https://doi.org/10.1016/j.tsf.2009.09.152). [Online]. Available: <https://dx.doi.org/10.1016/j.tsf.2009.09.152>.
- [14] E Paladino, "1 = f noise : Implications for solid-state quantum information", vol. 86, no. June, 2014. DOI: [10.1103/RevModPhys.86.361](https://doi.org/10.1103/RevModPhys.86.361).
- [15] D. Kim, D. R. Ward, C. B. Simmons, J. K. Gamble, R. Blume-kohout, E. Nielsen, D. E. Savage, M. G. Lagally, M. Friesen, S. N. Coppersmith, and M. A. Eriksson, "Microwave-driven coherent operation of a semiconductor quantum dot charge qubit", *Nature Nanotechnology*, vol. 10, no. 3, pp. 243–247, 2015, ISSN: 1748-3387. DOI: [10.1038/nnano.2014.336](https://doi.org/10.1038/nnano.2014.336). [Online]. Available: [http://dx.doi.org/10.1038/nnano.2014.336](https://dx.doi.org/10.1038/nnano.2014.336).
- [16] B. Thorgrimsson, D. Kim, Y.-c. Yang, L. W. Smith, C. B. Simmons, D. R. Ward, R. H. Foote, J Corrigan, D. E. Savage, M. G. Lagally, M. Friesen, S. N. Coppersmith, and M. A. Eriksson, "Extending the coherence of a quantum dot hybrid qubit", *npj Quantum Information*, no. March, pp. 2–5, 2017, ISSN: 2056-6387. DOI: [10.1038/s41534-017-0034-2](https://doi.org/10.1038/s41534-017-0034-2). [Online]. Available: [http://dx.doi.org/10.1038/s41534-017-0034-2](https://dx.doi.org/10.1038/s41534-017-0034-2).
- [17] B. M. Freeman, J. S. Schoenfield, H. Jiang, B. M. Freeman, J. S. Schoenfield, and H. Jiang, "quantum dots Comparison of low frequency charge noise in identically patterned Si / SiO<sub>2</sub> and Si / SiGe quantum dots", vol. 253108, no. 2016, 2017. DOI: [10.1063/1.4954700](https://doi.org/10.1063/1.4954700).
- [18] O. E. Dial, M. D. Shulman, S. P. Harvey, H Bluhm, V Umansky, and A Yacoby, "Charge Noise Spectroscopy Using Coherent Exchange Oscillations in a Singlet-Triplet Qubit", *Physical Review Letters*, vol. 110, no. 14, p. 146804, 2013, ISSN: 0031-9007. DOI: [10.1103/PhysRevLett.110.146804](https://doi.org/10.1103/PhysRevLett.110.146804). [Online]. Available: [http://link.aps.org/doi/10.1103/PhysRevLett.110.146804](https://link.aps.org/doi/10.1103/PhysRevLett.110.146804).
- [19] P. Harvey-Collard, N. T. Jacobson, M. Rudolph, J. Dominguez, G. A. Ten Eyck, J. R. Wendt, T. Pluym, J. K. Gamble, M. P. Lilly, M. Pioro-Ladrière, and M. S. Carroll, "Coherent coupling between a quantum dot and a donor in silicon", *Nature Communications*, vol. 8, no. 1, pp. 1–6, 2017, ISSN: 20411723. DOI: [10.1038/s41467-017-01113-2](https://doi.org/10.1038/s41467-017-01113-2). arXiv: [1512.01606](https://arxiv.org/abs/1512.01606). [Online]. Available: [http://dx.doi.org/10.1038/s41467-017-01113-2](https://dx.doi.org/10.1038/s41467-017-01113-2).
- [20] P. Boross, G. Széchenyi, and A. Pályi, "Valley-enhanced fast relaxation of gate-controlled donor qubits in silicon", 2016. arXiv: [arXiv:1509.08538v1](https://arxiv.org/abs/1509.08538v1).
- [21] B. Koiller, X. Hu, S. Das Sarma, and B. Koiller, "Exchange in Silicon-Based Quantum Computer Architecture", *Physical Review Letters*, vol. 88, no. 2, p. 4, 2002, ISSN: 10797114. DOI: [10.1103/PhysRevLett.88.027903](https://doi.org/10.1103/PhysRevLett.88.027903). arXiv: [0106259](https://arxiv.org/abs/0106259) [cond-mat].

- [22] J. Van Donkelaar, C. Yang, A. D. Alves, J. C. McCallum, C. Hougaard, B. C. Johnson, F. E. Hudson, A. S. Dzurak, A. Morello, D. Spemann, and D. N. Jamieson, "Single atom devices by ion implantation", *Journal of Physics Condensed Matter*, vol. 27, no. 15, 2015, ISSN: 1361648X. DOI: [10.1088/0953-8984/27/15/154204](https://doi.org/10.1088/0953-8984/27/15/154204).
- [23] M Veldhorst, J. C. C. Hwang, C. H. Yang, A. W. Leenstra, B. D. Ronde, and J. P. Dehollain, "An addressable quantum dot qubit with fault-tolerant control- fidelity", *Nature Nanotechnology*, vol. 9, no. 12, pp. 981–985, 2014, ISSN: 1748-3387. DOI: [10.1038/nnano.2014.216](https://doi.org/10.1038/nnano.2014.216). [Online]. Available: <http://dx.doi.org/10.1038/nnano.2014.216>.
- [24] M. Garwood and L. DelaBarre, "The return of the frequency sweep: Designing adiabatic pulses for contemporary NMR", *Journal of Magnetic Resonance*, vol. 153, no. 2, pp. 155–177, 2001, ISSN: 10907807. DOI: [10.1006/jmre.2001.2340](https://doi.org/10.1006/jmre.2001.2340).
- [25] G. Wolfowicz, A. M. Tyryshkin, R. E. George, H. Riemann, N. V. Abrosimov, P. Becker, H.-j. Pohl, M. L. W. Thewalt, S. A. Lyon, and J. J. L. Morton, "Atomic clock transitions in silicon-based spin qubits", *Nature Nanotechnology*, vol. 8, no. 8, pp. 561–564, 2013, ISSN: 1748-3387. DOI: [10.1038/nnano.2013.117](https://doi.org/10.1038/nnano.2013.117). [Online]. Available: <http://dx.doi.org/10.1038/nnano.2013.117>.
- [26] S. Oh, Y. P. Shim, J. Fei, M. Friesen, and X. Hu, "Resonant adiabatic passage with three qubits", *Physical Review A - Atomic, Molecular, and Optical Physics*, vol. 87, no. 2, pp. 1–6, 2013, ISSN: 10502947. DOI: [10.1103/PhysRevA.87.022332](https://doi.org/10.1103/PhysRevA.87.022332). arXiv: [arXiv:1201.4829v1](https://arxiv.org/abs/1201.4829v1).
- [27] S. Ravets, H. Labuhn, D. Barredo, L. Béguin, T. Lahaye, and A. Browaeys, "Coherent dipole – dipole coupling between two single Rydberg atoms at an electrically-tuned Förster resonance", vol. 10, no. December, 2014. DOI: [10.1038/NPHYS3119](https://doi.org/10.1038/NPHYS3119).
- [28] C. D. Hill, E. Peretz, S. J. Hile, M. G. House, M. Fuechsle, S. Rogge, M. Y. Simmons, and L. C. L. Hollenberg, "A surface code quantum computer in silicon", no. October, pp. 1–12, 2015.
- [29] L. M. K. Vandersypen, H. Bluhm, J. S. Clarke, A. S. Dzurak, R. Ishihara, A. Morello, D. J. Reilly, L. R. Schreiber, and M. Veldhorst, "Interfacing spin qubits in quantum dots and donors - hot, dense and coherent", *npj Quantum Information*, no. August, pp. 1–10, 2016, ISSN: 2056-6387. DOI: [10.1038/s41534-017-0038-y](https://doi.org/10.1038/s41534-017-0038-y). arXiv: [1612.05936](https://arxiv.org/abs/1612.05936). [Online]. Available: <http://arxiv.org/abs/1612.05936>.
- [30] L Childress and M. D. Lukin, "D", vol. 042302, pp. 1–8, 2004. DOI: [10.1103/PhysRevA.69.042302](https://doi.org/10.1103/PhysRevA.69.042302).
- [31] P Haikka, Y Kubo, A Bienfait, P Bertet, and K Mølmer, "Proposal for detecting a single electron spin in a microwave resonator IMPLEMENTATION g", vol. 022306, pp. 1–10, 2017. DOI: [10.1103/PhysRevA.95.022306](https://doi.org/10.1103/PhysRevA.95.022306).
- [32] X. Hu, Y. X. Liu, and F. Nori, "Strong coupling of a spin qubit to a superconducting stripline cavity", *Physical Review B - Condensed Matter and Materials Physics*, vol. 86, no. 3, pp. 1–5, 2012, ISSN: 10980121. DOI: [10.1103/PhysRevB.86.035314](https://doi.org/10.1103/PhysRevB.86.035314). arXiv: [1204.4732](https://arxiv.org/abs/1204.4732).

- [33] J. J. Viennot, M. C. Dartailh, A Cottet, and T Kontos, "Coherent coupling of a single spin to microwave cavity photons (supplementary material)", *Science (New York, N.Y.)*, vol. 349, no. 6246, pp. 408–11, 2015, ISSN: 1095-9203. DOI: [10.1126/science.aaa3786](https://doi.org/10.1126/science.aaa3786). [Online]. Available: <http://science.sciencemag.org/content/349/6246/408.abstract>.
- [34] N. Samkharadze, A. Bruno, P. Scarlino, G. Zheng, D. P. Divincenzo, L. Di-carlo, and L. M. K. Vandersypen, "High-Kinetic-Inductance Superconducting Nanowire Resonators for Circuit QED in a Magnetic Field", *Physical Review Applied*, vol. 5, no. 4, pp. 1–7, 2016, ISSN: 23317019. DOI: [10.1103/PhysRevApplied.5.044004](https://doi.org/10.1103/PhysRevApplied.5.044004). arXiv: [1511.01760](https://arxiv.org/abs/1511.01760).
- [35] J. J. L. Morton, A. M. Tyryshkin, R. M. Brown, S. Shankar, B. W. Lovett, A. Ardavan, T. Schenkel, E. E. Haller, J. W. Ager, and S. A. Lyon, "Solid-state quantum memory using the <sup>31</sup>P nuclear spin", vol. 455, no. October, pp. 1085–1088, 2008. DOI: [10.1038/nature07295](https://doi.org/10.1038/nature07295).
- [36] S. Freer, S. Simmons, A. Laucht, J. T. Muhonen, J. P. Dehollain, R. Kalra, F. A. Mohiyaddin, F. E. Hudson, K. M. Itoh, J. C. Mccallum, D. N. Jamieson, A. S. Dzurak, and A. Morello, "A single-atom quantum memory in silicon", 2017.
- [37] K. Saeedi, S. Simmons, J. Z. Salvail, P. Dluhy, H. Riemann, N. V. Abrosimov, P. Becker, H.-j. Pohl, J. J. L. Morton, and M. L. W. Thewalt, "Room-Temperature Quantum Bit Using Ionized Donors in Silicon-28", 2013.
- [38] K. M. Itoh, "Isotope engineering of silicon and diamond for quantum computing and sensing applications", *MRS Communications*, vol. 4, no. 4, pp. 143–157, 2014. DOI: [10.1557/mrc.2014.32](https://doi.org/10.1557/mrc.2014.32).
- [39] M. D. Jenkins, D Zueco, O Roubeau, G Aromí, J Majer, and F Luis, "A scalable architecture for quantum computation with molecular nanomagnets", vol. 45, no. 42, 2016. DOI: [10.1039/c6dt02664h](https://doi.org/10.1039/c6dt02664h).
- [40] M. Pioro-Ladrière, T. Obata, Y. Tokura, Y.-S. Shin, T. Kubo, K. Yoshida, T. Taniyama, and S. Tarucha, "Electrically driven single-electron spin resonance in a slanting Zeeman field", *Nature Physics*, vol. 4, no. 10, pp. 776–779, 2008, ISSN: 1745-2473. DOI: [10.1038/nphys1053](https://doi.org/10.1038/nphys1053). [Online]. Available: <http://www.nature.com/doifinder/10.1038/nphys1053>.
- [41] Z. Shi, C. B. Simmons, J. R. Prance, J. K. Gamble, T. S. Koh, Y.-p. Shim, X. Hu, D. E. Savage, M. G. Lagally, M. A. Eriksson, M. Friesen, and S. N. Coppersmith, "Fast Hybrid Silicon Double-Quantum-Dot Qubit", vol. 140503, no. April, pp. 1–5, 2012. DOI: [10.1103/PhysRevLett.108.140503](https://doi.org/10.1103/PhysRevLett.108.140503).
- [42] M. Russ and G. Burkard, "Three-electron spin qubits", 2017. arXiv: [arXiv : 1611.04945](https://arxiv.org/abs/1611.04945).
- [43] J. Salfi, "Charge-Insensitive Single-Atom Spin-Orbit Qubit in Silicon", *Physical Review Letters*, vol. 246801, no. June, pp. 1–6, 2016. DOI: [10.1103/PhysRevLett.116.246801](https://doi.org/10.1103/PhysRevLett.116.246801).
- [44] G. Tosi, F. A. Mohiyaddin, H. Huebl, and A. Morello, "qubits in isotopically enriched Si Circuit-quantum electrodynamics with direct magnetic coupling to single-atom spin qubits in isotopically", vol. 087122, no. 2014, 2017. DOI: [10.1063/1.4893242](https://doi.org/10.1063/1.4893242).

- [45] J. J. Pla, K. Y. Tan, J. P. Dehollain, W. H. Lim, J. J. L. Morton, F. a. Zwanenburg, D. N. Jamieson, A. S. Dzurak, and A. Morello, "High-fidelity readout and control of a nuclear spin qubit in silicon.", *Nature*, vol. 496, no. 7445, pp. 334–8, 2013, ISSN: 1476-4687. DOI: [10.1038/nature12011](https://doi.org/10.1038/nature12011). arXiv: [1302.0047](https://arxiv.org/abs/1302.0047). [Online]. Available: <http://www.ncbi.nlm.nih.gov/pubmed/23598342>.
- [46] J. Bollinger, "3 & 0," *Physical Review Letters*, vol. 54, no. 10, pp. 1000–1003, 1985.
- [47] A. J. Sigillito, A. M. Tyryshkin, T Schenkel, A. A. Houck, and S. A. Lyon, "Electrically driving nuclear spin qubits with microwave photonic bangap resonators", pp. 1–8, 2017. arXiv: [arXiv:1701.06650v1](https://arxiv.org/abs/1701.06650v1).
- [48] P London, J Scheuer, J Cai, I Schwarz, A Retzker, M. B. Plenio, M Katagiri, T Teraji, S Koizumi, J Isoya, R Fischer, L. P. McGuinness, B Naydenov, and F Jelezko, "Detecting and Polarizing Nuclear Spins with Double Resonance on a Single Electron Spin", vol. 067601, no. August, pp. 1–5, 2013. DOI: [10.1103/PhysRevLett.111.067601](https://doi.org/10.1103/PhysRevLett.111.067601).
- [49] A. Laucht, R. Kalra, S. Simmons, J. P. Dehollain, J. T. Muhonen, F. A. Mohiyaddin, S. Freer, F. E. Hudson, K. M. Itoh, D. N. Jamieson, J. C. Mccallum, A. S. Dzurak, and A Morello, "A dressed spin qubit in silicon", *Nature Nanotechnology*, vol. 12, no. 1, pp. 61–66, 2016, ISSN: 1748-3387. DOI: [10.1038/nnano.2016.178](https://doi.org/10.1038/nnano.2016.178). [Online]. Available: <http://dx.doi.org/10.1038/nnano.2016.178>.
- [50] J. Pachos and H. Walther, "Quantum Computation with Trapped Ions in an Optical Cavity", vol. 1, pp. 2–5, 2002. DOI: [10.1103/PhysRevLett.89.187903](https://doi.org/10.1103/PhysRevLett.89.187903).
- [51] Z.-b. Feng, "Coupling charge qubits via Raman transitions in circuit QED", no. September, pp. 1–5, 2008. DOI: [10.1103/PhysRevA.78.032325](https://doi.org/10.1103/PhysRevA.78.032325).
- [52] M Abanto, L Davidovich, B. Koiller, and R. L.D. M. Filho, "Quantum computation with doped silicon cavities", no. November 2009, pp. 1–7, 2010. DOI: [10.1103/PhysRevB.81.085325](https://doi.org/10.1103/PhysRevB.81.085325).
- [53] A. Angerer, T. Astner, D. Wirtitsch, H. Sumiya, S. Onoda, J. Isoya, S. Putz, and J. Majer, "element microwave resonator Collective strong coupling with homogeneous Rabi frequencies using a 3D lumped element microwave resonator", vol. 033508, 2016. DOI: [10.1063/1.4959095](https://doi.org/10.1063/1.4959095).
- [54] R. Li, L. Petit, D. P. Franke, J. P. Dehollain, J. Helsen, M. Steudtner, N. K. Thomas, Z. R. Yoscovits, K. J. Singh, S. Wehner, L. M. K. Vandersypen, J. S. Clarke, and M. Veldhorst, "CONDENSED MATTER PHYSICS A crossbar network for silicon quantum dot qubits", no. July, pp. 1–11, 2018.
- [55] D. P. Franke, J. S. Clarke, and M Veldhorst, "Rent's rule and extensibility in quantum computing", pp. 1–8, 2018. arXiv: [arXiv:1806.02145v1](https://arxiv.org/abs/1806.02145v1).
- [56] F. Motzoi, J. M. Gambetta, P. Rebentrost, and F. K. Wilhelm, "Simple Pulses for Elimination of Leakage in Weakly Nonlinear Qubits", *Physical Review Letters*, vol. 103, no. 11, pp. 1–4, 2009, ISSN: 00319007. DOI: [10.1103/PhysRevLett.103.110501](https://doi.org/10.1103/PhysRevLett.103.110501). arXiv: [0901.0534](https://arxiv.org/abs/0901.0534).
- [57] J. Werschnik and E. K. U. Gross, "Quantum Optimal Control Theory", 2007. DOI: [10.1088/0953-4075/40/18/R01](https://doi.org/10.1088/0953-4075/40/18/R01). arXiv: [0707.1883](https://arxiv.org/abs/0707.1883). [Online]. Available: <http://arxiv.org/abs/0707.1883>.
- [58] C. D. Hill, "Robust controlled-NOT gates from almost any interaction", *Physical Review Letters*, vol. 98, no. 18, pp. 1–4, 2007, ISSN: 00319007. DOI: [10.1103/PhysRevLett.98.180501](https://doi.org/10.1103/PhysRevLett.98.180501). arXiv: [0610059v2](https://arxiv.org/abs/0610059v2) [arXiv:quant-ph].

- [59] M. J. Curry, T. D. England, N. C. Bishop, G. Ten-Eyck, J. R. Wendt, T. Pluym, M. P. Lilly, S. M. Carr, and M. S. Carroll, "Cryogenic preamplification of a single-electron-transistor using a silicon-germanium heterojunction-bipolar-transistor", *Applied Physics Letters*, vol. 106, no. 20, 2015, ISSN: 00036951. DOI: [10.1063/1.4921308](https://doi.org/10.1063/1.4921308). arXiv: [1509.08201](https://arxiv.org/abs/1509.08201).
- [60] A. G. Fowler, M. Mariantoni, J. M. Martinis, and A. N. Cleland, "Surface codes : Towards practical large-scale quantum computation", vol. 032324, 2012. DOI: [10.1103/PhysRevA.86.032324](https://doi.org/10.1103/PhysRevA.86.032324).
- [61] A. Steane, "Multiple Particle Interference and Quantum Error Correction", no. 1982, 1996, ISSN: 1364-5021. DOI: [10.1098/rspa.1996.0136](https://doi.org/10.1098/rspa.1996.0136). arXiv: [9601029 \[quant-ph\]](https://arxiv.org/abs/quant-ph/9601029). [Online]. Available: <http://arxiv.org/abs/quant-ph/9601029> [Online]. Available: <http://dx.doi.org/10.1098/rspa.1996.0136>.
- [62] E Knill, "Quantum computing with realistically noisy devices", *Nature*, vol. 434, no. 7029, pp. 39–44, 2005, ISSN: 1476-4687. DOI: [10.1038/nature03350](https://doi.org/10.1038/nature03350). [Online]. Available: <http://www.ncbi.nlm.nih.gov/pubmed/15744292>.
- [63] N. H. Nickerson, Y. Li, and S. C. Benjamin, "Rates approaching one percent", *Nature Communications*, vol. 4, pp. 1755–1756, 2013. DOI: [10.1038/ncomms2773](https://doi.org/10.1038/ncomms2773). [Online]. Available: <http://dx.doi.org/10.1038/ncomms2773>.
- [64] B. M. Terhal, "Quantum error correction for quantum memories", *Reviews of Modern Physics*, vol. 87, no. 2, pp. 307–346, 2015, ISSN: 15390756. DOI: [10.1103/RevModPhys.87.307](https://doi.org/10.1103/RevModPhys.87.307). arXiv: [arXiv:1302.3428v1](https://arxiv.org/abs/1302.3428v1).
- [65] R. Barends, J. Kelly, A. Megrant, A. Veitia, D. Sank, E. Jeffrey, T. C. White, J. Mutus, A. G. Fowler, B. Campbell, Y. Chen, Z. Chen, B. Chiaro, A. Dunsworth, C. Neill, P. O'Malley, P. Roushan, A. Vainsencher, J. Wenner, A. N. Korotkov, A. N. Cleland, and J. M. Martinis, "Superconducting quantum circuits at the surface code threshold for fault tolerance", *Nature*, vol. 508, no. 7497, pp. 500–503, 2014, ISSN: 14764687. DOI: [10.1038/nature13171](https://doi.org/10.1038/nature13171). arXiv: [1402.4848](https://arxiv.org/abs/1402.4848). [Online]. Available: <http://dx.doi.org/10.1038/nature13171>.